THE UNIVERSITY OF HULL

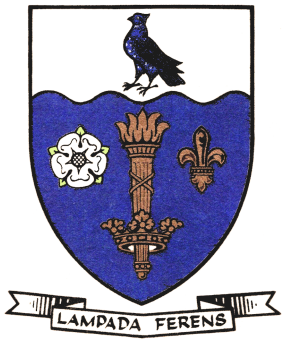

Development of Monte-Carlo Simulations for III-V Semiconductors employing an analytic band-structure

being a Thesis submitted for the Degree of Doctor of Philosophy

in the University of Hull

by

Daniel Robert Naylor B.Sc. (Hons.)

July 2012

Summary of Thesis

The thesis is primarily concerned with the III-V-N semiconductors Gallium Nitride (GaN) and the dilute nitride Gallium Nitrogen Arsenide (GaNAs) and the effect that the band structure has on electron transport in these materials. Ensemble Monte-Carlo algorithms are developed in order to determine the electron transport properties of these materials, coupled with derived expressions for a novel band-structure approximation based on the cosine form that incorporates the inflection point in the Γ valley. The algorithm is validated by comparison of the output of the simulation with the well characteristics of other III-V semiconductors, and the new band-structure approximation is validated through comparison of the generated characteristics with experimental work and the output of the balance equations.

Characteristics for GaN (bulk and in a 1D device) are presented, with excellent agreement with other works. It is found in bulk systems that there is the possibility of a significant number of negative-effective mass states occurring in GaN, dependent on inter sub-band (Γ- L-M) energy separation, and that these states have a noticeable effect on the characteristics of the system, both equilibrium and transient, particularly on the occurrence of the negative differential velocity in the velocity characteristics. A proof-of-concept algorithm for a 1D device code incorporating GaN is also presented with favourable results.

Two models for bulk dilute GaNAs are used, one based on the Nitrogen Scattering model to measure the dispersive effect of N impurities, and one modeling the lower E_-band from the BAC model with the cosine band-structure approximation to measure the distortive effect. Both models are used to generate equilibrium and transient characteristics for the material and we find that we have good agreement with recent works, particularly with the nitrogen scattering model.

Contents

Acknowledgements

It gives me great pleasure to be able to present this thesis, which would simply not have been possible without the unwavering support of many of my colleagues, family and friends. Many of them will unfortunately go unsung, in my attempt to keep this section short (I'm sure I'd be able to write a thesis-length acknowledgements section if I was allowed!), so to the many of you not written here, thank you! However, there are a few who deserve a proper mention for their massive help throughout this PhD.

First, I would like to offer my sincere gratitude to my PhD supervisor, Dr. Angela Dyson, for her utmost faith in my abilities, and for giving me this opportunity to complete a PhD in the first place. Without her, none of this would have been possible, and I couldn't have asked for better supervisor!

For the many ideas and the help that he has provided during my study, directly and indirectly, I thank Prof. Brian Ridley FRS. He is a truly remarkable man, and his support and kindness has been of enormous value to me.

For help throughout my PhD with some of the maths and concepts, I would like to thank Dr. Jianzhong Zhang. He has always been willing to provide help in any way he can, without question, and has always been highly supportive of my abilities and my work.

I would like to thank Dr. David Sands and Dr. Martin Buzza, for their incredibly useful feedback after my interim vivas, and the rest of the staff in the Physics Department for the seven year period for which I have studied at this university, each and every one of them has contributed to getting me to the position which I am in today.

Proper thanks should also go to the various PhD students who shared an office with me, namely Adam Law, Matthew Anyon, Igor Sapina and Anthony Edwards. Over the past four years or so, the time spent in the office has been made a lot more enjoyable, saving me from the clutches of insanity - though I fear that I may have made them go slightly insane in the process! I must also thank Aaron Whittam, whom I lived with during the final year and a half of my PhD and probably drove to the brink of insanity! I also acknowledge the support of other post-docs and MSc and PhD students, both from within the department and from other institutions. I must also thank all those friends of mine from outside these academic circles, their support has been of great value to me!

Last, and by no means least, I must thank my parents, Mark and Christine, and my four younger siblings, Natasha, Michael, Andrew and Leah, who have been incredibly supportive and understanding throughout this period. I hope I have made you all proud.

Declaration of Authourship

I declare that the work presented in this thesis is original, my own, and has not been previously submitted for examination for any other award. Where I have used the results, concepts, or work of others, they have been acknowledged at point of use.

Some of the work that has formed part of this thesis has been the source for the following conference presentations and journal publications:

Conference Presentations

- *D. R. Naylor*, A. Dyson and B. K. Ridley, "Cosine band structure approximation for bulk GaN using Monte Carlo methods", WOCSDICE, Darmstadt/Seeheim, Germany, May 2010.

- *D. R. Naylor*, A. Dyson and B. K. Ridley, "Negative-mass electronic transport in Gallium Nitride using analytic approximations in Monte-Carlo Simulations", TMCS III, School of Electronic and Electrical Engineering, University of Leeds, UK, January 2012.

Publications

- D. R. Naylor, *A. Dyson* & B. K. Ridley, "Steady-state and transient electron transport in bulk GaN employing an analytic bandstructure", *Solid State Communications*, **152** (2012), pp.549–551, doi:10.1016/j.ssc.2011.12.029

- *D. R. Naylor*, A. Dyson & B. K. Ridley, "Steady state and transient electron transport properties of bulk dilute GaN_xAs_{1-x}", *Journal of Applied Physics*, **111** (2012), p. 053703, doi:10.1063/1.3691597

This thesis contains approximately 34753 words, 71 figures and 4 tables.

Daniel R. Naylor
12^{th} June 2012 (revised 1^{st}October 2012)

List of Abbreviations

This is a list of commonly used abbreviations throughout this thesis. These abbreviations are also defined within the body of the text.

Acronym	Meaning
2DEG	Two-dimensional electron gas
ADP	Acoustic deformation potential
BTE	Boltzmann transport equation
CB	Conduction band
EM	Electromagnetic
EMC	Ensemble Monte-Carlo
HEMT	High electron mobility transistor
IV	Inter-valley
LA	Longitudinal acoustic
LO	Longitudinal optical
MC	Monte-Carlo
NDV	Negative differential velocity
NM	Negative effective mass
NPOP	Non-polar optical phonon
ODP	Optical deformation potential
POP	Polar optical phonon
PZ	Piezoelectric
RF	Radio-frequency
SMC	Single electron Monte-Carlo
TA	Transverse acoustic
TE	Transferred electron
TO	Transverse optical

"It can scarcely be denied that the supreme goal of all theory is to make the irreducible basic elements as simple and as few as possible without having to surrender the adequate representation of a single datum of experience."

Albert Einstein, "On the Method of Theoretical Physics", 10 June 1933

Chapter 1
Introduction

Semiconductors play an integral part in society today and have a wide range of applications. Silicon, perhaps one of the best known and understood materials, has been fundamental in the digitalisation of our society, with sophisticated silicon based devices being found all around the home, such as in personal computers, game consoles and mobile telephones. Other semiconductor compounds are also widely used in household appliances, such as in the laser diode that is found in CD/DVD players and, increasingly, Blu-Ray drives. However, there is still much research being done on semiconductors. One such area of research is in high-power, high-frequency semiconductor devices, particularly for use in fast switching devices and terahertz generators and amplifiers for use in medical and security applications. In a drive to attempt to create devices that exhibit these properties, there has been a lot of interest in the research and development of III-V semiconductors, such as GaAs, InP [1, 2] and GaN [3–7]. These III-V semiconductors have superior optical properties in comparison to tried and tested materials such as Silicon, with their direct band gap. The larger electron mobilities present in III-V semiconductors also allow for multi-functional devices to be made. GaN is also the focus of work in high-power applications due to it's huge threshold field for electrical breakdown, such as in high power-gain, high-frequency amplifiers [8, 9]. Much work has also recently been performed on dilute nitride III-V-N materials such as GaNAs [10–12], InNP [13] and GaInNAs, in an effort to create high-frequency response semiconductors. For this thesis, we concentrate on two materials that have shown much promise over recent years, GaN and dilute GaNAs and investigate some material properties which demonstrate the potential for high-power, high-frequency response devices.

We open this chapter by discussing some of the major concepts underpinning semiconductor physics, particularly those that play a major role in high-field III-V semiconductor physics. We then continue by discussing the III-V-N materials GaN and dilute GaNAs in more depth, before finally closing the chapter with an outline for the rest of the thesis.

1.1. Band-structure

If we place an electron in a non-uniform potential (away from any lattice) with energy E and treat the electron as a wave with frequency $\omega = E/\hbar$, through solution of the time independent wave-equation we find that we have a simple relation between E and the wave-vector of the electron, $\mathbf{k}$:

$$E(k) = \frac{\hbar^2 k^2}{2m_e} \tag{1.1.1}$$

where m_e is the electronic mass [14]. This relation is the basis of the free-electron model. As $\hbar k$ can be shown to be the electron momentum, (1.1.1) can be shown to be equivalent to the kinetic energy of the electron in classical physics. However, if we then place the same electron into a lattice that possesses a periodic, varying potential, for example, in a crystal where potential wells form around the atoms in the lattice, we find that this is no longer the case. We now have to solve the Schrödinger wave equation for an electron taking into account the potential at a given position, $\mathbf{r}$. For a crystal potential profile $V(\mathbf{r})$ applied to an electron with the wave function $\psi(\mathbf{r})$ and energy $E(\mathbf{r})$,

$$\left[-\frac{\hbar^2}{2m_0}\nabla^2 + V(\mathbf{r})\right]\psi(\mathbf{r}) = E(\mathbf{r})\psi(\mathbf{r}). \tag{1.1.2}$$

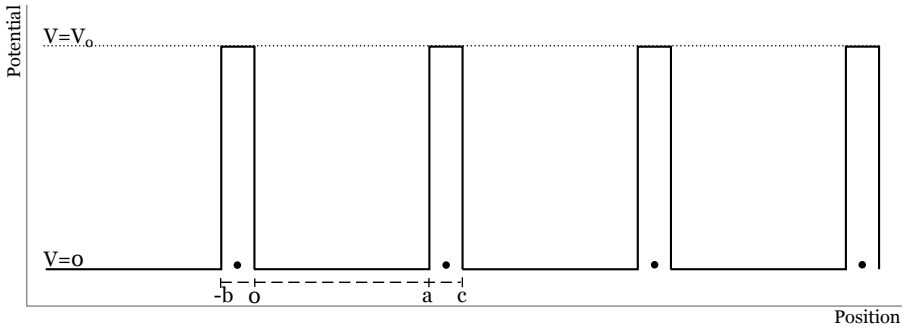

Figure 1.1) A visual representation of the lattice potential profile suggested by the Kronig-Penney model. Dots represent atoms. Image after Kittel [15].

Bloch proved that the solution to this equation must have the form,

$$\psi_{\mathbf{k}} = u_{\mathbf{k}} e^{i\mathbf{k}\cdot\mathbf{r}}, \tag{1.1.3}$$

where $u_{\mathbf{k}}$ is some function, and, for a lattice with a periodicity such that a move by a translational vector $\mathbf{R}$ would result in moving one period,

$$u(\mathbf{r}) = u(\mathbf{r} + \mathbf{R}). \tag{1.1.4}$$

This result, Bloch's Theorem, states that the solution to the wave equation in any periodic potential must itself be periodic [15]. This allows us to concentrate on obtaining the solution solely based on the unit cell, which in reciprocal space is the first Brillouin zone, knowing that the solutions found in one unit cell will apply to all unit cells.

In order to find a simple solution to the Schrödinger wave-equation (1.1.2), Kronig and Penney idealised the one-dimensional potential profile of the system as a series of small square potential barriers centred around the position of the atoms in the lattice [16], as depicted in figure 1.1. Solving (1.1.2) in one dimension, assuming a potential barrier width of b and potential V_0 (as illustrated in figure 1.1),

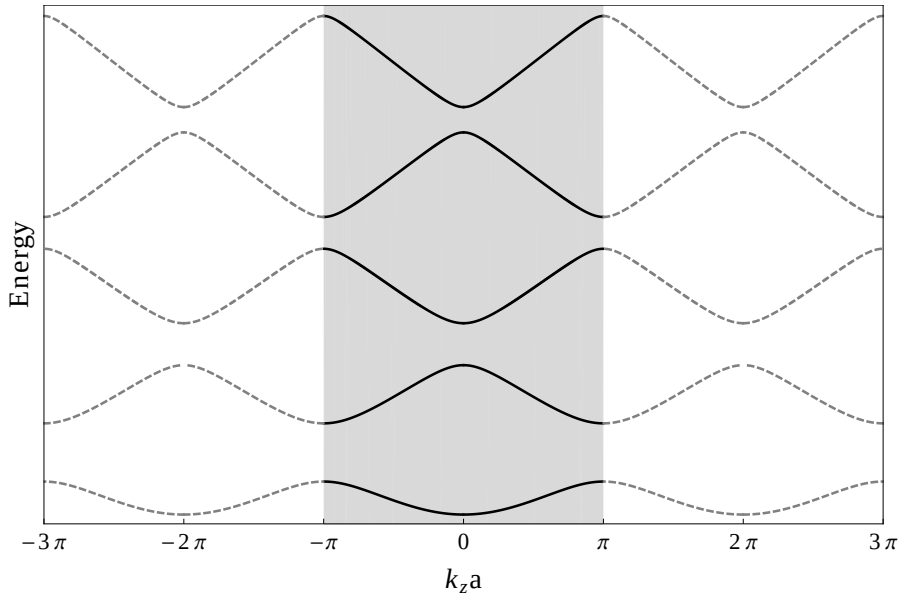

Figure 1.2) $E - k_z$ bands as suggested by the Kronig-Penney model. The shaded area represents the first Brillouin zone, note that either side of this zone is a continuation of this function in accordance with Bloch's theorem.

at the limit where $V_0 \to \infty$, $b \to 0$ and $V_0 b \to constant$ yields the solution,

$$\frac{P}{Ka}\sin(Ka) + \cos(Ka) = \cos ka, \tag{1.1.5}$$

where $K = \sqrt{2m_e E}/\hbar$ and P is a constant based on the selected parameters that quantifies how easy it is for an electron to tunnel through the barriers (with smaller numbers inferring that it is easier to tunnel through). This equation can clearly only hold true when the LHS of (1.1.5) lies between -1 and 1, and as K is proportional to the energy of an electron, it means that there are ranges of energies where no solution to the wave equation exists, giving rise to forbidden energy "gaps" in the band that electrons cannot attain. Figure 1.2 depicts bands as suggested by the Kronig-Penney model if $P = 3\pi/2$, and also illustrates Bloch's theorem, showing that the wave-function is identical across each Brillouin zone, with the principal zone, usually known as the "reduced zone", being shaded. In this model, the bands are symmetric around the zone centre, which is not always the case for more

complex systems.

Whilst using this model can show that there is an infinite number of bands, electrons tend to remain in the lowest energy bands, not all of these bands are useful in transport. If we were to cool the temperature of the system down to 0K, the highest energy band that contains electrons is termed the valence band, and the lowest band that does not contain electrons is termed the conduction band. For the purposes of these thesis, as we are dealing with electron transport, we will solely concentrate on the structure of the conduction band.

1.1.1. The Effective Mass

Whilst the Kronig-Penney model is good for showing the origin of bands and produces a simple result, in three dimensional space, the band-structure is generally more complex. This is partially due to variances in the lattice constants in different directions, and in binary and higher order compounds, the relative sizes and charges of the atoms can also complicate the band-structure. This can often manifest as bands having multiple "valleys", or local energy minima, throughout the Brillouin zone, and the valleys are generally not symmetric in all directions.

Full band-structure models making use of tight-binding (such as work performed in [17]), empirical pseudopotentials [18, 19] or Green's functions [20] can be used to solve transport problems using numerical methods. However, at valley minima located at energy E_c, an analytic approximation for the band-structure similar to the energy of an electron in free-space, the parabolic band-structure approximation, can often be used [14]. It is of the form,

$$E(k) = \frac{\hbar^2 k^2}{2m^*} + E_c. \tag{1.1.6}$$

Such an approximation is based on the concept of the effective mass of an electron, $m*$, and is thus defined as [14, 21, 22]:

$$m^* = \frac{\hbar^2}{d^2E/dk^2}. \tag{1.1.7}$$

For a band with spherical symmetry, or close to the valley minima, m^* is a constant. The concept of effective mass is useful for describing the motion of electrons, it is often the only parameter required for describing the carrier transport around the local energy minima in a material. The parameter m^* is termed the effective mass as an electron in a band will travel as if it has mass m^*. We can demonstrate this by taking the group velocity of the electron wave in a parabolic band, where the effective mass is constant throughout the valley, and showing the momentum using the effective mass is equal to that of the crystal momentum, $\hbar k$,

$$v(k) = \frac{1}{\hbar}\frac{\delta E}{\delta k} = \frac{\hbar k}{m^*} \implies m^* v(k) = \hbar k. \tag{1.1.8}$$

1.1.2. The single band k.p approximation

In reality, valleys in the conduction band are rarely parabolic, and the effective mass of the electron does change as it increases in energy. In order to take this into account, we can use the **k.p** model, which is known as such due to the fact that the solution is based on solving the Schrödinger equation using the Bloch theorem and **k.p** perturbation theory [23]. Solving this for a single conduction band, utilising Bloch's theorem, we obtain the following dispersion relation [22, 24]:

$$\frac{\hbar^2 k^2}{2m^*} = \gamma(E_{\mathbf{k}}) \tag{1.1.9}$$

where m^* is now the effective mass of the electron at the minima of the band. $\gamma(E)$ is usually taken in terms of the Kane non-parabolicity to the first order, obtaining [14, 22, 25],

$$\gamma(E) = E(1 + \alpha E) \tag{1.1.10}$$

where α (the first-order non-parabolicity constant) is taken to be,

$$\alpha = \frac{1}{E_g}(1 - \frac{m^*}{m_e})^2 \tag{1.1.11}$$

where we take E_g to be the difference in energy between the valence band maximum and valley minimum, and m_e to be the rest electronic mass. Note that $\gamma(E)$ does not necessarily have to take the form as shown in (1.1.10), it can include higher order terms or a completely different function, should it be required. (A good recent example where (1.1.11) is not used to determine α can be seen in the publication by Hadi *et al.* [26], who varied this constant to try and determine how altering α affected the characteristics output by their model for ZnO.)

1.2. Electronic Transport

1.2.1. Boltzmann Transport Equation

The Boltzmann transport equation (BTE) describes the behaviour of carrier transport in semiconductors over time in real space and momentum space. For a distribution of electrons described using the distribution function $f(\mathbf{k}, \mathbf{v})$, for an electron with velocity $\mathbf{v}$ when an subjected to an external force $\mathbf{F}$, the Boltzmann Transport

Equation (BTE) is of the form [14, 22]

$$\frac{\partial f}{\partial t} = \left(\frac{\partial f}{\partial t}\right)_{collision} - (\mathbf{v} \cdot \nabla_{\mathbf{r}} f + \mathbf{F} \cdot \nabla_{\mathbf{p}} f), \tag{1.2.1}$$

taking into account the transport evolution due to collisions (electron scattering) and drift due to the applied field only. Unfortunately, due to the BTE being a partial differential equation over six dimensions (three in real space, $\mathbf{r}$, three in momentum space, $\mathbf{p}$), finding an analytic solution to the equation is difficult to do. Steady state solutions have been found, however, using energy and momentum balance equations that incorporate the electron energy and momentum relaxation times. Dyson and Ridley [3] suggest the velocity and energy solutions to be

$$\frac{d\langle v\rangle}{dt} = eF\left\langle\frac{1}{m}\right\rangle - \frac{\langle v\rangle}{\tau_m}, \tag{1.2.2}$$

$$\frac{d\langle E\rangle}{dt} = eF\langle v\rangle - \frac{\langle E\rangle}{\tau_E}, \tag{1.2.3}$$

where τ_E and τ_m are the energy and momentum relaxation times, and $\langle v\rangle$ and $\langle E\rangle$ are the velocity and energy averages of the system. However, these equations depend on prior knowledge of the relaxation times of the system, something that is not always known. The Boltzmann equation can also be solved using numerical methods, such as through the use of Monte-Carlo methods to simulate electron transport though the system. Details of these methods will be presented in a future chapter.

1.2.2. Electron scattering

The BTE provides for collision affected transport, which is primarily down to electrons being scattered during drift in a crystal system. Whilst in a perfect crystal,

electrons would continue to be accelerated in a linear fashion, dependant on the strength of the field, in practice, this is not the case, and electrons can be scattered while drifting, altering the direction of travel and potentially the electron energy. There are many scattering mechanisms that exist, though not all mechanisms exist in all systems, for example, alloy scattering does not occur in pure elemental semiconductors. We therefore focus on the most common scattering mechanisms found in semiconductor transport, scattering caused by charged impurities and threaded dislocations, and scattering that is phonon-assisted.

1.2.2.1. Charged impurity and dislocation scattering

Charged impurity scattering occurs from impurities introduced during crystal growth (wanted or otherwise), whilst threaded dislocations, which is the inclusion or omission of a line of atoms in the host material, often occur due to the strain that is introduced by growing the material on a substrate with different lattice spacings. Both of these imperfections in the host material cause disruptions to the otherwise periodic potential across the system, and thus scatter electrons due to the abnormal field that is exerted around the location of the impurities and dislocations, and thus have the potential to disrupt the path of electrons, particularly slow moving particles that spend longer in the vicinity of the impurity or dislocation.

1.2.2.2. Phonons and phonon-assisted scattering

At temperatures above $0K$, the lattice of any solids encounter vibrations. These lattice vibrations cause the potential landscape around each of the atoms to deform and as a result, disturb electrons in the area. As electrons are much smaller than the atoms, any changes in the system caused by the atoms are almost immediately

picked up by the electrons and affect the path of the electrons. In order to account for the effects of these lattice vibrations in a simple manner, we quantise the energy of the vibrations into phonons with a wave-vector $\mathbf{q}$, and from phonon dispersion relations, frequency $\omega_{\mathbf{q}}$, energy $\hbar\omega_{\mathbf{q}}$. It thus transpires that phonons act as if they have a momentum of $\hbar\mathbf{q}$ and energy $\hbar\omega_{\mathbf{q}}$ when interacting with particles, which allows us to apply the principles of conservation of energy and momentum when determining the outcome of any interaction with other particles. Hence, if an electron with wave-vector $\mathbf{k}$ and energy $E_{\mathbf{k}}$ absorbs a phonon with wave-vector $\mathbf{q}$ and energy $\hbar\omega_{\mathbf{q}}$, through conservation of energy and momentum, we would expect that the electron after the event would have a momentum of $\mathbf{k}+\mathbf{q}$ and an energy of $E_{\mathbf{k}}+\hbar\omega_{\mathbf{q}}$.

There are two major phonon modes that can occur in solids, low-frequency acoustic modes (when neighbouring atoms vibrate in phase with each other) and higher frequency optical modes (when neighbouring atoms vibrate out of phase with each other) [15]. These modes can be further subdivided into transverse and longitudinal modes [27], and there can be multiple modes of each. Longitudinal acoustic (LA) and optical (LO) modes cause acoustic and optical deformation potential scattering mechanisms (also known as acoustic and non-polar optical phonon scattering, respectively), termed as such due to lattice vibrations deforming the band structure of the host material. In polar crystals, LO modes can also induce polarization waves in the material, causing an additional macroscopic time-dependant electric field that the electrons are able to interact with and are thus scattered from. Phonons that affect electrons in this manner are known as polar optical phonons, and are generally the dominant scattering mechanism in polar materials, particularly II-VI and III-V materials. A similar effect also occurs with LA phonons, these po-

lar acoustic phonons cause what is known as piezoelectric scattering [14], though this type of scattering is generally only dominant at low temperatures.

1.2.2.3. Fermi's Golden Rule

Fermi's Golden Rule is the quantum mechanical embodiment of the scattering process. It states that for a electron with an initial state $\mathbf{k}\rangle$ transitioning to a final state $\mathbf{k}'\rangle$ via any particular scattering mechanism, the probability per unit time that this transition will occur is given by [28],

$$S\left(\mathbf{k},\mathbf{k}'\right)=\frac{2\pi}{\hbar}\left|M\left(\mathbf{k}',\mathbf{k}\right)\right|^{2}\delta\left(E_{f}-E_{i}\right) \tag{1.2.4}$$

where $\mathbf{k}$ and $\mathbf{k}'$ are the initial and final wave-vectors of an electron, $|M\left(\mathbf{k}',\mathbf{k}\right)|$ is the scattering mechanism matrix element that links the two states and E_f and E_i are the final and initial electron energies. To obtain a scattering rate in three dimensional space, the sum can be converted to an integral over all potential final states in a crystal with volume Ω. For one-phonon scattering, where $E_{\mathbf{k}}$ and $E_{\mathbf{k}'}$ are the energies of the initial and final states and $\hbar\omega$ is the energy of a single phonon, we obtain [22],

$$W\left(\mathbf{k}\right)=\frac{\Omega}{(2\pi)^{3}}\frac{2\pi}{\hbar}\int\left|M\left(\mathbf{k}',\mathbf{k}\right)\right|^{2}\delta\left(E_{\mathbf{k}'}-E_{\mathbf{k}}\mp\hbar\omega\right)\delta_{\mathbf{k}'-\mathbf{k}\mp\mathbf{q},\mathbf{0}}d\mathbf{k}'. \tag{1.2.5}$$

The $\mp$ arises from the two phonon interactions that can occur in conjunction with the principle of conservation of energy, phonon absorption (corresponding to the minus in the equation), and phonon emission (corresponding to the plus in the equation), in order to make the delta function equal to zero.

Fermi's Golden Rule is derived from perturbation theory with the assumption

that any collision occurs instantaneously and has a permanent effect. However, as there are many collisions in any system, it is clear that the effects of any collision is not permanent. Each collision is not instantaneous either. However, if the duration of each collision (that is, the amount of time that the collision mechanism affects the particle) is much smaller than the time between collisions, then we find that this rule is valid - a condition that we find to be satisfied in nearly all cases [22, 29].

1.2.3. High Field Transport

One of the great draws of some of the materials that we will be studying in this thesis is that they exhibit interesting effects in high field scenarios. First focussing on the steady state high-field effects, Figure 1.3 shows the steady-state velocity-field characteristics for Gallium Arsenide (GaAs) as generated by a two-valley model. In low fields, electronic transport is ohmic, the velocity of an electron v_d is linearly proportional to the applied electric field F. We term this constant of proportionality as the low-field mobility, μ_{low}, for the host material, giving the relation:

$$v_d = \mu_{low} F. \tag{1.2.6}$$

As it can be seen in figure 1.3, (1.2.6) describes the low-field transport of the GaAs system well when we set $\mu_{low} \approx 8300\,\mathrm{cm^2V^{-1}s^{-1}}$ (which is consistent with other work [30, 31]). However, when we reach the mid- to high-field regions of the graph, we see a deviation from this ohmic behaviour and low-field mobility, with the velocity reaching a peak "saturation" velocity, v_{sat}, before the velocity of the electrons in the system decreases as the applied field increases, or a negative differential velocity (NDV). Whilst NDVs do not occur in all materials, such as

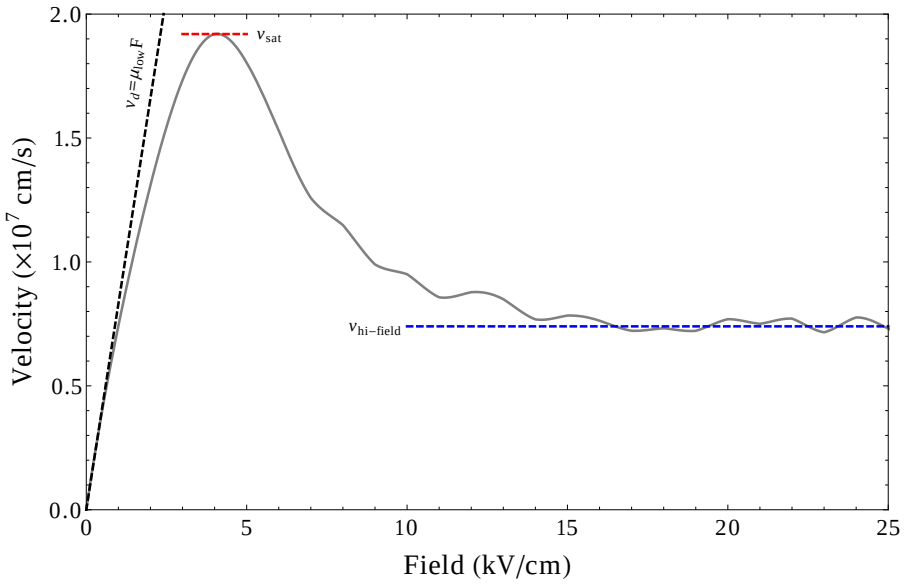

Figure 1.3) A velocity-field characteristic for GaAs generated from an Ensemble Monte-Carlo code using the **k.p** band-structure approximation describing various key features.

Silicon [32], which just reaches a maximum saturation velocity, they do in the materials that we study in this thesis, and it is thus important to be able to understand the processes behind them.

NDVs can occur for multiple reasons. The most well-known reason is due to the Gunn effect [33], which is physical embodiment of the Ridley-Watkins-Hilsum theory [34, 35], also known as the Transferred Electron (TE) effect. The TE effect only occurs in multi-valley systems, and is, as the name suggests, the effect of electrons transferring from one valley to another distinct valley. As the momentum of an electron is relative to the local minima of the valleys, electrons transferring between the valleys could mean a sudden change in momentum. This effect is particularly prominent when electrons are able to transfer from the middle (in terms of energy) of one valley to the bottom of a satellite valley where the energy minima is located higher with a larger effective mass, due to conservation of momentum, the velocity of the electron must decrease.[32]. It is also usually the case that the effective mass in the upper valleys is much higher that that in the lower valleys,

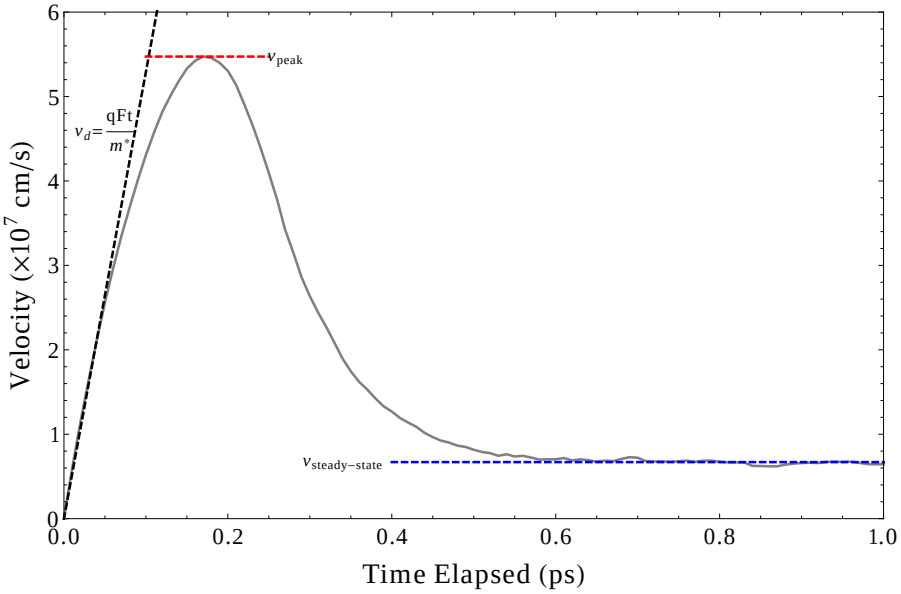

Figure 1.4) Velocity Overshoot in GaAs generated from the Ensemble Monte Carlo model using the **k.p** approximation (as described in Chapters 2) when the applied field is 25 kV/cm. Parts of this image after Ferry [21].

making it more difficult for electrons to gain momentum, which contributes to the severity of the NDV. The NDV in figure 1.3 is caused by this TE effect combined with higher effective masses in the upper valley. NDVs may also occur due to the shape of the band-structure. In materials such as GaN, there is an inflection point close to the energy centre of the central Γ valley [18, 36] where electrons begin to experience negative effective mass effects, and decelerate as a larger energy is attained. If enough electrons are able to attain these states, then as the applied field, and hence, the average energy of the system increases, the average velocity of the system may decrease causing a NDV.

1.2.3.1. Velocity Overshoot

One curious phenomenon that occurs in these materials at high field is the occurrence of velocity overshoot in the transient regime when the energy relaxation time of a system is greater than that of the momentum relaxation time. This transient characteristic is depicted in figure 1.4. Initially when the field is switched on, the

electrons in the system, having not undergone any effects that would cause an NDV, attempt to reach the drift velocity to match the low field mobility (which would be by continuing to follow the black dashed line in figure 1.4) [21]. As the average energy of the system rises, the characteristic deviates from this path to reach a peak velocity (v_{peak}). In low field scenarios, this peak velocity is also the steady state velocity, as the peak velocity has been reached due to equilibrium being reached between the drift due to the field and the scattering mechanisms. In high-field scenarios, however, we find that the electron velocity begins to drop again, due to electrons beginning to undergo (in the case of GaAs) the TE effect and/or negative effective mass transport and thus decelerating, before finally reaching equilibrium at the steady state velocity, $v_{steady-state}$. We find at higher fields, that the peak velocity is generally higher and occurs earlier, as the increase in field ensures that the electrons accelerate faster and gain energy more quickly, reaching the threshold for either of these processes much sooner.

1.2.4. Effect of Crystal Structure

Throughout this thesis, we examine materials with two different crystal structures, zinc blende and wurzite. Both of these crystal structures are tetrahedral in nature, however, whilst zinc blende has face-centred cubic symmetry, the wurzite crystal structure has hexagonal symmetry [29]. This difference in structure inevitably has effects on the shape of the band structure, but more importantly, the lack of inversion symmetry means that more than one LO phonon mode can occur.

Whilst most of the materials we study in this thesis posses the zinc blende crystal structure, Gallium Nitride, whilst it exists in both crystalline forms, the Wurzite form is more commonly found in nature as it is more energetically favourable. Thus,

we will use Wurzite band-parameters for GaN throughout this work. However, as the energies of the optical phonon modes for wurzite GaN are close to the energy for a zinc blende GaN optical phonon, we make the approximation that there is only one optical phonon mode in wurzite GaN and that its energy is the same as that of zinc blende GaN. It has previously been noted that this is a reasonable approximation to make, particularly as the effect of these extra phonon modes and the associated anisotropy is small [37].

1.3. N-based III-V Semiconductors

III-V semiconductors have always been the source of much interest, with materials such as Gallium Arsenide (GaAs) and Indium Phosphide (InP) now well characterised throughout the semiconductor world. With direct band-gaps and high electron mobilities, these materials have found many uses in the optoelectronic world. These materials also have many uses in building electronic devices, their high mobilities and large potential electron velocities make them ideal for use in high-frequency electronics.

Whilst GaAs and InP have been thoroughly investigated and are well understood, many of the Nitrogen based III-V materials are not. However, much is being done to remedy this, and there have been many theoretical and experimental studies performed in order to understand the properties of these N-based systems. In particular, two N-based III-V based compounds, Gallium Nitride and dilute Gallium Nitrogen Arsenide, have been the subject to a lot of recent research, and form much of the work underpinning this thesis. We thus discuss the properties and the surrounding interest of these two materials.

1.3.1. Gallium Nitride

The use of wide band-gap materials, such as Gallium Nitride, has gained a lot of interest in the area of semiconductor physics. As a result, there has been a lot of research, both theoretically and experimentally, on bulk GaN and device hetrostructures where GaN is a constituent material. GaN is an excellent material for use in high-power and high-frequency applications, as it has been shown to have a high breakdown field and a large saturation velocity. It is also a good material for use in optical applications, due to it's wide, direct band gap. GaN has been shown that it is a highly stable material, electronically and thermally, even though it tends to have a larger concentration of defects per unit volume than other III-V and II-VI semiconductor compounds [38]. This larger defect density is partially due to that fact that the growth of GaN crystals is difficult to do perfectly, as there are no materials that are lattice-matched to GaN to grow on. Therefore, there has been a significant effort to grow GaN on Silicon Carbide (SiC), where the lattice mis-match along the a-axis is 0.11 Å, or 3.4% [39]. This has proven to be successful, due to GaN's high stability, however, there are still ongoing efforts to find an improved lattice matching for GaN in order to increase the quality and performance of GaN overall [39, 40]. There has also been work done on growing GaN on a GaN substrate, thereby eliminating one of the sources of defects in the material [41].

Optically, GaN is very well understood. Naturally operating at a optical wavelength of 405 nm, and through the creation of higher order compounds incorporating GaN, such as Indium Gallium Nitride (InGaN), other, slightly longer wavelengths reaching into the green and yellow ranges of the visible light spectrum. Due to these properties, combined with the well established red LEDs, it is now possible to

create the full range LED colours efficiently. A good example of their use is in traffic lights, their fast response time and high efficiency when compared to conventional light bulbs means that their use is now widespread across the UK. GaN has also been used to create white light LEDs with higher efficiencies than conventional bulbs, and work is ongoing to create higher efficiency white light sources [42]. Other optics-based uses for GaN include the creation of the blue laser diode, which can now be found in many consumer households in Blu-Ray players, with the smaller wavelengths achieved by this diode allowing for higher capacity optical discs to be read.

Whilst the optical technology based on GaN is mature and, for the most part, well understood, the electronic transport properties and the technology surrounding these properties are not. Fortunately, there has been much recent interest in this area as GaN is especially suited for high power technologies due to it's high breakdown field, suggested to be above $4\,\mathrm{MV/cm}$ [17, 43], and it has also been linked with high frequency applications as it possesses a large saturation velocity, estimated to be in the region of $2.5 - 3 \times 10^7\,\mathrm{cm/s}$ [44, 45].

One particular technology that has been researched in recent years is the use of GaN and other nitride compounds (especially AlGaN/GaN and InGaN/GaN heterostructures) is the High Electron Mobility Transistor (HEMT, also known as the Heterostructure Field Effect Transistor, or HFET) [46]. While most semiconductor devices are created through the doping of the active semiconductor materials, HEMTs work through the creation of a junction between a highly-doped wide-gap material and an undoped material with a narrower band gap and a lower conduction band minima to form a triangular quantum well, and within it a "two-dimensional electron gas", or 2DEG. As the electrons in this 2DEG are, as the name

implies, confined to movement in two directions and that the 2D electron mobilities are greater than their 3D counterparts, the use of 2DEGs is advantageous for use in fast switching applications. GaN based HEMTs have wide range of uses in the high-power, high-frequency markets, with one such use being high-gain, highly efficient power amplifiers for pulsed signals, thanks to their high breakdown field and high frequency response, with power output reported to be between 250W and 400W at microwave frequencies [9, 47–49]. This technology has made its way into mobile network base stations, utilising the material's high-power, high-frequency and high mobility characteristics that are required for the broadcast of reliable, wide-ranging 4G networks, and has been researched for use in the competing WCDMA (Wide-band Code Division Multiple Access) [50] and WiMAX (Worldwide Interoperability for Microwave Access) [51] 4G networking systems, with these devices operating comfortably at these 4G frequencies of 2.2GHz, amplifying the input signal with a power added efficiency of approximately 55%. HEMTs, in this role of high frequency power amplification, have also got a place in military applications, with developments into versatile, high-gain, broadband response amplifiers that can be used with a multitude of high power military equipment [8]. Some research has also been conducted into the use of GaN based HEMTs in terahertz detection and amplification [5, 52], though most research into terahertz detectors using HEMTs has now moved onto other materials such as InP and GaAs [4, 53].

There has also been recent focus on the causes of the negative differential velocity (NDV) of the electrons that occurs under high-field conditions with a view to potentially exploit these underlying causes for terahertz frequency band (usually defined as the 300GHz - 3THz band between infra-red and microwave frequencies) electromagnetic radiation generation [3, 54]. There are two major causes of the NDV that

have been suggested in GaN, the first being the transferred electron effect, and the second cause being the inflection point in the band structure which allows for negative effective mass states, as first suggested by Krömer [55]. As the availability of THz emitters is well sought after, due to its uses in the security and medical imaging industries, as well as there being research into HEMT technology, much research has been undertaken in order to exploit the potential properties of GaN causing these NDVs. Recently, there has been much theoretical and experimental activity in the creation and operation of Gunn diodes, which work on the principle of the Gunn effect, for this purpose. One of the earliest results by Joshi *et al.* [6] suggested that for a Gunn diode that is $1\mu m$ in length with a potential of 50 V applied across it, EM radiation of frequency 135GHz could be emitted. Since then, there has be much activity in the theoretical simulation of these devices, with these simulations yielding suggestions that GaN based Gunn devices can indeed emit RF radiation in the THz band. Drift-diffusion models have suggested that GaN Gunn diodes can reach about 1.8THz [54], while Monte-Carlo based simulations suggest operating frequencies of 300GHz. Simulations by Macpherson *et al.* [56], which includes self-heating effects, suggests that a room temperature Gunn diode based on GaN with an active region of 2μm in length can achieve approximately 280 GHz with higher frequencies possible at lower temperatures, whilst more recently, Yang *et al.* [57] have calculated that it should be possible for a GaN to reach an operating frequency of 352GHz at room temperatures. It is interesting to note that the temperature dependence suggested by the two models are completely different, Yang *et al.* believe that increasing the temperature of the system would increase the operating frequency of the device, Macpherson *et al.* believe the opposite. This discrepancy may be down to the differences between the models that have been

used, though these differences serve as a good example to show that there is still a lot that is not understood and that there is still a lot of research being performed in an attempt to determine the exact properties of these systems.

Whilst there is still some debate in the community as to the actual properties of the GaN Gunn diode, and whether THz radiation can be generated, there have been experimental attempts to verify some of the properties of this diode. Yilmazoglu *et al.* [58] fabricated a device and recorded the current-voltage characteristics from the device, noting that the calculated drift velocities as determined from the experimental values matched previous theoretical predictions (comparing favourably with works such as Joshi *et al.* [6], Foutz *et al.* [44]) and experimental results from bulk measurements [59].

1.3.2. Dilute Gallium Nitrogen Arsenide

As well as binary compounds such as GaN, there has been much interest in the use of ternary III-V based semiconductor materials. Indeed, there has been much recent activity of research into III-V materials that have been doped with small concentrations of nitrogen atoms, due to the strong effects that the nitrogen impurities have on the host semiconductor material. Nitrogen (N) states in dilute nitrides have distinct localized energy levels and, amongst other effects, causes a large optical bowing of the band gap [13, 60, 61] and highly distorts the dispersion relation in the conduction band (CB) of the host material.

One material of particular note is lightly N-doped GaAs, or GaN_xAs_{1-x} (which we shall refer to as dilute GaNAs henceforth in this chapter). Dilute GaNAs inherits many of the properties of GaAs, however, due to the strong effect of the N impurities, the band gap between the conduction and valence bands reduces

(with a reduction of about 50 meV at ultra-dilute N concentrations, up to 0.4 eV at 4% N concentration) [62], and significantly alters the electron effective mass within the conduction band [63–65]. Indeed, the band-anticrossing (BAC) model as originally suggested by Shan et. al. [66], and then later refined through the use of Green's functions [20], suggests that the GaNAs conduction band around the Γ point actually splits into two or more sub-bands, and that an inflection point is introduced into the lower sub-band of the Γ band structure, potentially allowing for electrons to reach negative effective mass (NM) states.

Like GaN, dilute GaNAs has both potential optical and electronic uses. It is usually less favoured than the quaternary compounds containing gallium, nitrogen and arsenide, such as InGaNAs, though it is recognised that GaNAs is a good material for determining the properties of dilute nitrides [67]. Nevertheless, GaNAs has been used for practical applications. One such property that has been exploited is the optical bowing caused by the introduction of the N impurities which causes the material band gap to narrow, and as a result, an optical red-shift is observed. In particular, the ability to tune the band gap of the material by varying the nitrogen concentration of the material is a highly useful one, especially for optoelectronic devices. One such device which has benefited from such tunability is the solar cell [68], by using this ability, an optimal band gap, and thus, an optimal nitrogen concentration can be found for the solar cells such that their efficiency are as high as possible.

Recent work has been focused on determining the steady-state electronic properties of bulk GaNAs, directed towards determining the origin of the negative differential velocity (NDV) [11, 69] and on the mid to high field properties of the semiconductor [70]. It has previously been suggested that GaNAs has the poten-

tial for use in high-frequency scenarios, particularly in the terahertz region [10, 71], and as such, understanding of the transient regime is crucial in order to be able to potentially exploit this property.

1.4. Outline of Thesis

The next two chapters of this thesis are concerned with the algorithms and equations required to develop models in order to determine the properties of these III-V-N materials. Chapter 2 describes the different algorithms that are utilized in order to obtain results for this thesis, whilst chapter 3 explores the use of a new analytic band-structure approximation that is particularly suitable for Gallium Nitride and other dilute nitrides. The work presented in the first two chapters is then combined in chapter 4, where the algorithm is tested and validated against materials with well known parameters and characteristics, such as Gallium Arsenide and Indium Phosphide, and the new band-structure approximation is tested and contrasted with well known band-structure approximations.

The next two chapters then use the algorithms and approximations previously presented to determine the transport properties of GaN and dilute GaN_xAs_{1-x}. Chapter 5 is concerned with the characteristics of bulk GaN, whilst chapter 6 extends the model to simulate one-dimensional devices and analyses the characteristics of this model. We then take a look at bulk GaN_xAs_{1-x} using two different approaches in chapter 7, and discuss the effect of Nitrogen on the host band structure. We draw the thesis to a close in chapter 8 by drawing conclusions from this work and discuss potential future extensions to the project.

Chapter 2
Monte-Carlo methods for electron transport simulations

The use of a Monte-Carlo (MC) method is well suited for semiconductor electron transport simulations. It is one of many models that can be used in semiconductor transport simulations, which range from the semi-classical drift-diffusion (DD) models to full quantum descriptions using numerical solutions of the Schrödinger equation. DD models make use of the drift-diffusion equations that have been derived from the Boltzmann Transport Equation, however, this model is unsuitable for investigating sub-micron devices and non-equilibrium behaviour. To study such phenomena more complex models must be adopted. Numerical solutions of the Schrödinger equation result in a highly accurate set of data being produced, however the computational effort would be very great and can only be achieved for a small number of particles. Green's Functions methods, while a slightly less accurate method, would allow for a solution containing many more particles than the Schrödinger equations would allow. However, the use of Green's Functions would still be computationally challenging.[72]

Monte-Carlo methods are between the DD and full quantum methods in terms of both speed and accuracy. These methods can be used as purely semi-classical methods, or, if the problem requires it, quantum corrections can be included in order to take account of possible many body effects. However, for the purposes for work in this thesis, the semi-classical approach will be sufficient. This chapter will describe the Monte Carlo method implemented in the different codes and algorithms that have been used. Whilst most of the algorithms are based on that presented by *Tomizawa* [25], the codes have been re-designed and re-developed in

FORTRAN 95 to accommodate the chosen band-structure models.

In this chapter, we first discuss the use of an analytic band-structure in Monte-Carlo models. We then give the base algorithm for our Monte Carlo models using analytic band-structures for bulk materials of infinite size, and then finally 1D n^+-i-n^+ devices, limited in size in the direction of the applied electric potential. Then, in each case, the differences between the methods will be discussed.

2.1. Band-structure approximation in Monte-Carlo models

One of the most important parts of any charge transport simulation, whether it is bulk or more complex, is how the band-structure of the material is modelled - in the case of electrons, the energy profile of the conduction band across the Brillouin zone. The shape of the band, how the energy (E) of an electron relates to its wave-vector ($\mathbf{k}$), affects much in the simulation as it has a fundamental effect on the Density of States function, and in turn, this affects the rate of scattering of any electron in the band. It is therefore in our interest to ensure the band-structure is represented accurately in Monte-Carlo codes. Full-band models, by the very name, use numerical data (e.g., from data calculated from empirical pseudo-potential methods (EPM)) to build the full conduction band structure. The drawback of this method is that this requires the use of numerical methods to calculate the other information required for the simulation, such as scattering rates and density of states at each point of the band, and this can take a considerable amount of computing time and memory. For this reason, simulations that approximate various sections of the band-structure using analytic equations are often favoured.

In analytic simulations, like those presented in this thesis, the Monte-Carlo

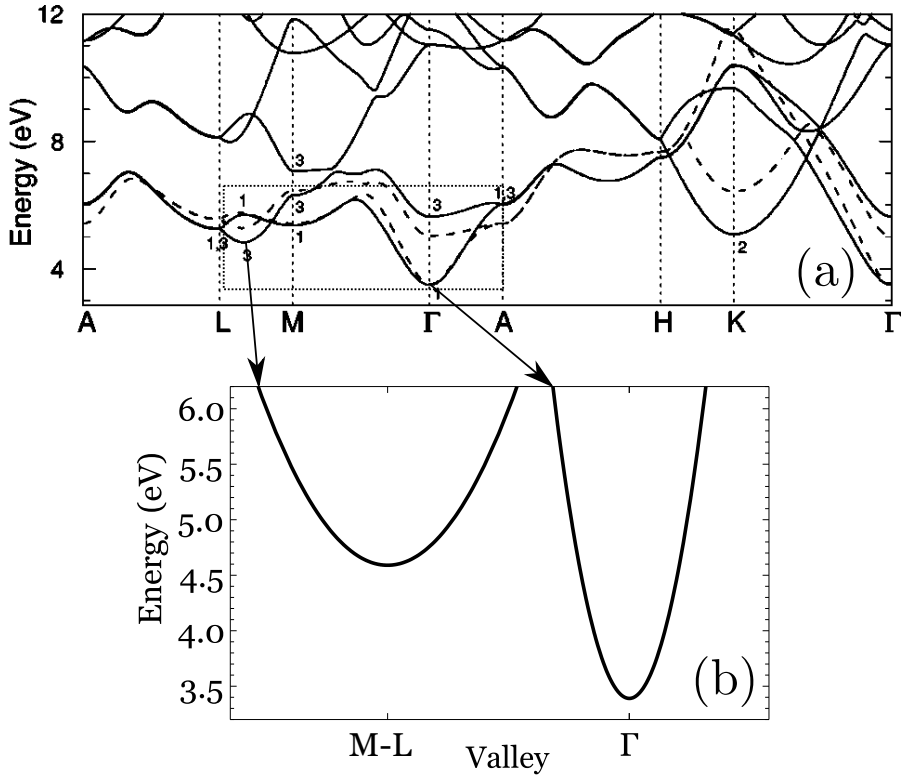

Figure 2.1) (a) The conduction band-structure of wurzite GaN as calculated by EPM (image after Bulutay *et al.* [18]) and (b) how a sample analytic two-valley model for use in Monte-Carlo codes based on this band structure would be conceptualised if a parabolic approximation was used. Energy scale on the y-axis is relative to the top of the valence band.

method treats each of the energy minima and the surrounding structure, each known as a valley (for example, a energy minima at the Γ point and the surrounding band-structure would be known as the Γ valley), as unlinked self contained valleys rather than treat the system as continuous throughout the whole Brillouin zone (see Figure 2.1). Each valley is then characterised by an analytic $E - \mathbf{k}$ relation, rather than numerical data, which allows for the use of analytic relations when calculating scattering rates, decreasing algorithm complexity and run-time significantly. It is assumed that the only way an electron can transfer to a different valley in this model is via a phonon assisted scattering process. A full continuous band-structure is not simulated, rather, analytic approximations including only the valleys around two or three of the lowest energy minima are used. Spherical

symmetry is also often assumed and hence, the $E-\mathbf{k}$ relation is the same in all directions. Some semiconductors may require the use of ellipsoidal symmetry instead [22, 25], such an approach is not required in this work.

Using this approach does have its drawbacks, however. Most band-structure approximations, such as the simple parabolic approximation (as depicted in Figure 2.1) or the slightly more complex **k.p** approximation do not have an upper limit, so theoretically, electrons in the simulation can achieve larger energies than would normally be allowed by the actual band structure without transferring to higher energy valleys. In practice, however, the probability of this happening is small, though it can lead to slight over-estimation of average energies and other transport properties.

Regardless of the drawbacks that arise from using the analytic methods, Monte-Carlo methods using analytic band-structure models, if set up correctly, provide good agreement with experiment and other theoretical methods, examples of this can be seen in Chapter 4.

2.2. Algorithm for bulk materials

In bulk materials, the following algorithm is used as a base in simulations:

1. Calculate scattering rates for a range of energies and maximum permissible drift time (which is related to the sum of the scattering rates, see section Calculation of Scattering Rates and Maximum Drift Time) between scattering events.

2. Set initial conditions and electron states (by starting with a thermalised electron distribution).

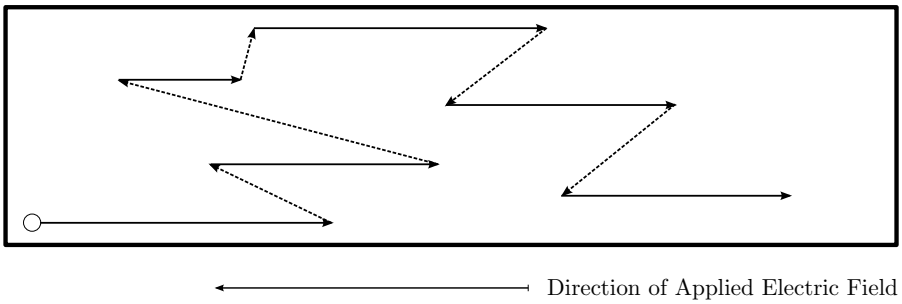

Figure 2.2) An example on how the wave-vector, and hence, momentum of an electron may change during the course of a simulation. Solid arrows indicate drift, dashed arrows indicate scattering.

3. Drift electrons for a random period of time (subject to constraints) by updating the wave-vector (and hence, momentum) and position of the electron.

4. Scatter electron (using Fermi's Golden Rule which assumes an instantaneous effect) based on the use of a random number generator to determine the scattering event that occurs.

Steps 3 and 4 may be repeated as required up to a set drift time, and for multiple electrons (see section 2.4 for details on performing this). Figure 2.2 is an example on how the wave-vector of an electron might change when this algorithm is used.

2.2.1. Calculation of Scattering Rates and Maximum Drift Time

In order to increase performance, scattering rates are pre-calculated for electrons in both the Γ valley and the upper valleys at energy "points" between $0eV$ and a maximum (dependent on the material and the energies the electron can potentially attain) at intervals of $2meV$ (though again, this is dependent on material and how much the scattering rates are liable to change across these intervals), and stored in a look-up table. Doing this removes the need to calculate the scattering rates for an electron every time it scatters, vastly decreasing the run time, at the

expense of accuracy. However, the error introduced through the use of this method is mitigated by choosing an appropriate value for the energy interval so that the difference between the scattering rates at two consecutive energy "points" is small.

Let $W_t(E_k)$ be the scattering rate for scattering mechanism t for an electron with energy E_k corresponding to wave-vector k. If we have a total of T scattering rates, we can determine the drift time of an electron between scattering events τ. *Tomizawa* states that the probability of an electron travelling for a time τ is

$$P(\tau) = W_T(E_k) \exp\left[-\int_0^\tau W_T(E_k)dt\right]. \tag{2.2.1}$$

where $W_T(E_k) = \sum_{t=1}^{n} W_t(E_k)$, the sum of all scattering rates (of which there are n) at a particular energy point [25]. Equation (2.2.1), however, has no analytical solution, due to $W_T(E_k)$ not being equal across all energies. In order to circumvent this, a new scattering mechanism is introduced, termed "self-scattering", which causes no changes to the electron state if selected. The self-scattering rate for each energy point is set so that the total scattering rate $W_T(E_k)$ becomes constant across all energies, so that

$$\Gamma = W_T(E_k) = \sum_{t=1}^{n+1} W_t(E_k) \ \ (\forall E_k). \tag{2.2.2}$$

where there are n scattering mechanisms, excluding self-scattering, which is the n+1th scattering mechanism. In order to minimise the effects of this self-scattering, Γ is set to the largest total scattering rate across the chosen energy range, thereby becoming energy independent in the following expressions. By substituting (2.2.2)

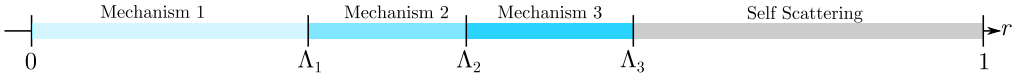

Figure 2.3) The storage of scattering probabilities can be thought of by placing the cumulative scattering probabilities on a number line, one after another. In this case, we have 3 scattering mechanisms, plus self scattering. For Λ_2, the probability of using mechanism 2 is added to that of mechanism 1. This allows for easy selection of a scattering mechanism using a uniform random number generator.

into (2.2.1), it is now possible to obtain an analytic solution, which is found to be,

$$P(\tau) = \Gamma e^{-\Gamma\tau}. \tag{2.2.3}$$

In order to be able to make use of the scattering rates in the selection of a scattering mechanism (which will be described in more detail in section 2.2.4), they have to be converted to scattering probabilities. Each scattering mechanism is assigned an integer index *(m)*. For each energy point, the code stores the rates cumulatively, normalised to Γ. Thus, for a scattering mechanism t when an electron has an energy E_k, we obtain a cumulative probability, $\Lambda_t(E_k)$,

$$\Lambda_t(E_k) = \frac{\sum_{j=1}^{m} W_j(E_k)}{\Gamma}, \tag{2.2.4}$$

noting that when $m = n+1$ (i.e. when calculating for self scattering) , $\Lambda_t(E_k) \equiv 1$. This provides a series of probabilities for a total of T mechanisms for a range of energies, where, for an electron with energy E_k, the probability of the mechanism denoted by index m being selected is $\Lambda_m(E_k) - \Lambda_{(m-1)}(E_k)$ (where $\Lambda_0(E_k) = 0$), and the probability of self-scattering occurring is $1 - \Lambda_n(E_k)$. Figure 2.3, through the use of a number line, illustrates how the probabilities are stored in the program.

2.2.2. Initial Electron States

In order to determine the electronic properties of the material, the algorithm attempts to start with a realistic electron distribution. Using the Fermi-Dirac function (allowing for three degrees of freedom by introducing a factor of 3/2),

$$f(E_k) = \frac{1}{1 + e^{[(E_k - E_F)/(3k_BT/2)]}} \tag{2.2.5}$$

where k_B is the Boltzmann constant and T is the lattice temperature, and $0 \leq f(E_k) \leq 1$. We assume that $e^{[E_k/(3k_BT/2)]} \gg 1$ and that the Fermi energy, E_F, corresponds with the minima of the lowest conduction band, and so is set to 0. Thus, we obtain,

$$f(E_k) = \frac{1}{e^{[E_k/(3k_BT/2)]}}. \tag{2.2.6}$$

Rearranging, we obtain,

$$E_k = -\frac{3k_BT}{2} \ln [f(E_k)] \tag{2.2.7}$$

As it is known that $f(E_k)$ is a value between 0 and 1, we then use a uniform random number generator to determine the energy of any particular electron. Should the random number generator pick 0, then a new random number is generated, to avoid calculating $ln\,[0]$. The electron wave-vectors are then determined from this energy, the magnitude is determined through the use of the selected band-structure approximation, whilst the direction of the wave-vector is determined through the use of two more randomly generated numbers, giving all directions an equal probability of being selected.

2.2.3. Electron Drift

A new drift time is determined each time an electron enters a drift phase of the algorithm, through the use of the solution of equation 2.2.3 in terms of τ,

$$\tau = -\frac{ln\,(r)}{\Gamma}. \tag{2.2.8}$$

where r is a random number generated by a uniform random number generator between 0 and 1 (again, generating a new number if 0 is selected). As the applied field is known to be constant throughout the device, using τ, the change in the wave-vector of the electron can be calculated using the equation,

$$\Delta\mathbf{k} = -\frac{e\mathbf{F}}{\hbar}\tau. \tag{2.2.9}$$

where $\Delta\mathbf{k}$ is the change in the wave vector over this drift step, e is the electronic charge and $\mathbf{F}$ is the applied field vector. For simplicity, we assume that the field is applied solely in the x-direction, and thus, only altering the x component of the wave-vector, giving,

$$\Delta k_x = -\frac{eF_x}{\hbar}\tau \tag{2.2.10}$$

It is assumed that the rate of change in k_x is constant throughout the drift step, so when calculating the distance the electron has moved in the x-direction, we assume that the electron moves with a constant velocity, corresponding to $k_{x,(inital)} + \frac{\Delta k_x}{2}$ (where $k_{x,(inital)}$ is the wave-vector in the x-direction before the drift step started),

that is,

$$x_{final} = x_{initial} + v\left(k_{x,(inital)} + \frac{\Delta k_x}{2}\right) \tag{2.2.11}$$

2.2.4. Electron Scattering

In order to determine which scattering mechanism is to be used, a random number, r, between 0 and 1 is generated using a uniform generator. As the algorithm has generated cumulative scattering probabilities, $\Lambda_n(E_{\mathbf{k}})$, the condition for selecting a scattering mechanism with index m becomes,

$$\Lambda_{m-1}(E_{\mathbf{k}}) < r \leq \Lambda_m(E_{\mathbf{k}}). \tag{2.2.12}$$

It is implied that "self-scattering" will occur if the random number generated is higher than that the sum of all the scattering probabilities.

Once the scattering mechanism has been chosen, the wave-vector is updated accordingly. In all cases, the energy change is straight forward and hence the magnitude of the after-scattering wave-vector, $|\mathbf{k}'|$, is easily obtainable. However, the determination of the direction of the vector can be more difficult to calculate. Two scattering angles are calculated in order to detemine this direction, the polar angle, θ', and the azimuthal angle, ϕ', their relation to the before- and after-scattering states can be seen in figure 2.4. The azimuthal scattering angle, ϕ', is always determined by the relation,

$$\phi' = 2\pi r \tag{2.2.13}$$

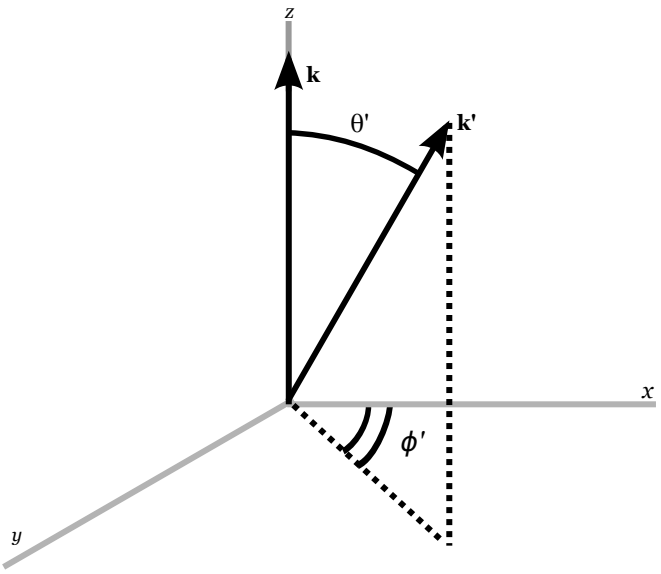

Figure 2.4) An illustation of sample polar (θ') and azimuthal (ϕ') scattering angles between the initial ($\mathbf{k}$) and final ($\mathbf{k}'$) electron wavevector states. The azimuthal angle is in the $x-y$ plane only, and is always perpendicular to the inital state.

where r is a random number between 0 and 1, generated via a uniform random number generator. This is due to the fact that the transition rates are always independent of the azimuthal angle. However, the determination of the polar scattering angle of scattering, θ', depends on whether the scattering mechanism is *isotropic* or *anisotropic*.

2.2.4.1. Isotropic Scattering

Isotropic scattering mechanisms, such as Non-Polar Optical and Acoustic Phonon scattering, are mechanisms in which the electron wave-vector has equal probability of pointing in any direction after scattering. In these cases, the polar angle can simply be determined by the relation

$$\cos(\theta') = 1 - 2r \tag{2.2.14}$$

As there is an equal probability for any scattering angle to occur, we assume that the obtained θ' and ϕ' are the polar and azimuthal angles of the new direction

of **k'**, rather than the change in these angles from the initial direction.

2.2.4.2. Anisotropic Scattering

For the anisotropic scattering mechanisms, Polar Optical Phonon, Impurity and Piezoelectric scattering, the determination of θ is more complex than having a direct relationship with a uniform random number generation. The probability of scattering through a polar angle between 0 and θ' can be found by solving $W_t(E_k)_{\theta:0-\theta'}/W_t(E_k)_{\theta:0-\pi}$ (where the θ subscript denotes the limits of the polar integration) in terms of $cos(\theta')$. It has been worked out for POP scattering using the parabolic band-structure to be [25]

$$\cos(\theta') = \frac{1 + f - (1 + 2f)^r}{f} \tag{2.2.15}$$

where r is a random number between 0 and 1, and f, in terms of the electron energy before ($E_{\mathbf{k}}$) and after ($E'_{\mathbf{k}}$) scattering, is defined as,

$$f = \frac{2\sqrt{E_{\mathbf{k}} E_{\mathbf{k}'}}}{\left(\sqrt{E_{\mathbf{k}}} - \sqrt{E_{\mathbf{k}'}}\right)^2}. \tag{2.2.16}$$

Similarly, for Impurity Scattering, again, for the parabolic band structure, [25]

$$\cos(\theta') = 1 - \frac{2r}{1 + (1 - r)\left(\frac{2k}{q_D}\right)^2}. \tag{2.2.17}$$

where q_D is the Debye length, given by

$$q_D = \sqrt{\epsilon_s k_B T / e^2 n} \tag{2.2.18}$$

where n is the electron concentration. For Piezoelectric scattering, one can obtain, using the parabolic band structure,

$$\cos(\theta') = \frac{1}{2k^2}\left(2k^2 + q_0^2\left(1 - \mathrm{Exp}\left[1 + \chi r + W_0\left(-e^{-1-\chi r}\right)\right]\right)\right) \tag{2.2.19}$$

where $\chi = \ln\left[1 + \frac{4k^2}{q_0^2}\right] - \frac{4k^2}{q_0^2+4k^2}$, $W_0(x)$ is the Lambert W-function (with the zero denoting the principal branch) and q_0 is the electronic screening, given by $\sqrt{2m^*\omega_L/\hbar}$. (See Appendix A for the derivation of the Piezoelectric scattering angle expression).

When the scattering angles have been decided, it is very difficult to work directly in the laboratory/original frame of reference $\left(k_x^L, k_y^L, k_z^L\right)$. It is much easier to use a rotated frame, denoted by $\left(k_x^r, k_y^r, k_z^r\right)$, rotated around the origin of the laboratory frame so that the initial wave-vector is parallel to the new z-axis. The relationship between the laboratory frame and the rotated frame is characterised by two angles of rotation, angle α clockwise round the k_x^L axis and angle β clockwise round the k_z^L axis, as shown in Figure 2.5.

The $\mathbf{k}'$ vector can then simply be determined in the rotated frame as (where k' is the magnitude of the final vector which already has been calculated),

$$\mathbf{k}' = (k'\sin\theta\cos\phi, k'\sin\theta\ \sin\ \phi, k'\cos\theta). \tag{2.2.20}$$

In order to obtain the direction in the laboratory frame (so we can apply the field simply in the next drift step), we need to multiply this by a transformation matrix.

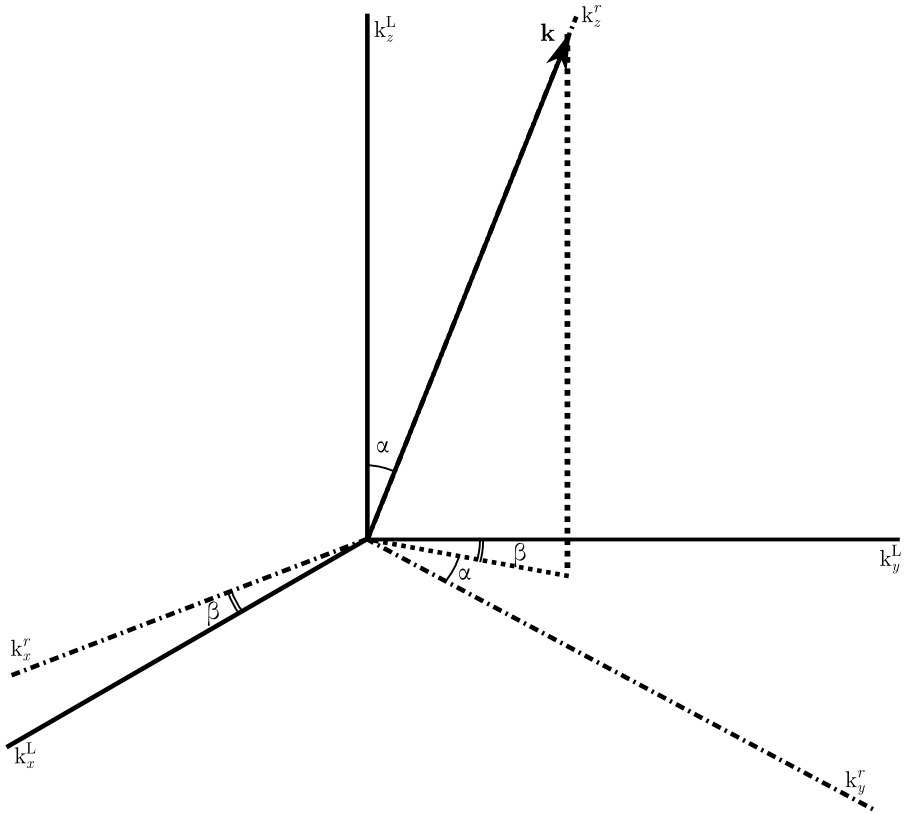

Figure 2.5) Comparison between the k^L and k^r frames. The z-axis in the rotated frame is set so that it is co-incident with the initial wave-vector.

The transformation matrix from the laboratory frame to the rotated frame is,

$$\begin{pmatrix} \cos(\beta) & \cos(\alpha)\sin(\beta) & \sin(\alpha)\sin(\beta) \\ -\sin(\beta) & \cos(\alpha)\cos(\beta) & \sin(\alpha)\cos(\beta) \\ 0 & -\sin(\alpha) & \cos(\alpha) \end{pmatrix}. \tag{2.2.21}$$

While we may not necessarily know what these angles are, the trigonometric functions can be replaced in terms of k (the original wave-vector) and its orthogonal

components, k_x, k_y and k_z in the laboratory frame.

$$\begin{aligned}
\sin\,\alpha &= \frac{\sqrt{k_x^2+k_y^2}}{k} \\
\cos\,\alpha &= \frac{k_z}{k} \\
\sin\,\beta &= \frac{k_x}{\sqrt{k_x^2+k_y^2}} \\
\cos\,\beta &= \frac{k_y}{\sqrt{k_x^2+k_y^2}}.
\end{aligned} \tag{2.2.22}$$

Finally, the inverse of this transformation matrix is found, and by right-multiplying by equation (2.2.20), we obtain $\mathbf{k}'$ in the laboratory frame, as shown in equation (2.2.23).

$$\mathbf{k}' = \begin{pmatrix} k'_x \\ k'_y \\ k'_z \end{pmatrix} = \begin{pmatrix} \frac{k_y}{\sqrt{{k_x}^2+{k_y}^2}} & \frac{k_x k_z}{k\sqrt{{k_x}^2+{k_y}^2}} & \frac{k_x}{k} \\ \frac{-k_x}{\sqrt{{k_x}^2+{k_y}^2}} & \frac{k_y k_z}{k\sqrt{{k_x}^2+{k_y}^2}} & \frac{k_y}{k} \\ 0 & \frac{-\sqrt{{k_x}^2+{k_y}^2}}{k} & \frac{k_z}{k} \end{pmatrix} \begin{pmatrix} k'\sin\theta\cos\phi \\ k'\sin\theta\sin\phi \\ k'\cos\phi \end{pmatrix}. \tag{2.2.23}$$

2.3. Bulk Single Electron Monte Carlo Simulation

The simplest model that can be used to simulate the electron transport based on this algorithm is to track the movement and scattering of a single electron, giving rise to a Single Electron Monte Carlo (SMC) simulation. While the usefulness of the SMC simulation is limited, the main advantage of using this method is its speed. For the work presented in this thesis, the SMC was used as a tool to gain experience in Monte Carlo simulations and as an effective test mechanism when adding new features that would be later implemented in more sophisticated codes.

The base algorithm as described in section 2.2 is performed on a single particle until the simulation has been run for a specified period of time within the simu-

lation, and then the data generated by the simulation is analysed and output for the applied field. The SMC code is often looped over a series of applied fields to obtain field dependence data.

2.3.1. Output

Whilst the data that can be obtained from the SMC is limited to steady state transport properties, time averaged velocities and energies over the whole simulation time can be obtained.

2.3.1.1. Velocity

Equation (1.1.8) states that the velocity of an electron in **k**-space is

$$\langle v \rangle = \frac{1}{\hbar} \frac{dE_{\mathbf{k}}}{d\mathbf{k}}. \tag{2.3.1}$$

Over one drift step j, with drift time τ, it is assumed that the rate of change of energy is constant. As the change in energy over τ is small, we make the approximation $\frac{dE_{\mathbf{k}}}{d\mathbf{k}} = \frac{\Delta E_{\mathbf{k}}}{\Delta \mathbf{k}}$ where the Δ symbolises this small change, rather than a derivative. Using (2.2.9) as a substitution for $\Delta\mathbf{k}$,

$$\langle v \rangle_j = -\frac{\Delta E_{\mathbf{k}}}{e\mathbf{F}\tau} = -\frac{E_f - E_i}{e\mathbf{F}\tau}, \tag{2.3.2}$$

where $\Delta E_{\mathbf{k}} = E_f - E_i$, the difference between the initial and final energies within the drift step.

In order to obtain the time-averaged velocity for the whole simulation consisting of n drift steps amounting to a total simulation time T, the total sum of the distance

traveled in each drift step is divided by the total simulation time. Thus,

$$\begin{aligned} \langle v \rangle_T &= \frac{1}{T} \sum_{j=1}^{n} \langle v \rangle_{\tau_j} \tau_j \\ &= -\frac{1}{e\mathbf{F}T} \sum (E_{f_j} - E_{i_j}). \end{aligned} \tag{2.3.3}$$

After each time step, in order to calculate the average velocity, the algorithm calculates $E_f - E_i$ and stores it.

2.3.1.2. Energy

Making the same assumption that the rate of change of energy is constant over a drift time τ, the average energy of an electron during a drift step is simply,

$$\langle E \rangle_j = \frac{E_i + E_f}{2}. \tag{2.3.4}$$

Thus, to get an average energy over the entire simulation time, T,

$$\langle E \rangle_T = \frac{1}{T} \sum_{j=1}^{n} \langle E \rangle_j \tau_j = \frac{1}{T} \sum_{j=1}^{n} \frac{E_{i_j} + E_{f_j}}{2} \tau_j. \tag{2.3.5}$$

After each time step, in order to calculate the average energy, the algorithm calculates $E_f + E_i$ and stores it.

2.4. Bulk Ensemble Monte Carlo Simulation

Whilst the SMC code is useful for quickly obtaining transport properties of materials in the steady-state regime, it lacks the ability to determine transient transport properties of materials and also is unable to generate distribution functions of various electron parameters. The Ensemble Monte-Carlo (EMC) code seeks to solve

these issues by simulating a system with many particles simultaneously, taking "snapshots" of the distribution of electrons at a specified intervals in order to be able to track the evolution of the system.

2.4.1. Ensemble Algorithm

The EMC simulation treats all electrons as separate entities that have no effect on each other - essentially running many SMC simulations at the same time. The pre-calculation of scattering rates is only done once, as it is assumed valid for all electrons. After this step, each electron is taken in turn, and then simulated using steps 3 and 4 from the base algorithm for a period of one time step, dt. If this time dt occurs before the end of a drift step, the drift step is "paused" and not allowed to run to the end until the next time step. Once all electrons have completed the time step (meaning that all electrons have been simulated for the same period of time), a snapshot of the electron distribution and other parameters can be captured - which allows for the monitoring of the time evolution of the transport properties.

The base algorithm is therefore amended for use in the EMC simulation and is listed below.

1. Calculate scattering rates for a range of energies and maximum permissible drift time between scattering events,

2. Set initial conditions and electron states (by starting with a thermalised electron distribution).

3. Select each electron in turn and repeat these steps on each electron until the end of the current time step.

    a) Drift electron until the time of the next scattering event or the end of

the time step (whichever comes first) by updating the wave-vector (and hence, momentum) and position of the electron,

b) Scatter electron (using Fermi's Golden Rule which assumes an instantaneous effect) based on the use of a random number generator to determine the scattering event that occurs.

4. If required, output average velocities/energies and electron distributions at the end of the time step.

Step 3 is repeated for each electron, whilst steps 3 and 4 are repeated for each time step. As the EMC simulation treats all electrons as independent from one another, it is possible to implement a multi-threaded approach to step 3 of the algorithm, that is, run this simulation with multiple electrons at once, in order to speed up the simulation. An alternative to this is, if the simulation is being run for multiple field strengths, run simulations for these different applied field strengths in parallel. In this case, step 1 would only need to be performed once for all fields, before the simulation runs steps 2 - 4 for all fields in parallel.

2.4.2. Output

The EMC code produces ensemble averaged data at the required point in time of the simulation, based on the distribution of the system. To calculate the average velocity and energy of the electrons in the ensemble, one simply needs to take the instantaneous properties and average over all n electrons.

$$\langle v \rangle_t = \frac{1}{n} \sum_{i=1}^{n} \frac{1}{\hbar} \frac{\partial E(k)_i}{\partial k_{x,i}}. \tag{2.4.1}$$

$$\langle E(k)\rangle_t = \frac{1}{n}\sum_{i=1}^{n} E(k)_i. \tag{2.4.2}$$

The EMC simulation is also capable of outputting valley occupancy data, and the distribution of the velocities and energies of the electrons, and can be taken at the end of any time step. To obtain time evolution properties, this needs to be done at multiple points in the simulation (as described in section 2.4.1).

2.5. 1D $n^+ - i - n^+$ Diode Monte Carlo Simulation

The simplest device that can be simulated is the 1D device, where a small length of a material is placed between two doped contacts made from the same material. To keep things as simple as possible, the device is assumed to have infinite dimensions perpendicular to the potential to be applied, as illustrated in figure 2.6.

2.5.1. Device algorithm.

In order to simulate a device, the bulk algorithm has to be amended to take into account the limited dimensions of the device.

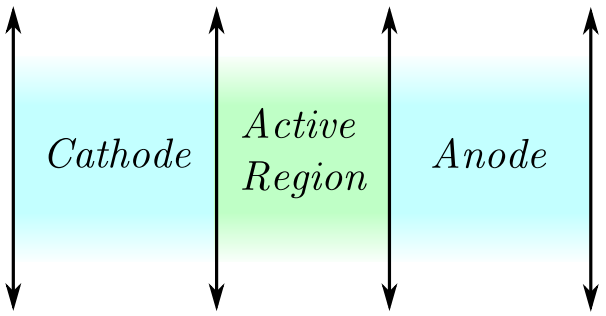

Figure 2.6) A diagram showing the layout of the simulated diode. The blue shaded areas are n-doped regions, the green shaded active region is an undoped intrinsic region.

1. Calculate scattering rates for a range of energies and maximum permissible drift time between scattering events,

2. Set up the device, create the mesh, and set up the super-particle states.

3. Set initial conditions (charges/fields per grid spacing) and electron states (by starting with a thermalised electron/distribution of electrons).

4. Select each particle in turn and repeat these steps on each electron until the end of the current time step or electron has left the device.

    a) Drift electron until the time of the next scattering event or the end of the time step (whichever comes first) by updating the wave-vector (and hence, momentum) and position of the electron,

    b) Remove the electron if it has left the device (either though the anode or the cathode)

    c) Scatter electron (using Fermi's Golden Rule which assumes an instantaneous effect) based on the use of a random number generator to determine the scattering event that occurs.

5. Determine number of electrons to re-introduce into the device and add them, setting initial conditions for these in the same was as was done for the initial electrons step 3.

6. Determine the charge and potential at each grid node.

7. Output particle data (if required at this point).

Steps 4 to 7 can be repeated as required. Parallel calculations can be performed in step 4, in a similar fashion to the EMC code, as the electrons are again deemed to be independent of each other.

2.5.2. Time Step and Mesh Size Determination

Unlike the bulk material simulations, the device has a potential applied across a finite length, rather than a field across an infinite length. In order to accommodate for the variable field across the length of the device, the algorithm divides the device into a grid of discrete "strips" or cells. It is assumed that the conditions are identical across the whole area of a cell, reducing the need to determine the properties of each electron in turn.

In order to determine a suitable grid spacing, a series of stability criteria must be met. First, a suitable time step, Δt, must be selected, that is, the simulation time between re-calculation of the field across each cell. If the time step is too long, the field won't be able to react to the particles' movement in the device fast enough for a meaningful simulation. In order to determine the time step, the plasma frequency of the material must be determined using the relation, [25]

$$\omega_p = \sqrt{\frac{e^2 n}{\epsilon_s m^*}} \tag{2.5.1}$$

where e is the electronic charge, n is the largest specified carrier density, ϵ_s is the static dielectric constant and $m*$ is the smallest effective mass that the electron can encounter. The time step must be much smaller than $1/\omega_p$.

A suitable cell length (or mesh size), Δx, must also be obtained. As the model needs to be able to react to the movement of charge throughout the device, the resolution must be sufficiently fine to be able to react to any variation in charge. Therefore, the cell lengths must be smaller than the wavelengths associated with this movement of charge. *Tomizawa [25]* states that the smallest wavelength is comparable to the Debye length of the system (equation 2.2.18) [25], thus, for the

simulation to remain stable, the cell length must be selected to be smaller than the Debye length. However, using a cell length that is too small for the time step chosen may also result in the inability for the simulation to adapt to the changing conditions of the system quickly (as a particle may be able to move over more than one cell in a time step without the field being re-calculated), so care has to be taken when selecting this cell length. In order to ensure that the particles are unable to "skip over" a cell, the following relation should be used to validate the choices of Δt and Δx,

$$\Delta x > v_{max} \times \Delta t \tag{2.5.2}$$

where v_{max} is the maximum velocity that the electron can be expected to gain during the simulation.

2.5.3. Super-particles

If the simulation assumed that all particles had the charge of an electron, running this simulation with typical doping levels would potentially require the simulation of billions of particles. In order to reduce this requirement, each particle in the simulation is treated as a "super-particle", that is, a particle that represents a multiple of particles. In charge and potential calculations, each super-particle is treated as if it holds the sum of the charges of the particles it represents, but when the super particle is subjected to drift and scattering, it is treated as if it only has the charge of a single electron.

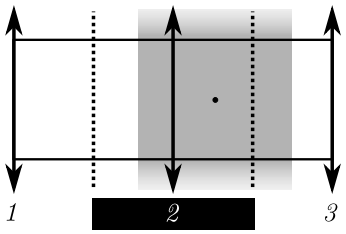

Figure 2.7) A representation of the cloud-in-cell scheme. The dashed lines are cell boundaries, the solid lines are the grid nodes where the charge profile is taken from, the dot represents a super-particle, and the grey shaded box represents the area the charge is spread over. The charge contributes to the profile of the cell it resides in, so in this case, there is a ~80% contribution to cell 2, and a ~20% contribution to cell 3.

2.5.4. Potential and field strength determination

In the device, the field is dynamic, unlike the bulk simulation, and has to be constantly updated. To do this, the algorithm has to solve Poisson's equation but in order to do this, the charge density profile across the device has to be determined at the centre of each cell, or grid node. A "cloud-in-cell" approach is used to do this - each super-particle representing n particles with charge q is assumed to create a cloud of electronic charge around it, spread uniformly across an area corresponding to one cell width, Δx, with the super-particle in the center of the charge cloud. Unless the particle is on a cell boundary, then this cloud will have an influence on two cells. An illustration of the cloud in cell approach can be seen in Figure 2.7.

In order to obtain the field across a cell, Poisson's equation in one dimension has to be solved for the potential, ψ

$$\frac{\partial^2 \psi}{\partial x^2} = -\frac{\rho}{\epsilon_s} \tag{2.5.3}$$

where ρ is the charge density. By allowing $\partial x^2 \rightarrow \Delta x^2$ (which can be done as the mesh is equally spaced in this model), $\partial^2 \psi$ can then be taken to be the difference

of two changes of potential, that is,

$$\partial^2\psi \rightarrow \Delta\psi_{i-1\rightarrow i} - \Delta\psi_{i\rightarrow i+1} = (\psi_{i-1} - \psi_i) - (\psi_i - \psi_{i+1}) = \psi_{i-1} - 2\psi_i - \psi_{i+1} \quad (2.5.4)$$

where i represents the index of a grid node. Substituting this into (2.5.3) yields a set of linear equations that can be used to determine the potential at a grid node i, that can be solved numerically through the use of matrix methods.

$$\frac{\psi_{i-1} - 2\psi_i - \psi_{i+1}}{\Delta x^2} = -\frac{\rho_i}{\epsilon_s}. \quad (2.5.5)$$

This solution works provided that the potential at either extreme of the device, ψ_1 and ψ_{max} is provided. In the case of this device, ψ_1 is set to zero, while ψ_{max} is set to the potential that is applied across the device. The field between two grid nodes can then be simply worked out as (for a particle between points i and $i+1$)

$$f_x = \frac{\psi_{i+1} - \psi_i}{\Delta x} \quad (2.5.6)$$

2.5.5. Initial Conditions

Like in the bulk simulations, the energy distribution and wave-vectors of the particles is determined according to a thermalised distribution. However, unlike the bulk simulations, where the initial position of the particles wasn't important (just the wave-vector), in the device, due to it's finite dimensions in one direction, position becomes very important. In the device, the super-particles are uniformly placed in the cells in the doped n^+ regions only, in order to balance out the positive charge that is caused by the uniform doping of the contacts. This ensures that the

device starts with a uniform net zero charge, and therefore a uniform electric field across the device when the potential is applied. No super-particles are injected into the intrinsic (active) region as the lack of dopants in the region means it is already electrically neutral.

2.5.6. Monte-Carlo dynamics

The Monte-Carlo based routines, (i.e. the drift and scattering regimes) are very similar to those performed in the bulk algorithms. However, due to the introduction of variable fields and the mesh, the routines have had to be modified. In the drift subroutine, the code now has to check the field across the cell that the particle is currently in, rather than use a constant field. If the particle crosses a cell boundary in the middle of a drift, however, the field in its initial cell is still assumed to apply to the particle until the end of the drift as it would be very difficult to determine the intermediate velocity of the particle at the cell boundary, which would be required in order to be able to work out the average velocity of the particle in both phases of the drift.

In the scattering routine, it is assumed that as the intrinsic region is devoid of all dopants, that impurity scattering is negligible, and as such, if the code selects the impurity scattering mechanism whilst the particle to be scattered is in the intrinsic region, self-scattering (i.e. no change) occurs instead. Conversely, the impurity scattering is considered to be large in the doped region, as the main contributor to the impurity scattering is considered to be the charged dopants.

Finally, the position of the particles is always tracked, and if the particle is detected to have left the bounds of the device in the x-direction (i.e. parallel to the field), then the particle is removed from the simulation.

2.5.7. Dynamic Electron Injection

Whilst particle removal is performed during the Monte-Carlo phases of the algorithm, no injection of particles is performed. In order to avoid the device being depleted of carriers (which would be entirely unphysical), a routine is executed before the charge and potential distributions are calculated that determines how many particles have left the device via the anode and the cathode and injects particles back into the contacts. The routine decides on the number of particles to inject by applying the principle of charge neutrality, that is, it attempts to maintain a charge neutral area at the extremes of either contact. When particles are injected into the contacts, their initial states are set in the same way as when the particles are initialised at the beginning of the simulation (see section 2.2.2).

2.5.8. Output

The output of the device code is similar to that of the EMC code, however, it can average over cells as well as over the whole device, so that a profile of the device can be built. Data that can be output from the device simulation includes velocity, energy and valley occupancy averaged over the entire simulation or over each cell to create a profile, and charge and potential profiles. This can be done at each time step, which allows for the observation of the time evolution of the system.

2.6. Summary

This chapter has demonstrated how the Monte Carlo method can be implemented in electron transport simulations, in bulk materials, and simple devices. The relative merits of the different algorithms have been discussed, while the use of a single

electron Monte Carlo algorithm is tempting due to its very low run times, the range of data that can be extracted is limited to time averaged velocity, energy and valley occupancy data in the steady-state regime. The Ensemble Monte Carlo method produces a range of output, providing ensemble averaged data at any point in time, which allows for both the steady-state and transient transport properties to be determined. Of course, this has implications for the run time, though this becomes less of an issue when parallelisation is introduced. The use of this method to simulate a one dimensional device has been also been described, where the field can vary across different sections of the device. Through the use of finite element methods and coupling the system with a Poisson solver for the potential calculation, we have demonstrated how the field profile across the system can be calculated, thus allowing for such systems to be successfully modelled.

Chapter 3
The Cosine Band-structure Approximation

It is well known that the band-structure of GaN is highly non-parabolic around the Γ point, however, the use of the well known **k.p** band-structure approximation does not provide a satisfactory approximation to the band-structure, missing vital features of the structure that have been postulated to produce negative effective mass transport in GaN. Therefore, to accurately simulate electron transport in GaN, full-band structure simulations have been used. While producing accurate results, these simulations are computationally expensive to run due to the numerical integrations involved throughout the simulation.

In 2005, *Ridley*, *Schaff* and *Eastman* suggested the use of a cosine band-structure approximation [36]. This cosine band model provides an approximation that is in close agreement with that of the actual band-structure of GaN as calculated by empirical pseudo-potential (ESP) methods [18], and takes the form:

$$E_{\mathbf{k}} = \frac{E_B}{2}(1 - \cos(ka)). \tag{3.0.1}$$

where $E_{\mathbf{k}}$ is the energy of an electron with wave vector $\mathbf{k}$, E_B is the energy difference between the energy minimum and maximum of the valley, k is the magnitude of the wave vector, and a is the c-axis hexagonal lattice constant. It turns out that this is an excellent approximation to the Γ-valley in GaN [3], and can also be adapted for other materials that exhibit a similar band-structure.

We therefore begin this chapter by exploring the use of a novel band-structure approximation that closely resembles that of the band-structure around the Γ point. The inflection point in the valley, postulated to give rise to a negative effective

mass effect at higher electron energies is taken into account. We continue by making comparisons between the cosine band-structure approximation and other, well-established analytic approximations (the parabolic and **k.p** approximations) and analysing some of the properties of the approximation. We close the chapter by deriving scattering rates based on this band-structure approximation in order to be able to take advantage of these properties in Monte Carlo simulations.

3.1. Approximation Properties

3.1.1. $E - k$ Relation

Figure 3.1 depicts the $E - \mathbf{k}$ relations of the cosine model and the more established parabolic and **k.p** approximations. At first glance, it can be seen that the cosine band-structure approximation has a very similar profile to that of the **k.p** approximation at low energies. A simple benefit of the use of the cosine approximation is that there is a inherent maximum attainable energy within the valley, E_B, which is not the case in other approximations. This ensures that in Monte Carlo simulations the electrons in the Γ-valley will not be able to attain a higher energy then would be physically possible if the electron was to remain in this valley. However, the cosine band-structure approximation is of particular value for GaN because it contains the inflection point necessary to facilitate negative effective-mass transport, unlike the parabolic approximation, which assumes a fixed effective mass at all points in the valley, and the **k.p** approximation, which does feature a varying effective mass, however, negative effective mass states do not feature in this approximation. We will return to the topic of effective masses later (in section 3.1.3).

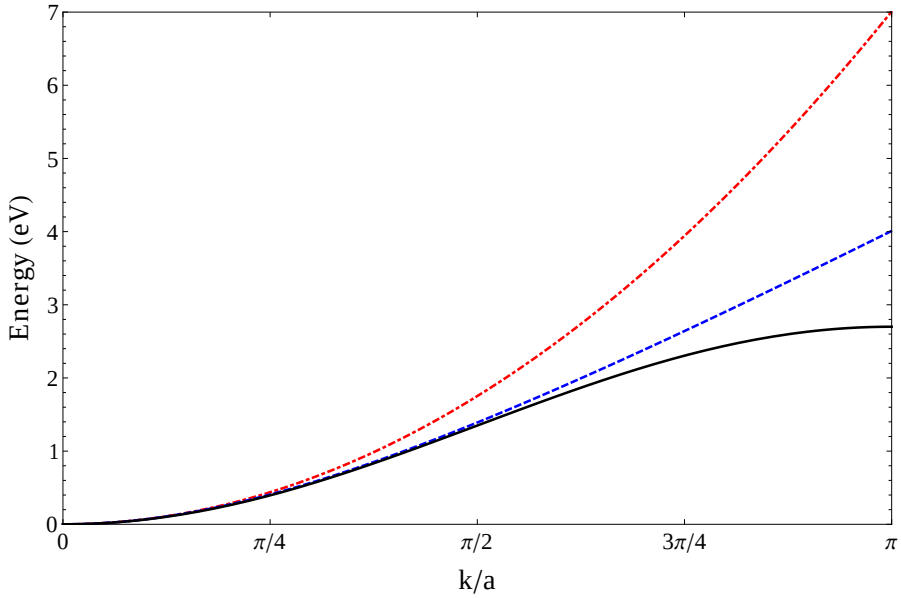

Figure 3.1) An E-**k** diagram of the parabolic (red, dot-dashed line), **k.p** (blue dashed line) and cosine (black solid line) band-structure approximation, when GaN parameters are used at a temperature of 300 K. For the parabolic and **k.p** approximations, the effective mass of the electron at the Γ point is set to $0.2m_e$, and for the cosine approximation, $a = 5.186\,\text{Å}$ and $E_B = 2.7\,\text{eV}$

3.1.2. Density of States

We can derive the density of states for the cosine band structure. The density of states, dN, per unit volume is

$$dN = \frac{1}{2}\left(\frac{k}{\pi}\right)^2 d\mathbf{k}. \tag{3.1.1}$$

Rearranging equation (3.0.1) in terms of $\mathbf{k}$, we get,

$$\mathbf{k} = \frac{1}{a}\cos^{-1}\left(1 - \frac{2E_\mathbf{k}}{E_B}\right). \tag{3.1.2}$$

Differentiating (3.1.2) with respect to E,

$$\frac{d\mathbf{k}}{dE_\mathbf{k}} = \frac{1}{E_B a\sqrt{(E_\mathbf{k}/E_B) - (E_\mathbf{k}/E_B)^2}}. \tag{3.1.3}$$

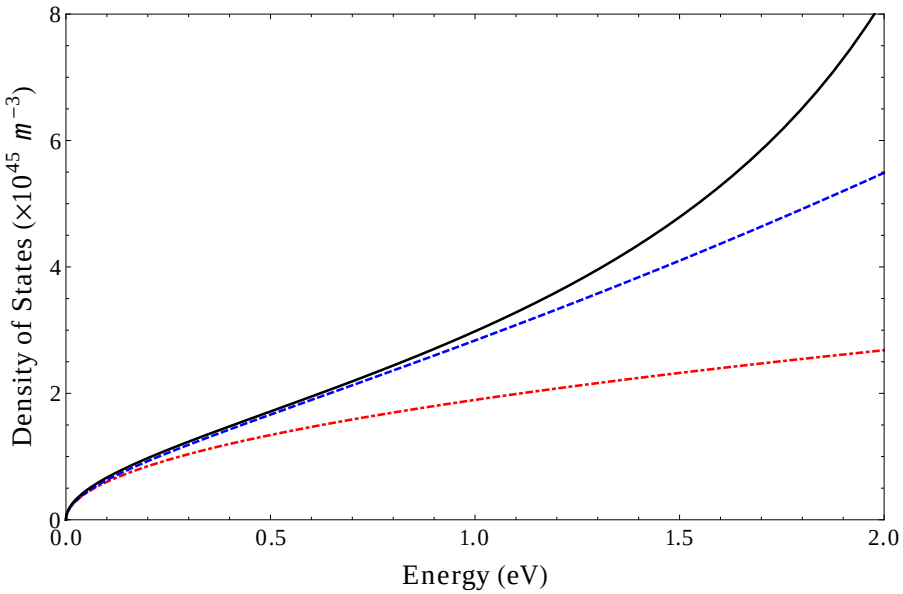

Figure 3.2) The density of states with respect to energy for the parabolic (red dot-dashed line), **k.p** (blue dashed line) and cosine (black solid line) band-structure approximations (using parameters from Figure 3.1).

Substituting (3.1.2) and (3.1.3) into (3.1.1), and simplifying, we get the Density of States for a cosine band-structure,

$$N(E_{\mathbf{k}}) = \frac{dN}{dE_{\mathbf{k}}} = \frac{\left[\cos^{-1}\left(1 - 2E_{\mathbf{k}}/E_B\right)\right]^2}{2E_B a^3 \pi^2 \sqrt{\left(E_{\mathbf{k}}/E_B\right)^2 - \left(E_{\mathbf{k}}/E_B\right)}}. \tag{3.1.4}$$

Figure 3.2 shows a comparison of the density of states calculated from different band-structure approximations. It can be seen that the density of states for all three approximations are closely matched at lower energies, deviating for the various models at larger energies. It is important to note that at energies close to the band edge (E_B), the density of states for the cosine band-structure approximation tends towards infinity and the approximation loses validity, so this approximation should not be used too close to the band edge.

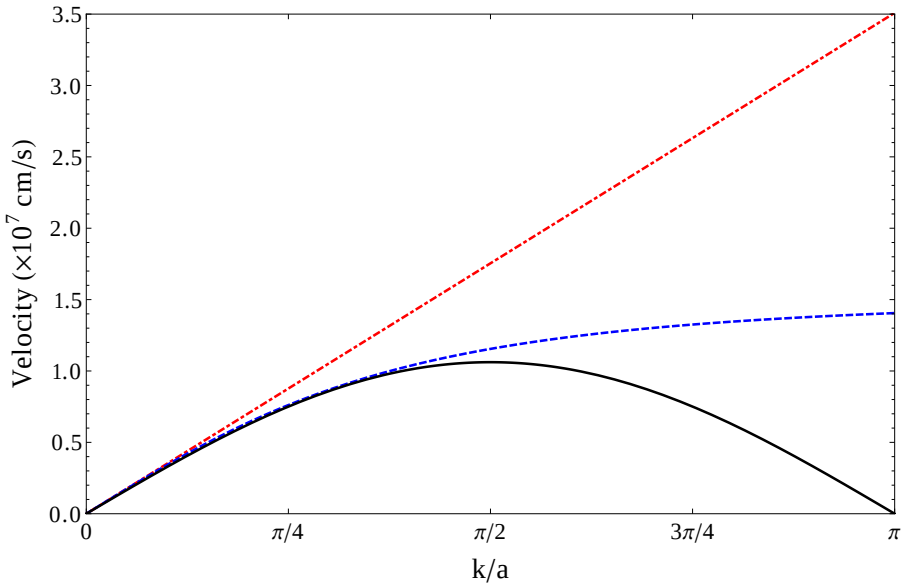

Figure 3.3) A plot of the velocity of an electron against k for the parabolic (red dot-dashed line), **k.p** (blue dashed line) and cosine (black solid line) band-structure approximations (using parameters from Figure 3.1) in the direction of **k**.

3.1.3. Negative effective-mass transport

As shown in chapter 1, we can get a relationship between the velocity of an electron and it's position in **k**-space.

$$\mathbf{v}(\mathbf{k}) = \frac{1}{\hbar}\frac{dE_{\mathbf{k}}}{d\mathbf{k}}. \tag{3.1.5}$$

For a cosine-approximated valley, the velocity of the electron in the direction of **k** is:

$$v(k) = \frac{E_B a}{2\hbar}\sin(ka). \tag{3.1.6}$$

By referring to figure 3.3, it can be seen that at higher energies, there is a deceleration of the electron, as opposed to an acceleration, something that isn't observed in the parabolic and **k.p** approximations. This effect of deceleration solely due to the band-structure is caused by what is known as negative effective

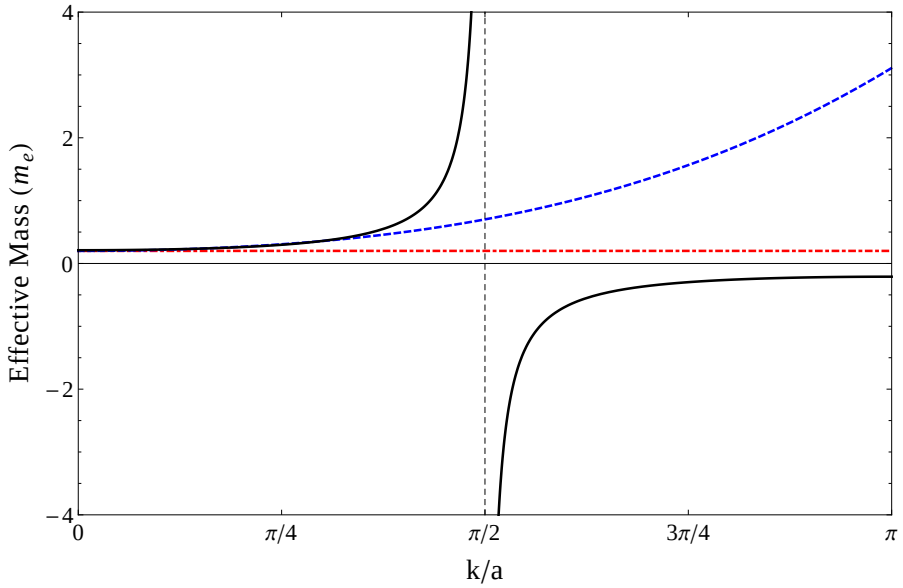

Figure 3.4) The calculated effective mass of an electron for different values of k when the parabolic (red dot-dashed), **k.p** (blue dashed) and cosine (black solid) approximations (using parameters from Figure 3.1).

mass states, through analogy with Newton's second law, the acceleration of the electron is in the opposite direction to the force on the electron caused by the applied electric field. This negative effective mass effect was originally postulated by Krömer [55], and it has discussed at length by *Ridley et. al.*[3, 36]. Using (1.1.11), the effective mass of the electron when in a valley approximated using the cosine band structure is,

$$m^* = \frac{2\hbar^2}{a^2 E_B \cos(ka)}. \tag{3.1.7}$$

A comparison between the different band structure approximations, illustrating the how the effective mass is related to the wave-vector of an electron can be seen in figure 3.4, where the occurrence of negative effective mass states can clearly be seen when using the cosine band-structure approximation.

3.2. Derivation of Scattering Rates

The use of this new analytic band-structure approximation requires the derivation of new scattering rates. We use Fermi's Golden Rule, which was introduced in chapter 1, to derive the rates, as it provides a mathematical expression for the probability of an electron transitioning from an initial state, $\mathbf{k}$, to a particular final state $\mathbf{k}'$ via some scattering mechanism. Fermi's Golden Rule can be expressed in the form,

$$S\left(\mathbf{k},\mathbf{k}'\right)=\frac{2\pi}{\hbar}|H_{\mathbf{k},\mathbf{k}'}|^2\delta\left(E_f-E_i\mp\hbar\omega\right)\delta_{\mathbf{k}'-\mathbf{k}\mp\mathbf{q},\mathbf{0}} \tag{3.2.1}$$

where $S\left(\mathbf{k},\mathbf{k}'\right)$ is the transition rate and $|H_{\mathbf{k},\mathbf{k}'}|^2$ is known as the "matrix element" [22, 28], and is defined for a system with an initial energy of E_i and final energy of E_f (including all interacting particles). The Dirac Delta function ensures that the expression complies with the principle of conservation of energy, whilst the Kronecker delta imposes the principle of conservation of momentum. The matrix element is dependent on the type of scattering, which means that Fermi's Golden Rule will produce different transition rates for the different scattering mechanisms. Fermi's Golden Rule can then be used in order to obtain an overall scattering rate, by integrating over all possible potential final states, **k'** that an electron can transition to from a set initial state, $\mathbf{k}$. The overall scattering rate for any particular scattering mechanism in the three-dimensional system is then given by,

$$W\left(\mathbf{k}\right)=\frac{\Omega}{(2\pi)^3}\frac{2\pi}{\hbar}\int|H_{\mathbf{k},\mathbf{k}'}|^2\delta\left(E_f-E_i\right)\delta_{\mathbf{k}'-\mathbf{k}\mp\mathbf{q},\mathbf{0}}d\mathbf{k}' \tag{3.2.2}$$

where the integration performed occurs over all possible final states that can

occur within the crystal with volume Ω. It is this expression which we use to derive the various scattering rates using the cosine band-structure approximation.

3.2.1. Polar Optical Phonon Scattering

Polar Optical Phonon (POP) scattering is the dominant form of electron scattering in polar materials at room temperatures. Whilst the polar optical phonon scattering rate has previously been derived by *Dyson* and *Ridley* [3], the derivation of this rate has previously not been published, and hence, it is a worthwhile exercise to re-derive the rate.

It has been shown that the matrix element for POP scattering is given by equation (3.2.3), where e is the electronic charge, ω_o is the polar optical phonon frequency, $\mathbf{q}$ is the phonon wave vector, q_0 is the electron screening, $n(\omega_o)$ is the phonon occupation number and $\frac{1}{\epsilon_p} = \frac{1}{\epsilon_\infty} - \frac{1}{\epsilon_s}$ (where ϵ_s and ϵ_∞ are the static and high frequency dielectric coefficients, respectively).

$$|H_{k,k'}|^2 = \frac{\hbar e^2 \omega_o q^2}{2\epsilon_p \Omega \left(q^2 + q_0^2\right)^2} \left(n(\omega_o) + \frac{1}{2} \pm \frac{1}{2}\right). \tag{3.2.3}$$

Substituting this into (3.2.2) and neglecting any potential electron screening, we obtain the scattering rate before integration, which is identical to that given by *Ridley* [22],

$$\begin{aligned} W(\mathbf{k}) &= \frac{e^2 \omega_0}{\epsilon_p 8\pi^2} \left(n\left(\omega_o\right) + \frac{1}{2} \pm \frac{1}{2}\right) \int_0^{2\pi} \int_{-1}^{1} \int_0^{q_{\mathrm{zb}}} \frac{q^2}{q^4} \\ &\times \delta\left(E_{k'} - E_k \mp \hbar\omega_o\right) \delta_{\mathbf{k}'-\mathbf{k}\mp\mathbf{q},\mathbf{0}} q^2 dq d(\cos\theta) d\phi. \end{aligned} \tag{3.2.4}$$

We can convert eqn. (3.2.4) to be an integration over $\mathbf{k}'$ instead, as the relation-

ship between $\mathbf{k}'$ and $\mathbf{q}$ is unique, obtaining,

$$\begin{aligned} W(\mathbf{k}) &= \frac{e^2\omega_0}{\epsilon_p 8\pi^2}\left(n\left(\omega_o\right)+\frac{1}{2}\pm\frac{1}{2}\right)\int_0^{2\pi}\int_{-1}^{1}\int_0^{\infty}\frac{k'^2}{q^2} \\ &\times \delta\left(E_{k'}-E_k\mp\hbar\omega_o\right)\delta_{\mathbf{k}'-\mathbf{k}\mp\mathbf{q},\mathbf{0}}dk'd(\cos\theta_k)d\phi. \end{aligned} \tag{3.2.5}$$

Using the principle of conservation of momentum (provided by the Kronecker delta), we have $q^2 = k^2 + k'^2 - 2kk'\cos\theta_k$. Substituting this into equation (3.2.5),

$$\begin{aligned} W(\mathbf{k}) &= \frac{e^2\omega_0}{\epsilon_p 8\pi^2}\left(n\left(\omega_o\right)+\frac{1}{2}\pm\frac{1}{2}\right)\int_0^{2\pi}\int_{-1}^{1}\int_0^{\infty}\frac{k'^2}{k^2+k'^2-2kk'\cos\theta_k} \\ &\times \delta\left(E_{\mathbf{k}'}-E_{\mathbf{k}}\mp\hbar\omega_o\right)dk'd(\cos\theta_k)d\phi. \end{aligned} \tag{3.2.6}$$

To simplify the integration further, the integral over k', can be converted to one over energy, $E_{\mathbf{k}}$. Using equation (3.1.3),

$$\begin{aligned} W(\mathbf{k}) &= \frac{e^2\omega_0}{\epsilon_p 8\pi^2}\left(n\left(\omega_o\right)+\frac{1}{2}\pm\frac{1}{2}\right)\int_0^{2\pi}\int_{-1}^{1}\int_0^{\infty}\frac{k'^2}{k^2+k'^2-2kk'\cos\theta_k} \\ &\times \frac{\delta\left(E_{\mathbf{k}'}-E_{\mathbf{k}}\mp\hbar\omega_o\right)}{E_B a\sqrt{\left(E_{\mathbf{k}}/E_B\right)-\left(E_{\mathbf{k}}/E_B\right)^2}}dE_{\mathbf{k}'}d(\cos\theta_k)d\phi. \end{aligned} \tag{3.2.7}$$

Integration over the azimuthal angle just introduces a factor of 2π. Following this with an integration over $\cos\theta_k$ produces,

$$\begin{aligned} W(\mathbf{k}) &= \frac{e^2\omega_0}{\epsilon_p 8\pi}\left(n\left(\omega_o\right)+\frac{1}{2}\pm\frac{1}{2}\right)\frac{k'}{k}\ln\left(\frac{(k'+k)^2}{(k'-k)^2}\right) \\ &\times \int_0^{\infty}\frac{\delta\left(E_{\mathbf{k}'}-E_{\mathbf{k}}\mp\hbar\omega_o\right)}{E_B a\sqrt{\left(E_{\mathbf{k}}/E_B\right)-\left(E_{\mathbf{k}}/E_B\right)^2}}dE_{\mathbf{k}'}. \end{aligned} \tag{3.2.8}$$

Finally, the integration of the delta function with respect to energy restricts $E_{k'}$ to be equal to $E_k \pm \hbar\omega_o$, with values of k' similarly restricted. This yields the POP scattering rate in a spherical cosine band, equivalent to that given by *Dyson* and

Ridley [3],

$$W(\mathbf{k}) = \frac{e^2\omega_0}{E_B a \epsilon_p 8\pi}\left(n\left(\omega_o\right) + \frac{1}{2} \pm \frac{1}{2}\right)\frac{k'}{k}\frac{1}{\sqrt{\left(E_\mathbf{k}/E_B\right) - \left(E_\mathbf{k}/E_B\right)^2}}\ln\left[\frac{(k'+k)^2}{(k'-k)^2}\right]. \tag{3.2.9}$$

3.2.2. Non-Polar Optical Phonon Scattering

Non-Polar Optical Phonon (NPOP) scattering, also called Optical Deformation Potential (ODP) scattering in some literature, has no part in intra-valley scattering in GaN, due to it's polar nature. However, NPOP scattering is the primary scattering mechanism for inter-valley scattering for scattering between non-equivalent valleys (e.g. from the Γ to one of the M-L valleys) and equivalent valleys (e.g. between the six M-L valleys) in materials such as GaN. For the purposes of GaN, however, only scattering into the Γ valley from satellite valleys need be considered using the cosine-band structure approximation, as the approximation is only used for the Γ valley. The scattering rate for NPOP scattering to, or between, the satellite valleys is determined by the shape of the valley that the electron is transferring to, in our case, the parabolic approximation. However, this derivation is very similar to that which would be required for equivalent valley scattering, should this approximation be used for satellite valleys in other models.

The matrix element for NPOP scattering is, [14, 22]

$$|H_{k,k'}|^2 = \frac{D_o^2\hbar}{2\Omega\rho\omega_o}\left(n(\omega_o) + \frac{1}{2} \pm \frac{1}{2}\right) \tag{3.2.10}$$

where D_o is the optical deformation potential constant and ρ is the material density. By substituting (3.2.10) into Fermi's Golden Rule, (3.2.2), we obtain the scattering

rate integral,

$$W(\mathbf{k}) = \frac{1}{(2\pi)^3}\frac{\pi {D_o}^2}{\rho\omega_o}\left(n\left(\omega_o\right) + \frac{1}{2} \mp \frac{1}{2}\right)\int \delta\left(E_{\mathbf{k}'} - E_{\mathbf{k}} \mp \hbar\omega_o\right) d\mathbf{k}'. \tag{3.2.11}$$

Assuming that the effect of the frequency dependence in the Dirac delta function is negligible when compared with the rest of the expression, we can convert this equation to an integration over energy by using the relation:

$$\frac{1}{2\pi^3}\int \delta\left(E' - E\right) d\mathbf{k}' = \int \delta\left(E_{\mathbf{k}'} - E_{\mathbf{k}} \pm c\right) N(E_{\mathbf{k}'}) dE_{\mathbf{k}'} \tag{3.2.12}$$

where c is some constant with no dependence on $dE_{\mathbf{k}'}$. Equation (3.2.11) therefore becomes:

$$W(\mathbf{k}) = \frac{\pi {D_o}^2}{\rho\omega_o}\left(n\left(\omega_o\right) + \frac{1}{2} \mp \frac{1}{2}\right)\int_0^\infty \delta\left(E_{\mathbf{k}'} - E_{\mathbf{k}} \mp \hbar\omega_o\right) N\left(E_{\mathbf{k}'}\right) dE_{\mathbf{k}'}. \tag{3.2.13}$$

Through the use of the properties of the Dirac delta function, integrating this equation produces the scattering rate for NPOP scattering, which is identical to that of the NPOP scattering rates of other scattering rates except for the density of states term, which is band-structure dependent.

$$W(k) = \frac{\pi {D_o}^2}{\rho\omega_o}\left(n\left(\omega_o\right) + \frac{1}{2} \mp \frac{1}{2}\right) N\left(E_{\mathbf{k}} \mp \hbar\omega_o\right). \tag{3.2.14}$$

Substituting in (3.1.4), we get,

$$W(\mathbf{k}) = \frac{\pi {D_o}^2}{\rho\omega_o}\left(n\left(\omega_o\right) + \frac{1}{2} \mp \frac{1}{2}\right)\frac{\left[\cos^{-1}\left(1 - 2(E \mp \hbar\omega_o)/E_B\right)\right]^2}{E_B a^3\pi^2\sqrt{\left((E \mp \hbar\omega_o)/E_B\right) - \left((E \mp \hbar\omega_o)/E_B\right)^2}}. \tag{3.2.15}$$

3.2.3. Piezoelectric Phonon Scattering

Piezoelectric (PZ) phonon scattering can be thought of as the acoustic mode equivalent of POP scattering. Unlike POP scattering, however, PZ scattering is less dominant at room temperature. However, at low energies and temperatures, the effects of PZ scattering cannot be neglected.

The matrix element for PZ scattering is [14, 22]

$$|H_{\mathbf{k},\mathbf{k}'}|^2 = \frac{e^2 K_{av}^2 k_B T q^2 \pi}{8\epsilon_p \hbar\Omega \left(q^2 + q_0^2\right)^2}. \tag{3.2.16}$$

where

$$K_{av}^2 = \begin{cases} \frac{e_{14}^2}{\epsilon_p}\left(\frac{12}{35c_L} + \frac{16}{35c_T}\right) & \text{for zinc blende structures} \\ \frac{1}{\epsilon_p}\left(\frac{e_L^2}{c_L} + \frac{e_T^2}{c_T}\right) & \text{for wurzite structures} \end{cases}. \tag{3.2.17}$$

c_L and c_T are the longitudinal and transverse spherical elastic constants and e_{14} is a piezoelectric constant determined by the piezoelectric tensor for zinc blende structres. e_L and e_T are defined as

$$e_L^2 = \frac{e_{33}^2}{7} + \frac{4e_{33}\left(e_{31} + 2e_{15}\right)}{35} + \frac{8\left(e_{31} + 2e_{15}\right)^2}{105}; \tag{3.2.18}$$

$$e_T^2 = \frac{16e_{15}^2}{35} + \frac{16e_{15}\left(e_{33} - e_{31} - e_{15}\right)}{105} + \frac{2\left(e_{33} - e_{31} - e_{15}\right)^2}{35}. \tag{3.2.19}$$

where e_{15}, e_{31} and e_{33} are the various wurzite structure piezoelectric constants. [22] The scattering rate integral, by substitution into (3.2.2), is therefore,

$$W(\mathbf{k}) = \frac{q^2 K_{av}^2 k_B T}{8\pi^2 \epsilon \hbar} \int \frac{q^2}{\left(q^2 + q_0^2\right)^2} \delta_{\mathbf{k}\pm\mathbf{q}-\mathbf{k}',0}\, \delta\left(E_{\mathbf{k}'} - E_{\mathbf{k}} \mp \hbar\omega_{\mathbf{q}}\right) d\mathbf{k}'. \tag{3.2.20}$$

Converting (3.2.20) to an integral over q,

$$\begin{aligned} W(\mathbf{k}) &= \frac{e^2 K_{av}^2 k_B T}{8\pi^2 \epsilon \hbar} \int_0^{2\pi} \int_{-1}^{1} \int_0^{2k} \frac{q^4}{\left(q^2 + q_0^2\right)^2} \delta_{\mathbf{k}\pm\mathbf{q}-\mathbf{k}',0} \\ &\times \delta\left(E_{\mathbf{k}'} - E_{\mathbf{k}} \mp \hbar\omega_{\mathbf{q}}\right) dq\, d\left(\cos\left(\theta\right)\right) d\phi. \end{aligned} \tag{3.2.21}$$

The integration over the azimuthal angle ϕ simply introduces a factor of 2π into the rate, yielding

$$W(\mathbf{k}) = \frac{e^2 K_{av}^2 k_B T}{4\pi \epsilon \hbar} \int_{-1}^{1} \int_0^{2k} \frac{q^4}{\left(q^2 + q_0^2\right)^2} \delta_{\mathbf{k}\pm\mathbf{q}-\mathbf{k}',0} \delta\left(E_{\mathbf{k}'} - E_{\mathbf{k}} \mp \hbar\omega_{\mathbf{q}}\right) dq\, d\left(\cos\left(\theta\right)\right). \tag{3.2.22}$$

In order to integrate over $\cos(\theta)$, we must make an approximation known as the "long wave" approximation. In the long wave approximation, we note that, for acoustic waves, $k_{max} \approx 1\% \frac{\pi}{a}$, that is, the maximum k-vector is approximately 1% of the Broullion zone of the crystal when PZ scattering is occurring. Therefore, we assume that $k_{max} a \approx 0.01\pi$. Using this, we can safely use the Taylor expansion for a cosine, as we now know $k_{max} a$, the maximum value we assume ka can be, to be small. This yields,

$$\cos\left(ka\right) \approx 1 - \frac{k^2 a^2}{2} + \frac{k^4 a^4}{24} + O\left(k^6\right) \tag{3.2.23}$$

Substituting (3.2.23) into (3.2.22) yields,

$$\begin{aligned} W(\mathbf{k}) &= \frac{e^2 K_{av}^2 k_B T}{4\pi \epsilon \hbar} \int_{-1}^{1} \int_0^{2k} \frac{q^4}{\left(q^2 + q_0^2\right)^2} \delta_{\mathbf{k}\pm\mathbf{q}-\mathbf{k}',0} \\ &\times \delta\left(\frac{E_B}{2}\cos\left(ka\right) - \frac{E_B}{2}\left[\left(1 - \frac{\left(k'a\right)^2}{2} + \frac{\left(k'a\right)^4}{24}\right)\right] \mp \hbar\omega_{\mathbf{q}}\right) dq\, d\left(\cos\left(\theta\right)\right). \end{aligned} \tag{3.2.24}$$

It is important to note that $\cos(ka)$ in (3.2.24) is regarded as a constant, as no integration over k is performed, therefore, the substitution in (3.2.23) is only performed on $\cos(k'a)$. Applying the conservation of momentum from the Kronecker delta to (3.2.24),

$$\begin{aligned} W(\mathbf{k}) &= \frac{e^2 K_{av}^2 k_B T}{4\pi\epsilon\hbar} \int_{-1}^{1}\int_{0}^{2k} \frac{q^4}{\left(q^2+q_0^2\right)^2} \delta\left\{\frac{E_B}{2}\cos(ka)\right. \\ &\times -\frac{E_B}{2}\left[\left(1-\frac{a^2\left(k^2+q^2-2kq\cos(\theta)\right)}{2}+\frac{a^4\left(k^2+q^2-2kq\cos(\theta)\right)^2}{24}\right)\right] \\ &\times \mp\hbar\omega_{\mathbf{q}} dq\, d(\cos(\theta)). \end{aligned} \tag{3.2.25}$$

Equation (3.2.25) is now in an state in which we can integrate the Dirac delta over $\cos(\theta)$ using the identity

$$\int f(x)\,\delta(g(x))\,dx = \sum_{i=1}^{n} \frac{f(x_n)}{g'(x_n)} \tag{3.2.26}$$

Before differentiation, however, we neglect the term $(kqa^2)^2\cos(\theta)$ that arises from the expansion of $a^4\left(k^2+q^2-2kq\cos(\theta)\right)^2$, as $(k_{max}a^2)^2 \approx 10^{-4}\pi^2$, which is much less than 1. Differentiating (3.2.25) with this term neglected with respect to $\cos(\theta)$ using (3.2.26), we obtain

$$W(\mathbf{k}) = \frac{e^2 K_{av}^2 k_B T}{4\pi\epsilon\hbar} \int_{0}^{2k} \frac{q^4}{\left(q^2+q_0^2\right)^2} \frac{1}{(E_B/2)\left[kqa^2+(a^4/6)\left(k^3q+q^3k\right)\right]} dq. \tag{3.2.27}$$

The summation sign has been dropped, as all the $\cos_n(\theta)$ terms have been cancelled out, meaning that there is only one term to sum. (3.2.27) can be further simplified to give,

$$W(\mathbf{k}) = \frac{e^2 K_{av}^2 k_B T}{2\pi\epsilon\hbar E_B k a^2} \int_{0}^{2k} \frac{q^3}{\left(q^2+q_0^2\right)^2\left[1+(a^2/6)\left(k^2+q^2\right)\right]} dq. \tag{3.2.28}$$

Integrating (3.2.28) with respect to q and inserting the limits yields the scattering rate,

$$W(\mathbf{k}) = \frac{3e^2 K_{av}^2 k_B T}{2\pi\epsilon\hbar E_B k a^2} \frac{\chi_2\chi_1 \ln\left[\left(\chi_1\chi_2\right) / \left({q_0}^2\left(6+5a^2k^2\right)\right)\right] - 4k^2\chi_3}{{\chi_1\chi_3}^2}, \tag{3.2.29}$$

where $\chi_1 = 4k^2 + {q_0}^2$, $\chi_2 = 6 + a^2k^2$ and $\chi_3 = 6 + a^2\left(k^2 - {q_0}^2\right)$.

3.2.4. Acoustic Phonon Scattering

Acoustic Phonon, or Acoustic Deformation Potential (ADP) scattering, is the acoustic mode equivalent of NPOP scattering, but unlike NPOP scattering, ADP scattering is present within the Γ valley and plays no part in inter-valley scattering of electrons. Like PZ scattering, ADP is only a dominant scattering mechanism at low energies and temperatures, but it is for these very reasons again that they must not be neglected.

The ADP matrix element is, [14, 22]

$$\left|H_{\mathbf{k},\mathbf{k}'}\right|^2 = \frac{{\Xi_d}^2 k_B T}{2\rho{\bar{\nu}_{sL}}^2} \tag{3.2.30}$$

where Ξ_d is the acoustic deformation potential constant, $\bar{\nu}_{sL}$ is the longitudinal acoustic velocity. Substituting this into (3.2.2), we obtain, [25],

$$W(\mathbf{k}) = \frac{1}{(2\pi)^3} \frac{\pi{\Xi_d}^2 k_B T}{\hbar\rho{\bar{\nu}_{sL}}^2} \int \delta\left(E_{\mathbf{k}'} - E_{\mathbf{k}} \mp \hbar\omega_{\mathbf{q}}\right) d\mathbf{k}'. \tag{3.2.31}$$

As with the NPOP scattering, we can convert the equation to be integrated over energy as long as we neglect the angular dependence on the delta function and consider acoustic phonon scattering as an elastic process as $\hbar\omega_{\mathbf{q}} \ll kT$ at

most temperatures.[22] (As there is no $\mathbf{k}'$ dependence outside of the delta function, unlike in the derivation of PZ scattering, it is advantageous to do this, see Ridley [22].) Thus, we obtain

$$W(\mathbf{k}) = \int \frac{\pi \Xi_d{}^2 k_B T}{\hbar \rho \bar{\nu}_{sL}{}^2} N\left(E_{\mathbf{k}'}\right) \delta\left(E_{\mathbf{k}'} - E_{\mathbf{k}}\right) dE_{\mathbf{k}'}. \tag{3.2.32}$$

Integrating this, we can easily obtain the ADP scattering rate though the integration of the Dirac delta function:

$$W(\mathbf{k}) = \frac{\pi \Xi_d{}^2 k_B T}{\hbar \rho \bar{\nu}_{sL}{}^2} N\left(E_{\mathbf{k}}\right). \tag{3.2.33}$$

which, as with the NPOP scattering, is an identical expression to that of other band structures. Substituting in the density of states for the cosine band structure approximation, and Equation (3.2.33) becomes:

$$W(\mathbf{k}) = \frac{\pi \Xi_d{}^2 k_B T}{\hbar \rho \bar{\nu}_{sL}^2} \frac{\left[\cos^{-1}\left(1 - 2E/E_B\right)\right]^2}{E_B a^3 \pi^2 \sqrt{\left(E/E_B\right)^2 - \left(E/E_B\right)}}. \tag{3.2.34}$$

3.2.5. Charged Impurity Scattering

Imperfections often occur through the growth of semiconductor crystals. One type of imperfection that can occur is the inclusion of foreign molecules to the crystal, usually artificially included in the material in order to alter the transport properties of the material (often referred to as doping a material).

Using the Brooks-Herring approach, Ridley suggests that the matrix element is

[22],

$$|H_{\mathbf{k},\mathbf{k}'}|^2 = \frac{Z^2 e^4}{\epsilon_s^2 \Omega^2} \frac{1}{\left(|\mathbf{k}' - \mathbf{k}|^2 + q_0^2\right)^2}. \tag{3.2.35}$$

where Ze is the charge on an impurity atom, and $q_0 \equiv q_D$, the Debye length. Through the use of the delta function and the principle of conservation of energy, we can assume that $|\mathbf{k}'| = |\mathbf{k}|$. Therefore, it can be shown that, if the angle between $\mathbf{k}$ and $\mathbf{k}'$ is θ, using trigonometric identities, we find,

$$\mathbf{k}' - \mathbf{k} = 2k^2 \left(1 - \cos\theta\right). \tag{3.2.36}$$

Substituting (3.2.35) and (3.2.36) into (3.2.2), and multiplying by $N_I \Omega$, the number of impurities in the normalization volume,

$$W\left(\mathbf{k}\right) = \frac{1}{8\pi^3} \int \frac{2\pi}{\hbar} \frac{N_I Z^2 e^4}{\epsilon_s^2} \frac{1}{\left(k^2\left(1 - \cos\theta\right) + q_0^2\right)^2} \delta\left(E_{\mathbf{k}'} - E_{\mathbf{k}}\right) d\mathbf{k}'. \tag{3.2.37}$$

Substituting out $d\mathbf{k}'$ for $k'^2 dk' d\cos\theta d\phi$, we obtain

$$W\left(\mathbf{k}\right) = \frac{1}{8\pi^3} \int_0^{2\pi} \int_{-1}^{1} \int_{-\infty}^{\infty} \frac{2\pi}{\hbar} \frac{N_I Z^2 e^4}{\epsilon_s^2} \frac{1}{\left(2k^2\left(1 - \cos\theta\right) + q_0^2\right)^2} \delta\left(E_{\mathbf{k}'} - E_{\mathbf{k}}\right) k'^2 dk' d\cos\theta d\phi. \tag{3.2.38}$$

We can further replace $k'^2 dk'/8\pi^3$ by $(N(E_{\mathbf{k}'})/4\pi) dE_{\mathbf{k}'}$, allowing for the easy integration of (3.2.38). Integrating with respect to the azimuthal angle ϕ and energy,

$$W\left(\mathbf{k}\right) = \int_{-1}^{1} \frac{4\pi^2}{\hbar} \frac{N_I Z^2 e^4}{\epsilon_s^2} \frac{1}{\left(2k^2\left(1 - \cos\theta\right) + q_0^2\right)^2} \frac{N(E_{\mathbf{k}})}{4\pi} d\cos\theta. \tag{3.2.39}$$

Finally, by integrating (3.2.39) we obtain the scattering rate for charged-impurity scattering,

$$W(\mathbf{k}) = \frac{2\pi N_I Z^2 e^4}{\hbar \epsilon_s^2 \left(q_0^2 \left(4k^2 + q_0^2\right)\right)} N\left(E_{\mathbf{k}}\right). \tag{3.2.40}$$

As with the NPOP scattering rate, the expression is identical to that derived for parabolic band-structures, except for the density of states, which takes the required form (in this case, the cosine form).

3.2.6. Threaded Dislocation Scattering

Due to the lack of lattice-matched substrates for the epitaxial growth of GaN crystals, lattice dislocations occur throughout the material. These can play a significant role in the characteristics of the material if there is a sufficient concentration of them - it is therefore important to ensure they are not neglected. It is also important to note that electrons that are traveling parallel to the thread dislocations will not be scattered by them, and therefore only the component of the **k**-vector perpendicular to the dislocation is taken into account. Dislocation scattering is therefore a two-dimensional rate, and it is assumed that the dislocations are perpendicular to the applied electronic field.

Look and *Sizelove* suggested that the transition rate for dislocation scattering is (with the momentum relaxation rate factor of $(1 - \cos\theta)$ removed)[73],

$$W(\mathbf{k}) = \frac{1}{(2\pi)^2} \frac{2\pi}{\hbar} \int \left|H_{\mathbf{k},\mathbf{k}'}\right|^2 \delta\left(E_{\mathbf{k}_\perp} - E_{\mathbf{k}'_\perp}\right) d\mathbf{k}'_\perp. \tag{3.2.41}$$

It has been shown that, to an excellent approximation that the matrix element

is [73],

$$|H_{\mathbf{k},\mathbf{k}'}|^2 = \frac{e^2\lambda^2}{\epsilon a\left(1+q^2\lambda^2\right)} \tag{3.2.42}$$

where,

$$\lambda = \left(\frac{\epsilon k_B T}{e^2 n'}\right)^{1/2} \tag{3.2.43}$$

and n' is the effective screening concentration. Substituting (3.2.42) into (3.2.41)

$$W(\mathbf{k}) = \frac{1}{(2\pi)^2}\frac{2\pi}{\hbar}\int\left(\frac{e^2\lambda^2}{\epsilon a\left(1+q^2\lambda^2\right)}\right)^2 \delta\left(E_{\mathbf{k}_\perp} - E_{\mathbf{k}'_\perp}\right) d\mathbf{k}'_\perp. \tag{3.2.44}$$

Converting this into an integration over energy by making substitutions like so,

$$d\mathbf{k}'_\perp = k'_\perp dk'_\perp d\theta = \left(\frac{\cos^{-1}\left(1-2E_{\mathbf{k}'_\perp}/E_B\right)}{E_B a\pi\sqrt{\left(E_{\mathbf{k}'_\perp}/E_B\right)^2 - \left(E_{\mathbf{k}'_\perp}/E_B\right)}}\right) d\theta dE_{\mathbf{k}_\perp}. \tag{3.2.45}$$

Putting (3.2.45) into (3.2.44), we obtain,

$$\begin{aligned} W(\mathbf{k}) &= \frac{1}{2\pi\hbar}\int_0^{2\pi}\int_0^{\infty}\left(\frac{e^2\lambda^2}{\epsilon a\left(1+q^2\lambda^2\right)}\right)^2 \\ &\times \frac{\cos^{-1}\left(1-2E_{\mathbf{k}'_\perp}/E_B\right)}{E_B a^2\sqrt{\left(E_{\mathbf{k}'_\perp}/E_B\right)^2 - \left(E_{\mathbf{k}'_\perp}/E_B\right)}}\delta\left(E_{\mathbf{k}_\perp} - E_{\mathbf{k}'_\perp}\right) d\theta dE_{\mathbf{k}_\perp}. \end{aligned} \tag{3.2.46}$$

Integrating this, we get,

$$W(\mathbf{k}) = \frac{1}{\hbar}\left(\frac{e^2\lambda^2}{\epsilon a\left(1+q^2\lambda^2\right)}\right)^2 \frac{\cos^{-1}\left(1-2E_{\mathbf{k}_\perp}/E_B\right)}{E_B a^2\sqrt{\left(E_{\mathbf{k}_\perp}/E_B\right)^2 - \left(E_{\mathbf{k}_\perp}/E_B\right)}}. \tag{3.2.47}$$

Finally, we must multiply this by the areal density of dislocations, N_{dis}, as the

rate derived is for one dislocation per unit area. Hence, our final rate for dislocation scattering is,

$$W(\mathbf{k}) = \frac{N_{dis}}{\hbar}\left(\frac{e^2\lambda^2}{\epsilon a\left(1+q^2\lambda^2\right)}\right)^2 \frac{\cos^{-1}\left(1-2E_{\mathbf{k}_\perp}/E_B\right)}{E_B a^2\sqrt{\left(E_{\mathbf{k}_\perp}/E_B\right)^2-\left(E_{\mathbf{k}_\perp}/E_B\right)}}. \tag{3.2.48}$$

3.3. Summary

In this chapter, an overview of the cosine band-structure approximation and its various characteristics have been described. The basic form of the approximation has been compared with that of other approximations, particularly the **k.p** approximation, the two approximations are similar at low energies but begin to diverge significantly at energies above 0.5 eV. We have also explained the effect of the inflection point in the approximation, giving rise to the negative effective mass effect, which is thought to be crucial in some III-V nitride materials, in particular, Gallium Nitride. By using this new cosine band-structure approximation, we can try to gain insight into how much of an effect negative mass states has the electron transport characteristics of these materials.

In order to include this band-structure approximation in our simulations, we have derived scattering rates specifically for this approximation. Figure 3.5 shows all derived rates as a function of energy, compared with the rates for a parabolic band-structure, with the exception of dislocation scattering. We find, through comparison of these rates with those derived from other models, that the scattering rates deviate more at higher energies, thus, it is expected that the effect of the new band-structure approximation will be more apparent at higher energies.

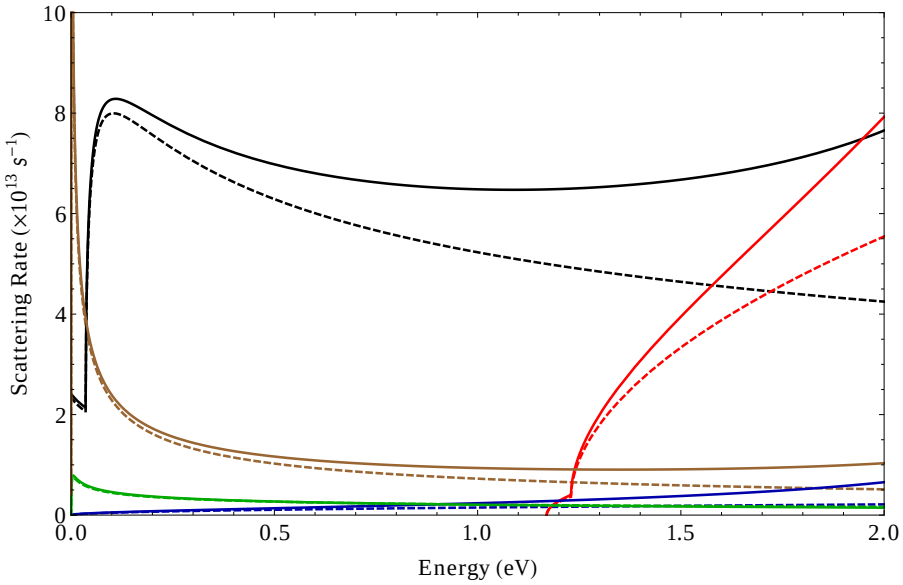

Figure 3.5) Comparison of scattering rates derived using the parabolic (dashed) and cosine (solid) band-structure approximations assuming GaN parameters at a temperature of 300 K. POP (black), NPOP inter-valley (assuming an inter-valley separation of 1.2 eV, red) ADP (blue), PZ (green) and Impurity (brown) scattering rates are included in the comparison. Dislocation scattering is not included as it is only a two-dimensional rate.

Chapter 4
Demonstration of Monte Carlo codes

The basic algorithms described in chapter 2 are given by *Tomizawa* [25]. They have been re-engineered to make use of the latest Fortran features and parallelisation techniques, as well as to make use of a new band-structure approximation (as described in chapter 3). However, in order to be able to use these codes with confidence, the codes are checked against the properties of materials with known characteristics. As two major sets of changes have been made to the codes, computational (use of new language features and parallelisation) and physical (use of a new band-structure approximation), separate tests for each sets of changes need to be performed, to ensure that the results are believable by checking our results against other theoretical and experimental works.

To this end, in this chapter we first demonstrate that the computational changes that were made to the algorithm produce expected and believable results, by generating results from materials that have well documented transport characteristics, namely Gallium Arsenide (GaAs) and Indium Phosphide (InP). Results from the code are compared with experimental results for velocity-field characteristics. A check of the model when a third valley is added to the algorithm is then performed by checking the output of the three valley Zinc Oxide (ZnO) model against recent theoretical works, as there is very little available experimental data. In both these cases, we use the well-established **k.p** model for the band-structure in order to perform these tests. The chapter concludes by arguing the case for the new cosine band-structure approximation, with details and results of tests which compare the results that the physical changes to the model (introduced by this new approximation) produce, with experimental data and other models, using sample Gallium

Nitride parameters.

4.1. Demonstration of computational changes

4.1.1. Materials

4.1.1.1. Gallium Arsenide

Gallium Arsenide (GaAs) is a well-understood direct band gap III-V semiconductor that has been intensively studied over the past decades [74, 75]. GaAs can be used in a variety of high frequency situations due to it's high electron mobility and the transferred electron (TE) effect (also known as the Gunn effect) due to the relatively small energy difference between the two lowest conduction band valleys ($\sim 0.3\,\mathrm{eV}$) [74]. These properties make GaAs an excellent candidate for fast field-effect transistors, with switching speeds of 30 GHz being reported [76], and has also been used in Gunn diodes in order to generate EM waves with frequencies around 100 GHz [77]. It also has optoelectronic uses, due to its direct band gap it can be used in lasers with relative efficiency when compared with indirect band gap materials (such as Silicon) [31]. However, a major drawback of GaAs when compared with GaN is that the field in which electrical breakdown occurs is relatively low, GaN has a breakdown field approximately an order of magnitude greater than that of GaAs at approximately $\sim 4 \times 10^5\,\mathrm{V/cm}$ [78, 79], restricting its use in high power situations. That said, GaAs is a cheap and relatively fast responding material that is used in a wide variety of low power applications. Due to it's well known characteristics, and abundance of experimental data, GaAs is an excellent and simple candidate to validate this algorithm with.

4.1.1.2. Indium Phosphide

Indium Phosphide (InP), like GaAs, is a direct band gap III-V semiconductor that has also been studied extensively [80]. Like GaAs, it has been touted as a material suited to high frequency electronics (again, due to the TE effect) and has even been the subject of some investigations into terahertz (THz) frequency electromagnetic wave generation [1], again, due to high electron mobilities and the transferred electron effect. As InP also has a direct band gap, it is suitable for efficient optoelectronic applications. Its main drawback, however, is its low breakdown field, whilst slightly higher than that of GaAs [2], limiting its usefulness in lower power situations. Nevertheless, with it's high electron mobility and the Gunn effect exhibited by the material, it is a good choice for low power high frequency applications. Its well known characteristics and parameters allows for InP to be used as an excellent material to validate the algorithm with.

4.1.1.3. Zinc Oxide

Zinc Oxide (ZnO) is a direct-band gap II-VI semiconductor that has gathered much recent interest [26, 81–84]. Unlike GaAs and InP, ZnO favours the wurzite molecular structure (though it can also form a zinc blende structure) [85], and, like GaN, it has a wide band gap and has been touted as a possible competitor to GaN in high-field electronics. As it is a transparent material, it has seen use in the creation of transparent electrodes, a recent example of this by Oh *et al.* [86] suggests the use of zinc oxide in the production of light-emitting LCD devices, replacing the more expensive and hazardous indium tin oxide layer. It has also gathered interest in the optoelectronic field, with a similar band gap to GaN, it shares some optical properties with it, with optical emission occurring at approximately $384nm$ [87],

comparable with that of GaN, which emits light at wavelengths of about 405 nm.

Less is known about ZnO than GaAs and InP, with a large variance in the reported material parameters, which gives rise to many different reported transport characteristics (which is particularly noticeable when looking at the different reported velocity-field characteristics of the material [81–84]). Thus, the validation of the algorithm presented in this thesis is limited to comparing results from other theoretical works using their parameters, there is very little reliable experimental data on ZnO with regards to electron velocity.

4.1.2. Results

The parameters that are used in this set of tests are summarized in table 4.1. We discuss the characteristics of GaAs and InP first, as their material properties and transport characteristics are well known and experimental data is easily accessible, and then move on to analysing ZnO and tests of a three-valley model.

Table 4.1) Parameters used in the tests for GaAs, InP and ZnO. For ZnO, parameters from Bertazzi *et al.* [82] take precedence over other sources.
*Calculated from the C_{44} elastic constant, 44.3GPa. [88]

Parameter (units)	GaAs [31, 74, 89]	InP[80]	ZnO [81, 82, 88, 90]
Crystal Structure	Zinc Blende	Zinc Blende	Wurzite
Density (kg/m^3)	5360	4810	5606
Longitudinal sound velocity (ms^{-1})	5240	5130	6590
Transverse sound velocity, (ms^{-1})	2480	2160	2810*
Non-polar optical deformation potential coupling constant, (eV/m)	10^{11}	6.7×10^{10}	10^{11}
Inter-valley scattering coupling constant, (eV/m)	10^{11}	2.5×10^{11}	10^{11}
Acoustic deformation potential, (eV)	7	8	3.83
Piezoelectric constant e_{14} (C m^{-2})	−0.16	−0.035	–
Piezoelectric constant e_{15} (C m^{-2})	–	–	−0.37
Piezoelectric constant e_{31} (C m^{-2})	–	–	−0.62
Piezoelectric constant e_{33} (C m^{-2})	–	–	0.96
Energy gap (eV)	1.424	1.34	3.4
Static dielectric constant (ϵ_0)	12.9	12.5	8.2
High-frequency dielectric constant (ϵ_0)	10.92	9.61	3.7
Energy gap (between Γ_1 and Γ_3 valley minima) (eV)	–	–	4.4
Energy gap (between Γ_1 and satellite valley minima) (eV)	0.29	0.59	4.6
Number of equivalent satellite upper valleys	4	4	6
Effective mass, Γ_1 minima (m_e)	0.067	0.078	0.22
Effective mass, Γ_3 minima (m_e)	–	–	0.42
Effective mass, satellite upper valley minima (m_e)	0.35	0.26	0.7
Polar optical phonon energy (meV)	35.36	42.82	72
Non-polar optical phonon energy (equivalent valleys) (meV)	27.8	29	50
Non-polar optical phonon energy (inter-valley) (meV)	34.3	27.8	50
Charged carrier concentration (cm^{-3})	10^{14}	10^{15}	10^{14}

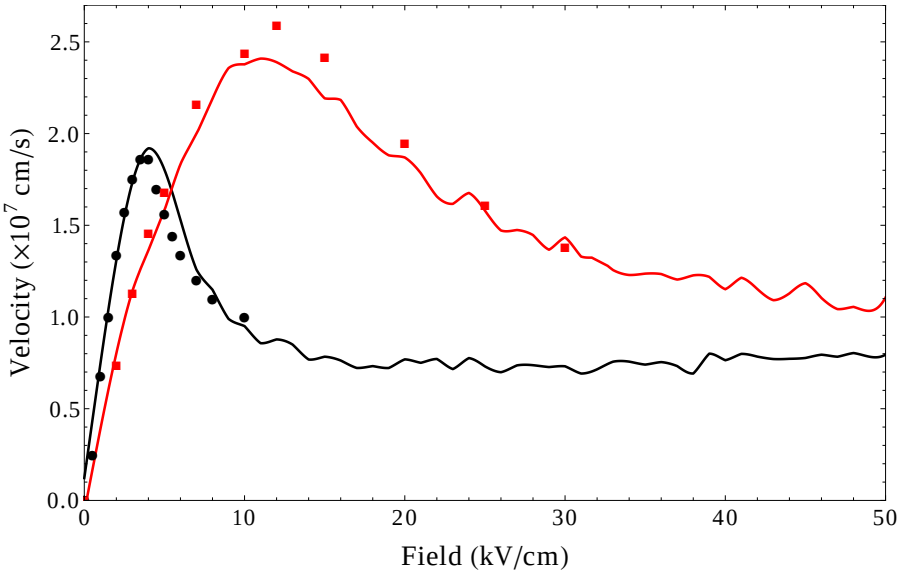

Figure 4.1) Velocity-field data for GaAs and InP. Lines are from Monte-Carlo code using the EMC algorithm and the **k.p** band structure, points are experimentally obtained data points. Black: GaAs, red: InP. (GaAs experimental data from Blakemore [74], InP experimental data from Maloney and Frey [80].)

4.1.2.1. Gallium Arsenide & Indium Phosphide

The steady-state velocity-field characteristics that have been generated for GaAs and InP, along with experimental data, are shown in figure 4.1. It can be seen that there is a close correlation between the theory and experimental results in both cases, particularly in the case of GaAs. The discrepancy in the data can be accounted for by noting that the codes do not account for all scattering mechanisms that are known to happen in the materials, which would most likely cause an overestimation in the velocity as there would be an absence of momentum relaxing events, and that the concentration of charged impurities in the experimental data was not specified, where the expectation is that larger impurity concentrations would cause a decrease the magnitude of the velocity saturation, and potentially decreasing the critical field slightly, with the opposite effect occurring with a smaller concentration of impurities.

We also look at the energy-field and the Γ_1 valley occupancy characteristics in

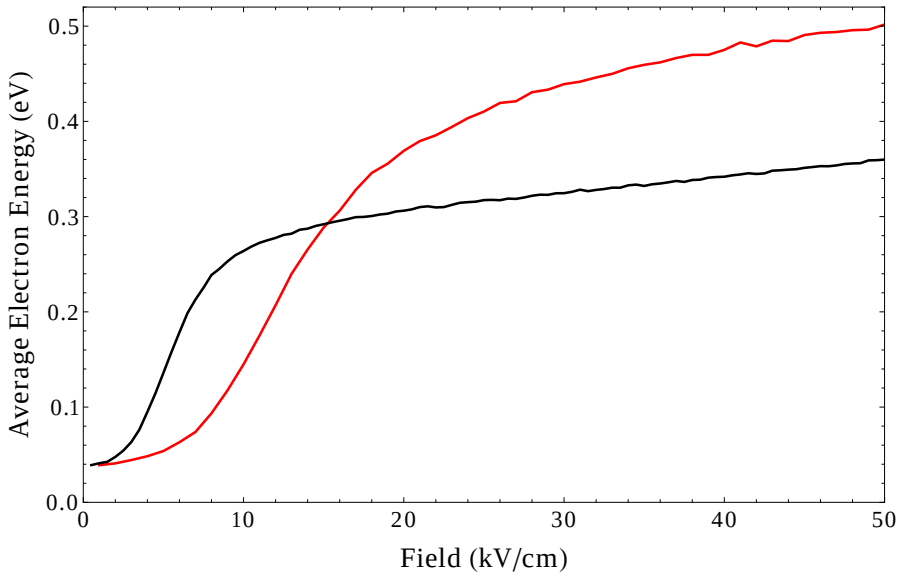

Figure 4.2) Energy-field characteristics for GaAs (black) and InP (red) using the EMC algorithm and the **k.p** band structure. Average energy is relative to the minima of the Γ_1 valley (i.e. the bottom of the conduction band)

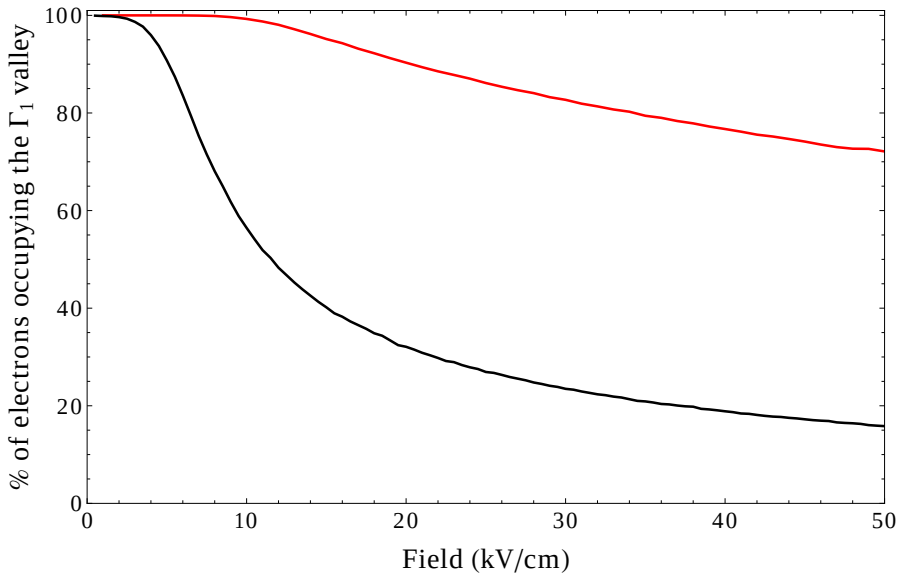

Figure 4.3) Steady state occupancy of the Γ_1 valley as a function of the applied field for GaAs (black) and InP (red) using the EMC algorithm and the **k.p** band structure.

figures 4.2 & 4.3, and find that they are consistent with the velocity-field characteristics from the models. From the energy-field characteristics, it can be seen that the sharp increase in steady-state average electron energy (with respect to the field), at slightly lower fields than the critical field - a characteristic that is consistent with the occupancy characteristic, with electron transfer to the satellite valleys beginning to occur at a similar field. The occupancy-field characteristics also fit well with the velocity-field characteristics, with the transferred electron effect beginning before the critical field and the saturation velocity is reached. Based on the combination of these characteristics, we can make a reasonable assumption that the algorithm performs as expected and can therefore be relied upon for two-valley **k.p** approximation based models.

4.1.2.2. Zinc Oxide

In this set of tests, both a two valley and a three valley model are used. The two valley model uses the lowest conduction band valley at the Γ point (Γ_1) valley and the six satellite valleys located between the L and M points in the Brillouin zone. The three valley model includes the next highest valley at the Γ point, the Γ_3 valley.

Figure 4.4 compares the velocity-field characteristics of these two models, and it can be seen that the resulting characteristics between the two models are almost identical. This is not surprising, as the the Γ_3 valley, which only features in the three valley simulations, has a similar energy minima to that of the satellite L-M valleys. Also, as the valley is narrower than the L-M valleys (as referenced by the lower effective mass), larger energies can be attained more quickly and, as such, electrons can be promoted into the satellite valleys from the Γ_3 valley quickly.

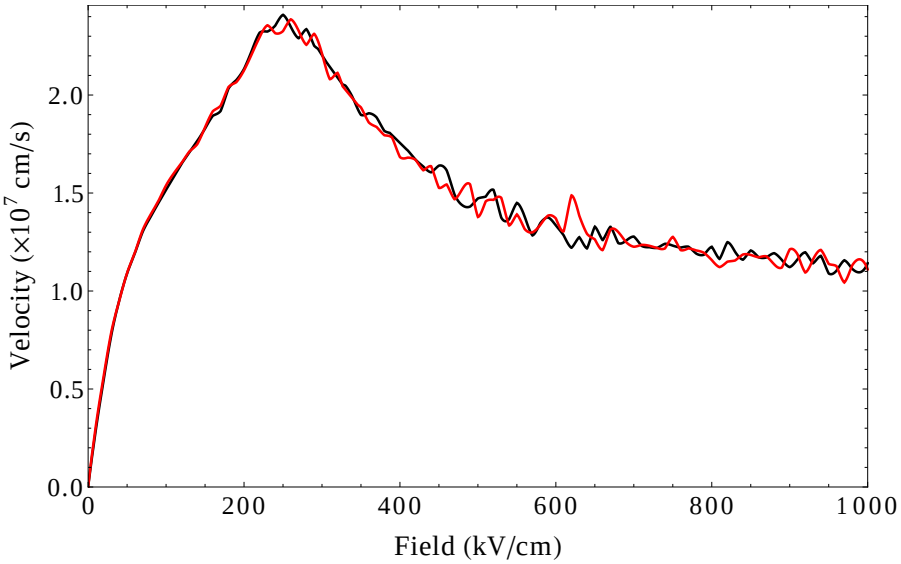

Figure 4.4) Velocity-field characteristics of ZnO as determined by a two-valley (red line) and a three valley (black line) EMC model when using the **k.p** band structure.

Encouragingly, however, this characteristic is comparable to those obtained by Bertazzi *et al.* [82] (figure 4, blue line) and Furno *et al.* [83] (figure 2) (from where many of the parameters we have used for the simulation have been taken), with a similar critical field (approx. 250 kV/cm), and a fairly similar peak velocity (this work suggesting 2.4×10^7 cm/s, compared with $\sim 2.2 \times 10^7$ cm/s as suggested by the referenced recent theoretical works.)

The energy-field characteristics, depicted in figure 4.5, however, indicate that there is a difference between the two models, whereby at larger fields, much after the point in which inter-valley transfer occurs, the three valley model reports a slightly lower average electron energy than the two valley model. This is an expected characteristic, as the electrons in the Γ_3 valley can be at slightly lower energies than those in the satellite valleys (as the Γ_3 valley minimum is slightly lower than the L-M valley minima), and it is favourable for electrons to be in a lower state if possible, which the Γ_3 valley enables. This is evident in figure 4.6, where a comparison has been made between the valley occupancy profiles of the two models. It can be seen that there is virtually no difference between the occupancies of the lowest

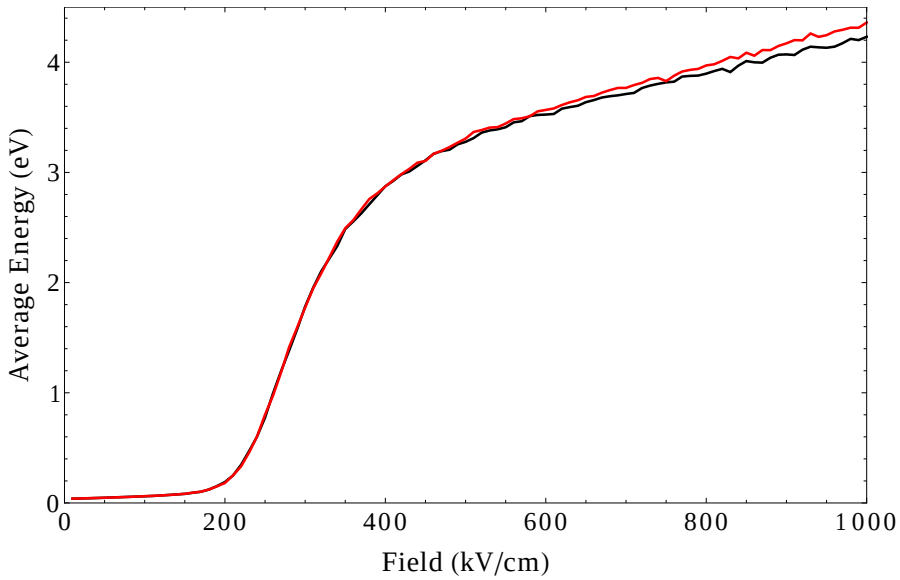

Figure 4.5) Average electron energy (relative to the Γ_1 valley minima) as a function of applied electric field across bulk ZnO as predicted by a two-valley (red line) and a three valley (black line) EMC model using the **k.p** band structure.

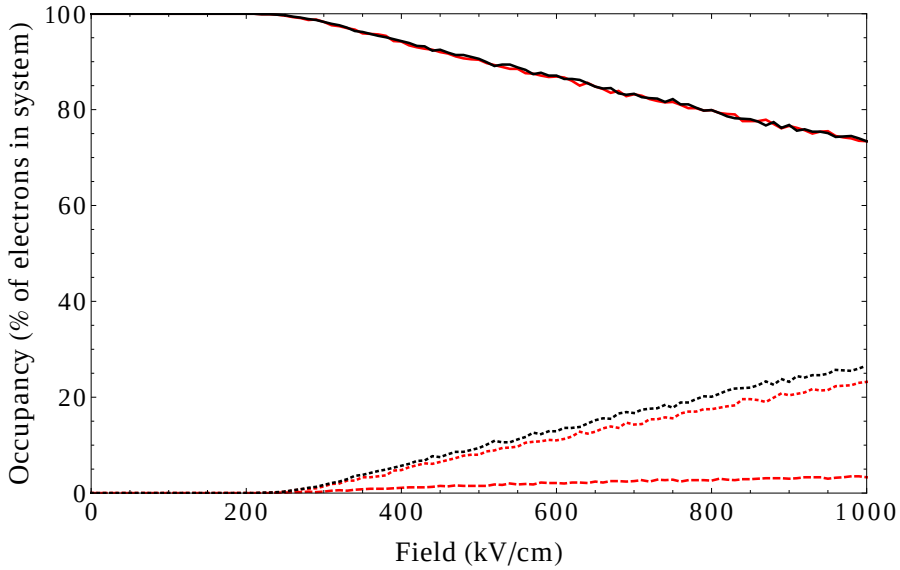

Figure 4.6) Valley occupancy (as a percentage of the system) in ZnO at various fields for the Γ_1 (solid), Γ_3 (dashed) and the L-M (dotted) valleys when using a two (red) and three (black) valley EMC model using the **k.p** band structure.

(Γ_1) valleys, with the only difference being that a proportion of the electrons that transfer to the L-M valleys in the two-valley model transfer to the slightly lower energy Γ_3 valley instead in the three valley model.

Whilst this demonstrates that the algorithm can be adapted to simulate a three-valley model successfully, it can be seen that, at least in this case, the additional computational time and code complexity required to simulate the third valley is difficult to justify. However, it is useful to be able to validate these changes so that for future work utilising this algorithm, should the three valley model be needed, it can be used in the knowledge that it works.

4.2. Cosine band-structure approximation demonstration

As the computational changes and updates that have been applied to the algorithm have been shown to produce results that are in excellent agreement to other works, both theoretically and experimentally, attention can now be focused on demonstrating that the implementation of the cosine band-structure approximation in the Γ valley within the algorithm produces believable results. To do this, the characteristics for GaN that are generated using the EMC code that utilises this approximation is compared with the characteristics from the EMC code that uses the **k.p** model. We also compare the velocity-field characteristics with data obtained through the use of a simple hydrodynamic model and the velocity data obtained through experimental work. For the EMC simulations, we revert to the use of a two valley model, and in both models, we use a spherical parabolic satellite valleys in the $M-L$ position . The GaN parameters used in these validation tests are listed in table 4.2.

Table 4.2) Parameters used in the tests for GaN. Parameters obtained from [6, 7, 44, 91–94].

Parameter (units)	GaN
Crystal Structure	Wurzite
Density (kg/m^3)	6150
Longitudinal sound velocity (ms^{-1})	6560
Transverse sound velocity, (ms^{-1})	2680
Non-polar optical deformation potential coupling constant, (eV/m)	10^{11}
Inter-valley scattering coupling constant, (eV/m)	10^{11}
Acoustic deformation potential, (eV)	8.3
Piezoelectric constant e_{15} (C m^{-2})	-0.3
Piezoelectric constant e_{31} (C m^{-2})	-0.55
Piezoelectric constant e_{33} (C m^{-2})	1.12
Energy gap (eV)	3.39
Static dielectric constant (ϵ_0)	8.9
High-frequency dielectric constant (ϵ_0)	5.35
Energy gap (between Γ_1 and satellite valley minima) (eV)	1.2
Number of satellite upper valleys	6
Effective mass, Γ_1 minima (used in **k.p** based simulations only) (m_e)	0.2
Effective mass, upper valley minima (m_e)	1.0
Polar optical phonon energy (meV)	91.2
Non-polar optical phonon energy (equivalent valleys) (meV)	91.2
Non-polar optical phonon energy (inter-valley) (meV)	91.2
Hexagonal lattice constant along c-axis ($\AA$)	5.186
Γ valley width (from minima to top of valley)(eV)	2.7
Charged carrier concentration (cm^{-3})	10^{17}

4.2.1. Velocity-field characteristics.

We first take a look at the velocity-field characteristics. The characteristics generated using the cosine band-structure approximation based EMC model is compared with the **k.p** approximation based EMC algorithm using the same parameters, ex-

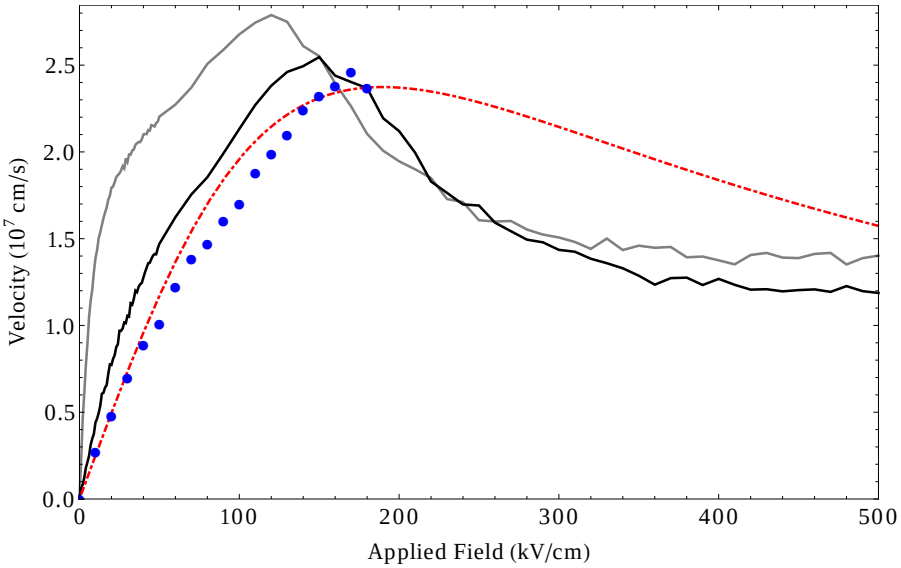

Figure 4.7) Velocity-field characteristics of GaN as predicted by Equation 4.2.1 (red dashed), generated using the EMC code with the **k.p** (solid grey) and the cosine (solid black) approximation, in comparison with experiment by Barker *et. al.*[59] (blue dots)

perimental data from Barker *et al.* [59], and a simple hydrodynamic model based on the energy balance equations, characterised by the equation,

$$\langle v_F \rangle = \frac{E_B a^2 e F \langle \tau_m \rangle}{2\left(\hbar^2 + e^2 F^2 a^2 \langle \tau_e \rangle \langle \tau_m \rangle\right)} \tag{4.2.1}$$

where F is the applied electric field, $\langle v_F \rangle$ is the average electron velocity in the direction of the field, $\langle \tau_e \rangle$ is the energy relaxation time and $\langle \tau_m \rangle$ is the momentum relaxation time. The relaxation times are set to averaged values for GaN around the inflection point in the band structure ($\sim 1.35\,\text{eV}$), as such, we use $\langle \tau_m \rangle = 30\,\text{fs}$ and $\langle \tau_e \rangle = 150\,\text{fs}$ [3, 95].

Figure 4.7 shows a comparison in the velocity-field characteristics, where it can clearly be seen that there is a marked difference between the two band-structure models. Whilst there is little difference in the saturation velocity, simulations using our cosine band-structure approximation suggest a critical field that is much closer to that suggested the simple hydrodynamic model and the experimental

data than the **k.p** model. Based on these comparisons, one can be satisfied that the cosine band-structure approximation does indeed provide a better fit to recent experimental data when compared with the **k.p** approximation. Though it is true that the hydrodynamic equation appears to be a closer fit with the experimental data, as stated above, $\langle \tau_m \rangle$ & $\langle \tau_e \rangle$ are the average energy and momentum relaxation times across all conditions and we assume that they are valid for all applied field strengths, which in reality, they are not. As such, these values treated as fitting parameters, rather than substituting in representative values for each field. As a result, the hydrodynamic model can only be used as a rough guide to the velocity field characteristics of the system in steady-state, the Monte-Carlo approach using the cosine band-structure, which does not require any experimental data to be provided allows for more insight into the behaviour of the system.

4.2.2. Other characteristics

We now turn our attention to a comparison of other steady-state characteristics generated by both the cosine band-structure approximation based and the **k.p** based EMC models, in order to ensure that the characteristics are consistent with each other. Figure 4.8 depicts the relationship between the steady-state occupancy of the Γ_1 valley with respect to the applied field, and figure 4.9 shows the energy-field characteristics of the two models. From the occupancy-field characteristic, it can be seen that the **k.p** model suggests that electrons begin to transfer to satellite valleys earlier that the cosine band-structure approximation predicts (with the first sign of the TE effect occurring at approximately 70 kV/cm in the **k.p** approximation as opposed to 100 kV/cm when using the cosine approximation). This is consistent with the energy-field characteristics, as it can be seen in figure 4.9

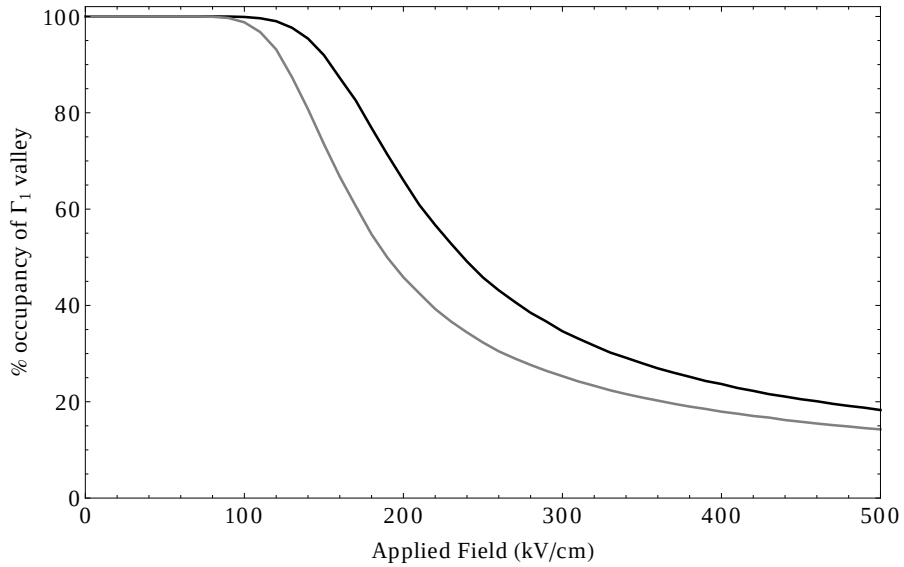

Figure 4.8) Percentage of electrons in system occupying the Γ_1 valley generated using the EMC code with the **k.p** (grey) and the cosine (black) approximation

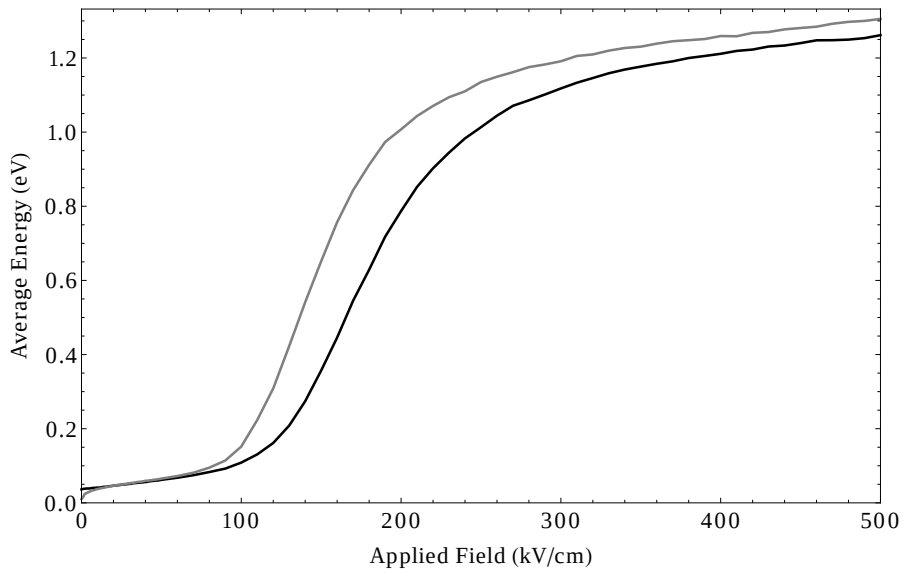

Figure 4.9) Energy-field characteristics generated using the EMC code with the **k.p** (grey) and the cosine (black) approximation

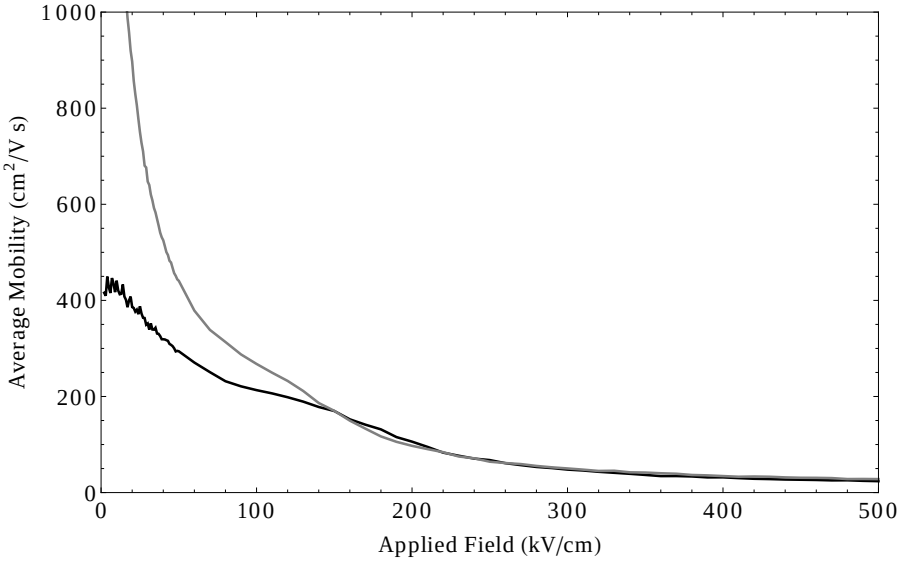

Figure 4.10) Electron mobility as a function of field when using the EMC code with the **k.p** (grey) and the cosine (black) approximations.

that the two characteristics begin to diverge at about $70 - 80\,\mathrm{kV/cm}$, where the **k.p** approximation suggests that the average energy of an electron begins to rise sharply with the field, unlike the cosine approximation, with this feature of the characteristic occurring closer to $100 - 110\,\mathrm{kV/cm}$. It is also consistent with the velocity-field characteristics as again, the critical field in the velocity-field characteristics is larger when the cosine band-structure approximation is used, similar to the energy-field characteristics.

We finally turn to the mobility-field characteristics (figure 4.10), and find that there is a large discrepancy between the two models at low field, something that was already evident by inspection of the velocity-field characteristics. The **k.p** approximation suggests a low field (at $2\,\mathrm{kV/cm}$) mobility of about $2300\,\mathrm{cm^2V^{-1}s^{-1}}$, whilst the cosine band-structure approximation yields a much lower low-field mobility of approximately $430\,\mathrm{cm^2V^{-1}s^{-1}}$, which is in very close agreement with work by Ilegems and Montgomery [96] ($440\,\mathrm{cm^2V^{-1}s^{-1}}$) and, more recently, experimental and theoretical works by Abdel-Motaleb and Korotkov [97] (also $440\,\mathrm{cm^2V^{-1}s^{-1}}$) for a carrier concentration of $10^{17}\,\mathrm{cm^{-3}}$. The high-field electron mobility is almost

identical in both models, which is not surprising as most electrons have transferred into the upper valley, which is identical in both models, and as can be seen in the velocity-field characteristics, the attained velocities are very similar.

4.3. Summary

In this chapter, the concepts introduced in chapters 2 & 3 have been subject to a series of tests to check their computational and physical validity. We first checked the re-engineered algorithm and found that it executed successfully, yielding results that match up with previous experimental data and other theoretical works for GaAs and InP, as well as producing almost identical results to the base code, as shown in [25]. We then extended the algorithm to include a third valley and tested our algorithm against recent ZnO theoretical results, and whilst we discovered that, at least in that case, the the addition of a third valley made little difference to the theoretical characteristics, it still gave an expected outcome and gives us confidence in this version of the algorithm should it be needed for later works.

The new approximation as described in chapter 3 was then integrated with the algorithm that had been tested in the earlier sections of this chapter, and found that the use of the new approximation gave a velocity field and mobility characteristic that agrees more favourably to experimental results obtained from GaN than the use of the **k.p** approximation in the model does, and produced other characteristics that are consistent with these results. We can therefore use the re-written algorithm and the new approximation for GaN and other materials that have a band structure containing a valley that can be closely approximated with the form presented in the new approximation, and be confident in the results that are obtained.

Chapter 5
Bulk Gallium Nitride

In previous chapters, we laid the foundations of our simulations for Gallium Nitride (GaN), describing the algorithms in chapter 2, developing a new analytic approximation for the GaN band structure in chapter 3, and checking that these new features and systems were successfully implemented in chapter 4. We can now focus on using these foundations to determine some of the transport properties of GaN. In this chapter, we will focus on bulk GaN, that is, we assume a uniform, infinitely large block of GaN and apply a constant, uniform electric field across the whole system.

Throughout this chapter, we use a two valley model, as used in the previous chapter, to simulate the system. It is assumed that the two valleys in the Brillouin zone are totally separate, and electrons can only transfer between the two valleys via non-polar optical phonon scattering (see section 2.1 for a detailed description on this model). Polar-optical, equivalent- and inter-valley non-polar optical, piezoelectric and acoustic phonon scattering are all considered, as well as charged impurity scattering, using expressions derived in chapter 3. Dislocation scattering is not considered as the effect of dislocations in the material is assumed to be negligible. The Ensemble Monte-Carlo (EMC) code coupled with the cosine band-structure approximation has been used to determine the properties of the system. All bulk simulations are run for a total simulation time of 4 ps to allow for enough time for the system to reach steady-state conditions, broken into 40000 time steps of 0.1 fs, and 15000 particles are used. We assume that the temperature of the system is 300K, and the concentration of charged impurities is $10^{23}\,\mathrm{m}^{-3}$.

We use the same GaN material parameters used in our simulations as those used

Table 5.1) Gallium Nitride simulation parameters at 300K. Parameters obtained from [6, 7, 44, 91–94].

Parameter (units)	GaN
Crystal Structure	Wurzite
Density (kg/m^3)	6150
Longitudinal sound velocity (ms^{-1})	6560
Transverse sound velocity, (ms^{-1})	2680
Non-polar optical deformation potential coupling constant, (eV/m)	10^{11}
Intervalley scattering coupling constant, (eV/m)	10^{11}
Acoustic deformation potential, (eV)	8.3
Piezoelectric constant e_{15} (C m^{-2})	-0.3
Piezoelectric constant e_{31} (C m^{-2})	-0.55
Piezoelectric constant e_{33} (C m^{-2})	1.12
Energy gap (eV)	3.39
Static dielectric constant (ϵ_0)	8.9
High-frequency dielectric constant (ϵ_0)	5.35
Energy gap (between Γ_1 and satellite valley minima) ($\Delta E_{\Gamma-L}$)(eV)	Varies from $0.7 - 1.9$
Number of satellite upper valleys	6
Effective mass, upper valley minima (m_e)	1.0
Polar optical phonon energy (meV)	91.2
Non-polar optical phonon energy (equivalent valleys) (meV)	91.2
Non-polar optical phonon energy (inter-valley) (meV)	91.2
Hexagonal lattice constant along c-axis ($\AA$)	5.186
Γ valley width (from minima to top of valley) (eV)	2.7

in the validation test in the previous chapter (repeated here in table 5.1), with one exception, being the energy gap between the Γ_1 and next lowest satellite valleys ($\Delta E_{\Gamma-L}$), as in the wurzite structure for GaN, the lowest satellite valley is at the M-L position [18]. An exact value for $\Delta E_{\Gamma-L}$ is currently unknown. Estimates of this separation have varied between 1.1 eV and 2.27 eV [6], though Semenenko *et al.* [94] published experimental optical measurements in 2011 suggesting that the size of this gap is between 1.18 eV and 1.21 eV.

Thus, we open this chapter by investigating how varying the valley separation

affects the steady-state transport characteristics of the system. We then investigate the effect of negative effective mass on the system under steady-state conditions comparing our two valley model with a one valley model, where the transferred electron (TE) effect is unable to occur as there is no satellite valley for electrons to transfer into. Using this, we are also able to determine how much of an effect the TE mechanism has on the system by comparing the models that include and exclude the TE effect. We close the chapter by studying how the characteristics of GaN during the first picosecond of the simulation, again, investigating the potential effects of negative effective mass through the use of a one-valley system alongside our two-valley models, and the contribution of the TE effect through the use of this direct comparison.

5.1. Comparison of Valley Separations

As the energy separation between the minima of the two lowest conduction band valleys is not exactly known, steady-state electron transport characteristics of GaN have been generated using five different values for the valley separation, 0.7 eV, 1.2 eV, 1.35 eV, 1.6 eV and 1.9 eV. Whilst the valley separation of 0.7 eV is outside of the range for the separation given in the literature [6, 18, 56, 94], using this separation allows us to investigate the cosine band-structure approximation in a regime where the TE & NM mechanisms are separate (that is, the threshold for the TE effect is well below that of the NM effect). However, we will not comment on the effect of the NM states in this section (we will be investigating this later in the chapter, see section 5.2).

We start by comparing the velocity-field characteristics for GaN for the selected

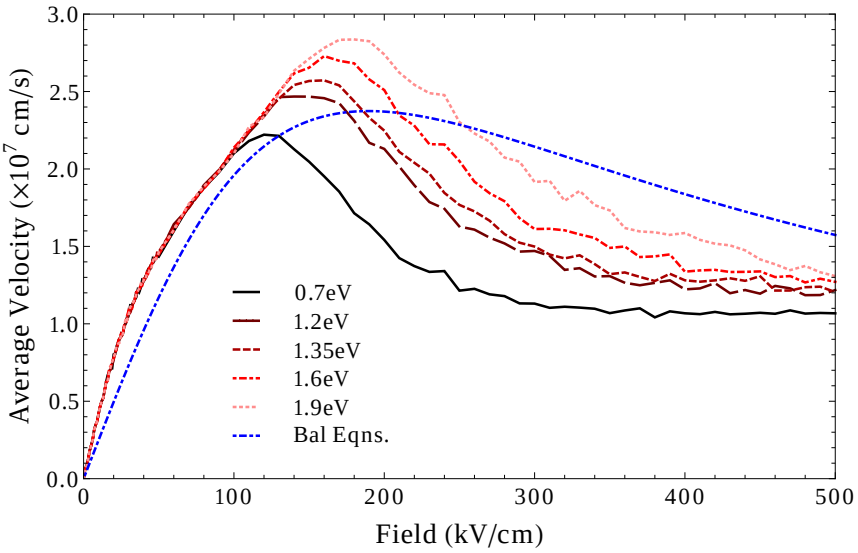

Figure 5.1) Average velocity-field characteristics for various valley separations (using the EMC simulation and the cosine band-structure approximation), and the calculated velocity-field characteristics when using the balance equations/simple hydrodynamic model (signified as Bal Eqns. in the legend).

values of $\Delta E_{\Gamma-L}$ (figure 5.1), along with the result as predicted through use of the simple hydrodynamic model based on the balance equations, (see equation (4.2.1)). We find that the saturation velocity, over this range of separation energies, ranges from 2.23×10^7 cm/s at a peak field of 123 kV/cm for a valley separation of 0.7 eV, to 2.84×10^7 cm/s at a peak field 175 kV/cm for a valley separation of 1.9 eV. These results are comparable other works, with Foutz *et al.* [44] suggesting a slightly higher peak velocity of 2.9×10^7 cm/s at a relatively low critical field of 140 kV/cm when the inter-valley separation is as high as 2.1 eV, (where the discrepancy between the critical field reported by them compared with our work is explainable through the choice of band structure approximation), while Yamakawa *et al.* [17] suggest a peak velocity of 2.8×10^7 cm/s at a critical field of 180 kV/cm using a full-band model with a valley separation of 2.0 eV, and produces very similar results to our model where the separation is 1.9 eV. At low field strengths, the velocities obtained are identical, as expected, due to the only difference between the models being the separation between the Γ and upper valleys, and hence, the threshold energy when

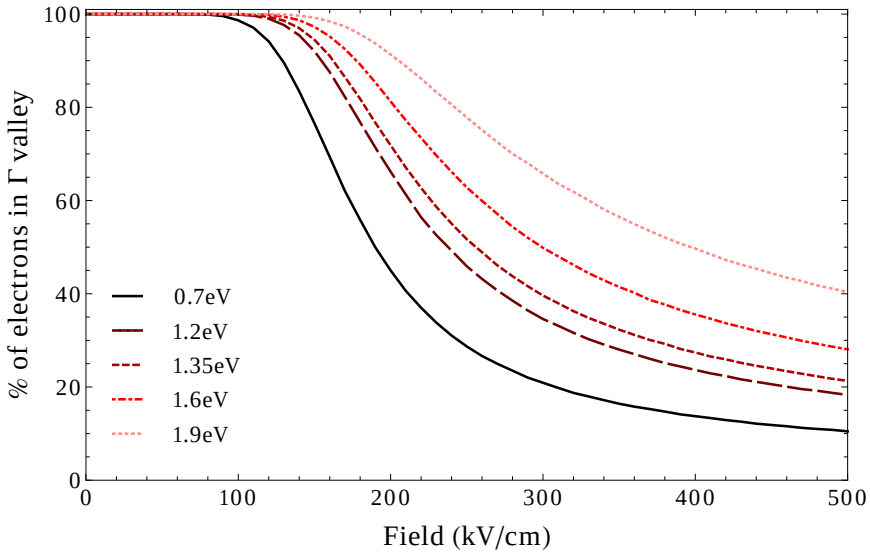

Figure 5.2) Percentage of electrons in the system occupying the Γ_1 valley in the steady state as a function of field for various $\Delta E_{\Gamma-L}$.

scattering into upper valleys can occur, $\Delta E_{\Gamma-L} - h\omega_{ij}$, that is, the valley separation energy less one inter-valley (IV) non-polar optical phonon, which is the threshold for inter-valley scattering by phonon absorption. We would therefore expect that the various characteristics will begin to diverge at approximately the field strength where IV transfer begins to occur, and by referring to figure 5.2, which shows the equilibrium occupancy of the Γ valley as a function of the applied field, we can see that this is broadly the case. It transpires that this "divergence" of the velocity-field characteristic for a particular separation occurs at the field strength when the occupancy of the Γ valley for that separation drops to approximately 98%. As high-field scenarios are reached, it can be seen that the velocity characteristics begin to converge, which again can be linked to the occupancy characteristics. Referring to figure 5.2, at high fields ($> 300\,\mathrm{kV/cm}$), the rate of change of the lower valley occupancy with respect to the applied field is shallower for the models utilising the lower valley separations than the larger separations. As the occupancy has a large effect on the velocity, it follows that the greater the change in occupancy, the greater the effect on the system velocity, thus providing the link between the

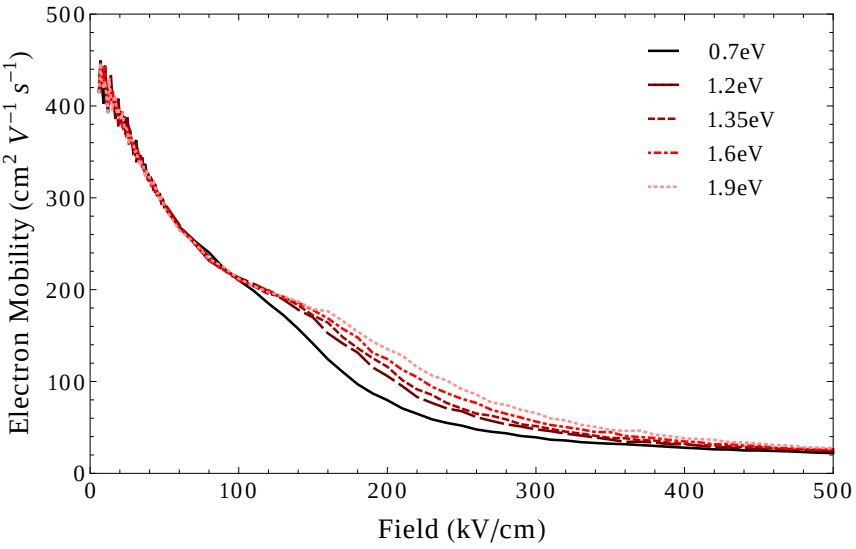

Figure 5.3) Average mobility of electrons in the steady state as a function of field for various valley separations (using the EMC simulation and the cosine band-structure approximation).

two characteristics, though we note that this convergence of characteristics is more pronounced in the velocity field characteristics than the occupancy characteristics.

Figure 5.3 depicts the electron mobility-field characteristics. As with the velocity-field characteristics, we can see that all models have yielded identical mobilities regardless of valley separation in the low-field regime, with electrons having an average mobility of approximately $430\,\mathrm{cm^2V^{-1}s^{-1}}$ at $2\,\mathrm{kV/cm}$, in excellent agreement with previous works, suggesting $440\,\mathrm{cm^2V^{-1}s^{-1}}$ [96, 97]. A divergence in the characteristics can be seen when the occupancy of the Γ valley reaches approximately 98%, as expected, due to the link between mobility and velocity. In effect, a noticeable "kink" can be seen in each characteristic at the fields where electron transfer begins to take effect. At high-field, again, much like in the velocity-field characteristics, we note that the mobility-field characteristics converge. However, the mobilities converge with nearly identical mobilities being recorded over all valley separations, with mobilities of $20 - 25\ \mathrm{cm^2V^{-1}s^{-1}}$ occurring when a field strength of $500\,\mathrm{cm^2V^{-1}s^{-1}}$ is applied.

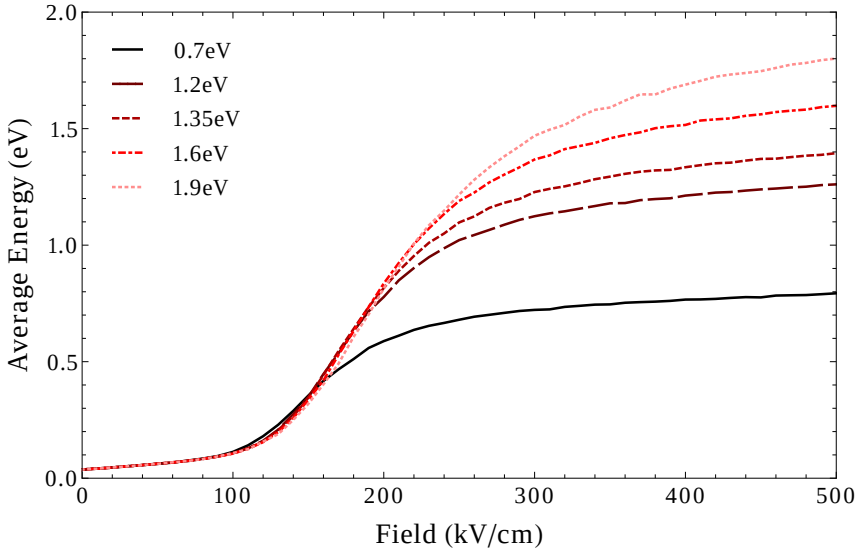

Figure 5.4) Average energy-field characteristics for various valley separations (using the EMC simulation and the cosine band-structure approximation). Energy is relative to the Γ_1 valley minima at the bottom of the conduction band.

We now look at the energy-field characteristics for the different valley separations, as shown in figure 5.4. First commenting on the general shape of all the models, we note that they all show this elongated "S" shape characteristic, something that has already been seen when investigating other materials in the previous chapter. This "S" shape arises from the different processes that occur in these materials. In the low-field regime, electrons do not gain momentum from the field quickly, and thus, gain energy at a lesser rate than would be the case with larger fields, due to the elastic charged impurity scattering being dominant at low energies over a range of applied fields. When electrons are unable to gather energy quickly, they have to spend longer in this low energy region, thus encountering more scattering events, increasing the probability that a momentum-relaxing collision that sets the electron's momentum against the applied field (which ensures that the electron must first lose energy as it loses momentum against the field, and hence overall) occurs. If the electrons are able to gain enough energy so that impurity scattering does not play a large role, the inelastic polar-optical phonon (POP) scattering mechanism

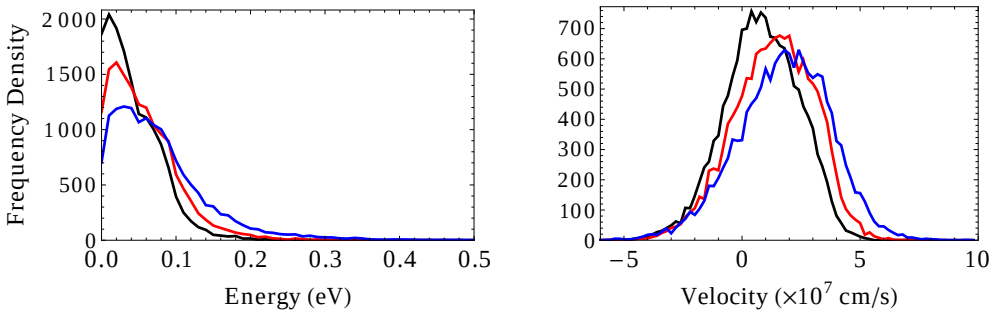

Figure 5.5) Energy (left) and velocity (right) number distributions under steady-state conditions when fields of 25 kV/cm (black), 50 kV/cm (red) and 80 kV/cm (blue) are applied to the system (using the EMC simulation and the cosine band-structure approximation). These distributions are near-identical for all valley separations considered.

(particularly in the energy-reducing case where scattering occurs due to phonon emission) becomes dominant. At sub-0.2 eV energies, electrons gaining momentum and energy slowly are very likely to encounter this scattering mechanism which decreases the electron's energy by 0.1 eV, placing it in the high impurity scattering rate region. This makes it difficult for the affected electron to gain energy, thus keeping the average electron energy low.

Whilst we see that there is a low average energy (comparable to those suggested by the thermal distribution) at these low fields, referring back to the velocity-field characteristics in figure 5.1, it appears that there is a fairly large increase in the average velocity of the system. In figure 5.5, where the electron energy and velocity distributions are displayed for sample fields in the low-field regime, we can see that at 80 kV/cm, unsurprisingly, there is a larger "tail" in the energy characteristics, causing a noticeable shift in peak velocity and a slight broadening in the velocity distribution. This seemingly disproportionate shift is explainable by combining the band-structure energy and velocity relations (equations 3.0.1 and 3.1.6) to obtain

an energy-velocity relation:

$$v_k = \frac{E_B a}{\hbar}\sqrt{\frac{E_B E_k - E_k^2}{E_B^2}} \tag{5.1.1}$$

where E_B is the width of the Γ band and a is the c-axis lattice constant. The relation suggests that, for the first half of the band, the rate of increase in velocity with respect to energy starts high, but the potential increase in velocity diminishes as energy is increased, until the mid-point of the band is reached. Thus, the (relatively) large increase in the average velocity caused by a small change in average energy is a physical occurrence.

Beyond 100 kV/cm, the rate of energy increase with regards to the field increases dramatically. Most electrons are able to gain enough energy quickly so that many electrons are not affected by the impurity scattering and the peak in POP scattering trying to push the electrons back to this region, however, the systems reach equilibrium at energies well below the valley separation energy. This equilibrium occurs, again, mostly due to the POP scattering by phonon emission rate. Unlike the charged impurity scattering, which is only dominant for electrons with energies up to 0.1 eV, POP by emission is dominant for electrons with energies of 0.2 eV up to energies just larger than the valley separation (there are, of course, other scattering mechanisms that affect the system, but their contribution is negligible compared to POP emission). There is one critical difference between the impurity and POP scattering mechanisms, however, that ensures that there is this growth in the energy-field characteristics. While charged impurity scattering is isotropic, POP scattering is anisotropic in such a way that an electron is more likely to be scattered in the current direction of travel - which for most electrons in this scen-

ario, is in the general direction of the field. Thus, electrons in the mid-field regime generally encounter energy reducing scattering mechanisms, but are also less likely to be back scattered than in the low field regime, meaning that it is easier for electrons to regain energy that they have lost. Higher applied fields, as it can be seen from figure 5.4, means that electrons can reach a higher energy, on average, due to faster rate of gain of energy means that electron can gain more energy between scattering events.

In high-field regimes, the average energies of the systems are fairly steady around the valley separation energy (i.e. the third part of the "S"). The inability of the system to attain average energies much higher than this can be explained by the same reasoning as given in the low-field regime, as most electrons will have transferred into the upper valleys (refer back to figure 5.2) as they are able to reach energies where IV scattering is dominant with a relatively small number of scattering events. Once electrons transfer to the upper valleys, they tend to have low energies relative to the local minimum, where impurity and POP by emission are highly dominant. Indeed, we find that the scattering rates in the upper valleys are approximately an order of magnitude larger than their counterparts in the lower valley, making it more difficult for electrons to reach high energies (relative to the upper valley minimum). Thus, we end up with a similar characteristic to that found at low-field, albeit centred around the upper valley minima rather than the thermal energy.

We can now explain how varying the valley separation makes a difference between the two models with ease. As we would expect through comparison with the other characteristics presented, there is little difference between the models in low-field scenarios, only seeing variations in the energy-field characteristics at high-field.

As explained in the previous paragraph, we see the characteristics for each model reach energies around the valley separation in question before increases in the applied field make little difference to the average energy of the system, due to the hugely inhibitive scattering rates in the upper valleys, particularly around the valley minima. Thus, models utilising a larger valley separation have a larger mid-field phase, as larger fields are required in order to be able to ensure the majority of the electrons in the system are able to attain the energies required.

5.2. Effect of Negative Effective Mass

We now focus on the effect of the negative effective electron mass (NM) states in the bulk material. We start by analysing the effect that the potential NM states have on the system in the absence of other mechanisms that could potentially cause a negative differential velocity (NDV) in the direction of the applied field, that is, we remove the possibility of the TE effect occurring. To do this, we run the model with the electrons confined to the Γ valley only, and compare this with the results obtained from the two valley model. For the two valley model, only valley separations of 1.2 eV and 1.9 eV will be considered.

It can already be seen from figure 5.1 that the TE mechanism has a sizeable effect on the velocity-field characteristics of the material, as the saturation velocity and the critical field are both decreased by assuming a lower valley separation. In figure 5.6, the one-valley model is plotted alongside the two valley model where $\Delta E_{\Gamma-L}$ is set to 1.2 eV and 1.9 eV. Focussing on the one-valley model at first, with the TE mechanism unavailable, a noticeable NDV still occurs, with the model predicting a saturation velocity of 2.98×10^7 cm/s at a critical field of 185 kV/cm. We find

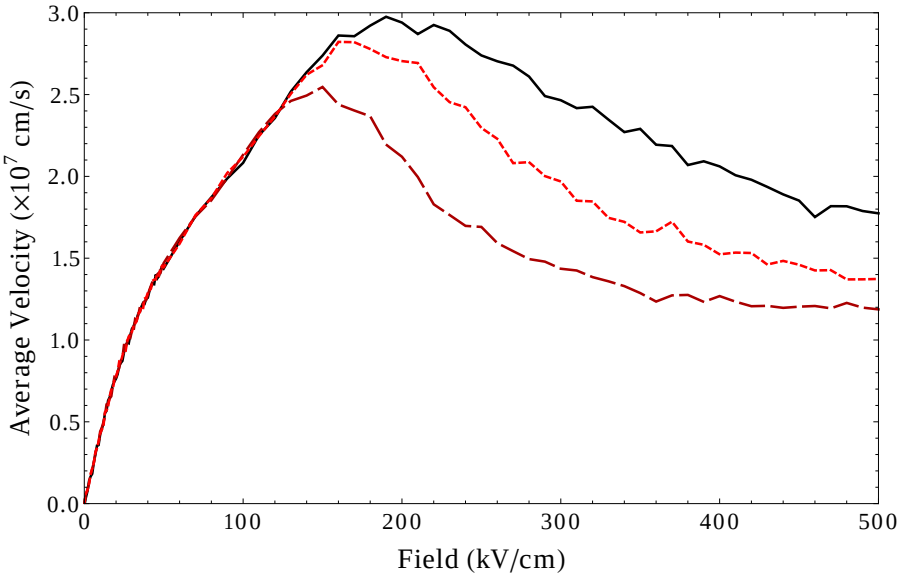

Figure 5.6) Velocity-field characteristics for GaN when a one valley model is used (solid line), and a two valley model is used where the energy separation of the two valleys is $1.2eV$ (long dashed) and $1.9eV$ (short dashed), using the EMC simulation and the cosine band-structure approximation for the lower band.

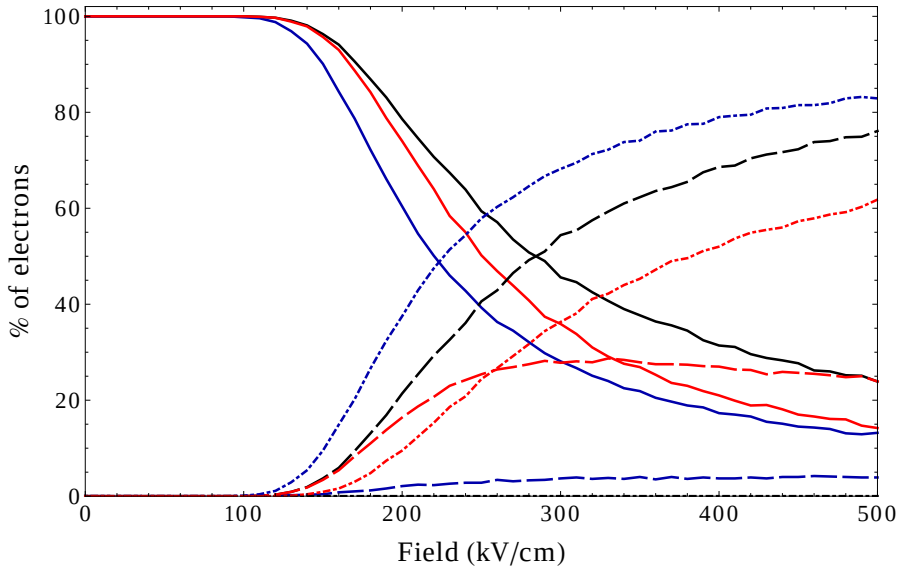

Figure 5.7) Percentage of electrons in the system occupying the Γ_1 valley with a positive effective mass (solid lines) or a negative effective mass (dashed lines) in the direction of the applied field, and the satellite valley (dot-dashed line) as a function of field for the one-valley model (black), and the two valley model where the valley separation is $1.2eV$ (blue) and $1.9eV$ (red)

that there is a dominant proportion of NM states in the one band model, with NM occupation reaching approximately 75% of the system at 500 kV/cm (see figure 5.7), causing this NDV.

If NM transport was a dominant transport mechanism in the two valley model in the mid-field regime (that is, more electrons are in NM states than have transferred into the upper valley around 200 kV/cm where velocity saturation occurs), then the expectation would be that the velocity-field characteristics of the one-valley model and two-valley model in question would be very similar, i.e. the characteristics would share the same velocity saturation point, with the potential for the characteristics to diverge beyond this point in the NDV region. We find that for a valley separation of 1.9 eV that this is not the case, with the velocity saturation being 0.14×10^7 cm/s lower than suggested by the one-valley model at 2.84×10^7 cm/s, occurring at the lower critical field of 175 kV/cm. Though there are more electrons in NM states than have transferred to the upper valleys, it would not be fair to state that NM transport is dominant, for example, when a field of 180 kV/cm is applied to the system, there is only 10% of the system in NM states compared with 4% of electrons that have transferred to upper valleys. At high-fields, the TE effect becomes a much more favoured process, indeed, suppressing the ability of the electrons to reach NM states, with NM state occupation reaching a maximum of 28% of the system at a field of 330 kV/cm, before decreasing at the expense of the upper valley occupation, which reaches above 60% of the system when a field strength of 500 kV/cm is applied. When the valley separation is set to 1.2 eV, we find that the TE effect is completely dominant, with only 4% of the system ever reaching NM states. If the recent experimental measurements suggesting that this valley separation is between 1.18 eV and 1.21 eV [94] hold true, the effects of NM

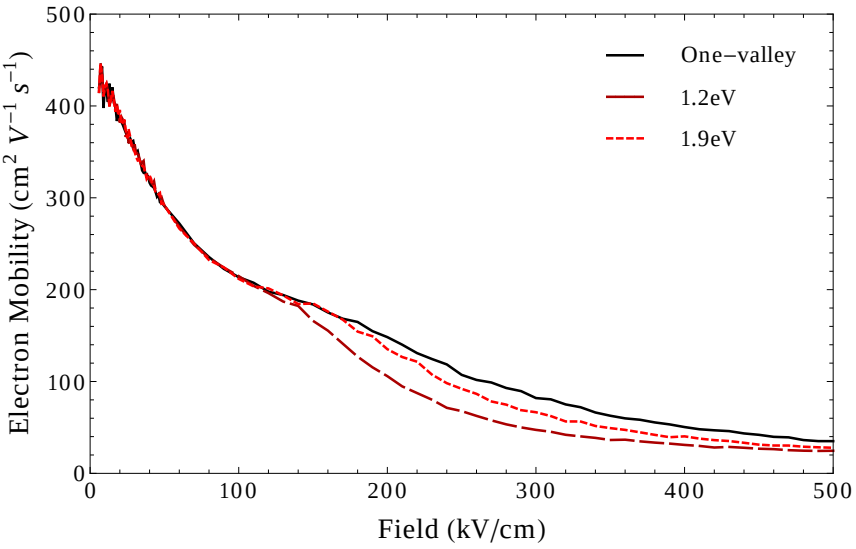

Figure 5.8) Mobility-field characteristics for GaN using the one-valley and two-valley models (using the EMC simulation and the cosine band-structure approximation for the lower band).

transport in GaN are negligible in the steady state regime.

Figure 5.8 depicts the electron mobility-field characteristics. Again, focussing on the one-valley model, it can be noted that the mobility is appreciably larger than that of the two-valley model the in high-field regime. Interestingly, the "kink" that can be seen in the two-valley model characteristics arising from the TE effect (as discussed previously) can also be seen in the one-valley model at around 170 − 180 kV/cm, although it is a much less aggressive and is difficult to pinpoint. Much like with the velocity-field characteristics, the effect of NM states alone (from the one valley model) and the relative contribution of the TE effect by adding a second valley can be seen, and again, it can be seen that the TE effect is more dominant than the effect of the NM states, especially in the case where the valley separation is 1.2 eV. In the case where the valley separation is 1.9 eV, the TE effect also dominates the overall form of the characteristic, though the field strength the "kink" occurs at is close to that of the one-valley NM characteristic, suggesting that there is some contribution from the NM states (which is what is expected from figure 5.7,

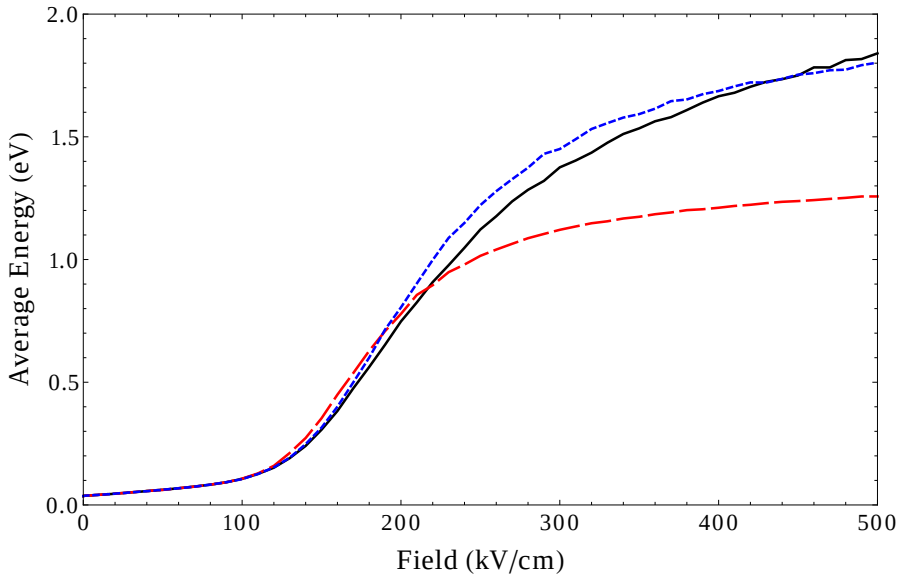

Figure 5.9) Energy-field characteristics of the one-valley model (black), and the two valley model where $\Delta E_{\Gamma-L} = 1.2\,\text{eV}$ (red) and $\Delta E_{\Gamma-L} = 1.9\,\text{eV}$ (blue) (using the EMC simulation and the cosine band-structure approximation for the lower band).

where in the mid-field range, there is a slightly higher population of electrons in NM states than there are in the upper valley).

Figure 5.9 shows the energy field characteristics of these models. As was shown in figure 5.4, the two valley models reach average energies that are roughly equal to the valley separation at high fields, due to the large scattering rates that are experienced in the upper valley. Clearly, the same cannot be said for the one valley model as there is no upper valley and thus no valley separation that can be used to explain high-field scenarios. It is not surprising that the low-field characteristics are practically identical to the results obtained through the use of the two-valley model, as the only difference between the two models is the existence the transferred electron model, and the effect that this has on the system has been explored in an earlier section. Yet, we find a similarity between the two-valley and one-valley models, in that the "S" shape can still be observed in the one-valley model, though in the high-field regime, there is less of a "plateau" as seen in the two valley model. The shape of the characteristic in the high-field regime is dictated by two

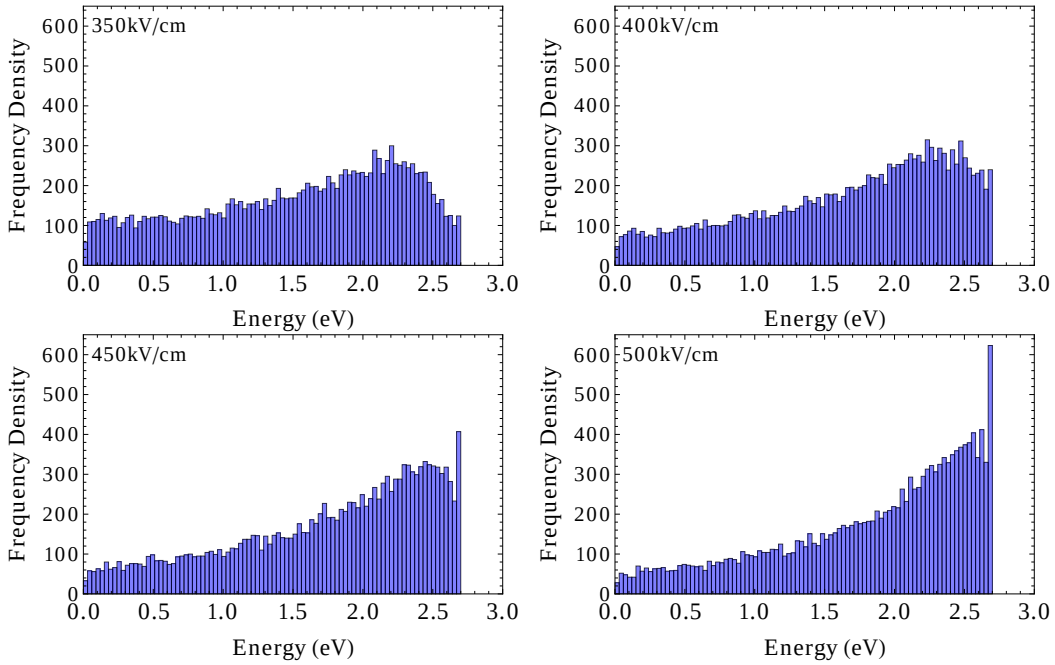

Figure 5.10) Energy number distributions of the system in steady state for various high-field scenarios when using the one band model (using the EMC simulation and the cosine band-structure approximation).

different mechanisms, all scattering rates towards the band edge are very large, and that some electrons are reaching the band edge unable to increase in energy any further, decreasing the overall rate of increase in the energy. We can illustrate this in figure 5.10, where steady-state energy distributions are shown for various high-field models, it is quite clear to see that as the field strength is increased, the position of the peak in the distribution increases. However, at fields above 400 kV/cm, there is a large proportion of electrons at the top of the band (at $2.7eV$), unable to gain any more energy as they are unable to transfer to an upper valley. This therefore inhibits the rate of increase of the average energy with respect to the field in the energy-field characteristics, causing the characteristic seen at high-field in the one-valley model.

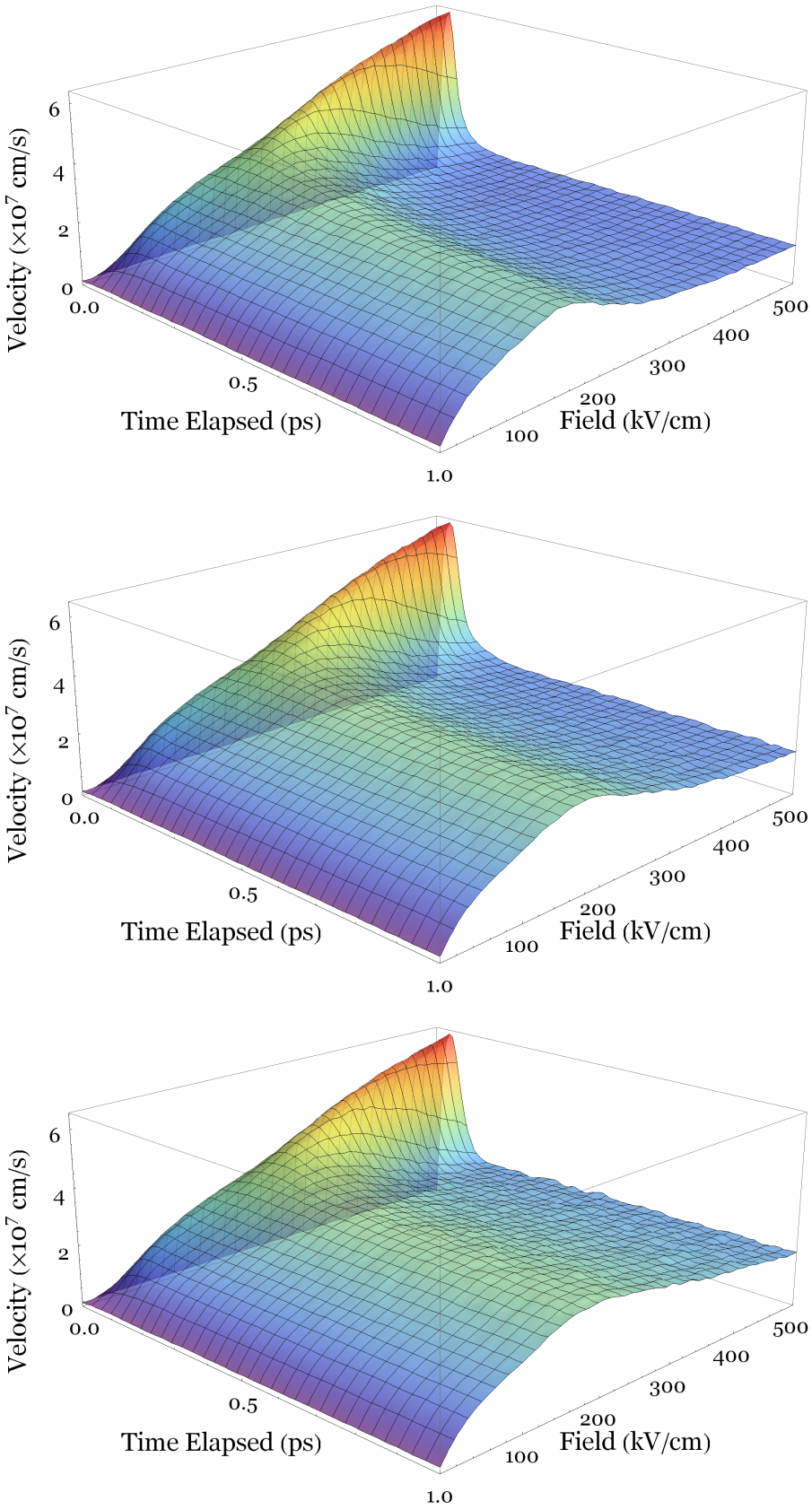

Figure 5.11) Time evolution of average electron velocity for fields of $1 - 500\,\mathrm{kV/cm}$, using the two valley model where the Γ-L valley separation is a) 1.2 eV and b) 1.9 eV, and c) using the one-valley model (using the EMC simulation and the cosine band-structure approximation for the lower band).

5.3. Transient Characteristics

We now focus on the transient characteristics of GaN, using the two-valley model with valley separations of $1.2eV$ and $1.9eV$, as well as the one-valley model as described previously. To do this, we assume that before the beginning of the simulation ($t < 0$ ps) there was no applied field and the electrons have a thermal spread of energies, and that at $t = 0$ ps, the required field is immediately applied across the system. Snapshots of ensemble-averaged data is taken over the course of the simulation, as has been previously described in chapter 2.

We start by looking at the the velocity-field-time characteristics for the first $1ps$ of transport, as shown in figure 5.11. In all three cases, it takes no longer than $1ps$ to reach equilibrium, so by looking at the right edge of each of the graphs (at a time of 1 ps), the steady state velocity-field characteristics are clearly visible. One obvious feature visible in all three models is that a velocity "peak" can be seen at larger applied field strengths. This effect is generally seen when the applied field strength is larger than that of the critical field as seen in the steady-state velocity-field characteristics (i.e. the field at which the steady-state velocity saturation point/peak occurs). These peaks occur at approximately 100 fs after the start of the simulation, though this is dependant on the field applied across the system and the valley separation (or lack thereof). We term the occurrence of this transient peak in velocity "velocity overshoot", as in these scenarios, the average electron velocity is larger than the expected steady-state velocity for a small period of time, before relaxing to equilibrium values.

In order to investigate this phenomenon, we analyse the velocity-time characteristics for all three models in the mid-field case, where the transient profiles begin

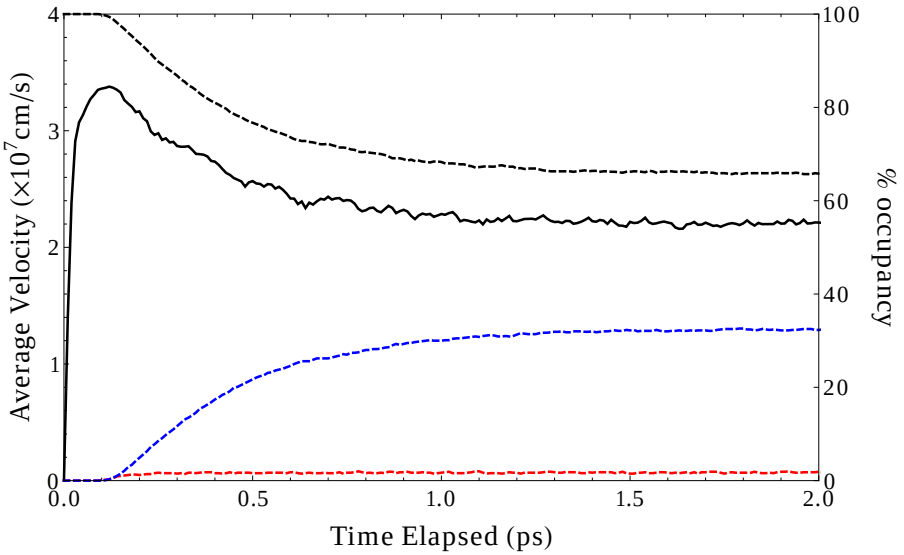

Figure 5.12) Transient characteristics when the valley separation is 1.2 eV and a field of 190 kV/cm is applied (using the EMC simulation and the cosine band-structure approximation for the lower band). Solid line, left axis, velocity. Dashed lines, right axis, percentage occupancy, with positive (black) and negative (red) states in the Γ valley, and states in the upper valleys (blue).

to display small, broad velocity overshoots, and in high-field scenarios, well beyond the critical field, in order to investigate a large and narrow overshoot profile.

5.3.1. Mid-field transient transport

In the mid-field regime, we take transient measurements at a field strength of 190 kV/cm, which is just beyond the critical field for all three models.

We begin by discussing the transient properties of the two valley model when we set the valley separation to 1.2 eV, with the velocity and occupancy-time characteristics as shown in figure 5.12. A small velocity overshoot peak can be seen, with the peak velocity of the system reaching 3.38×10^7 cm/s after 120 fs, before slowly falling back to a steady state velocity of 2.21×10^7 cm/s, reaching equilibrium after approximately 1 ps. It is quite clear to see that there is almost no contribution from electrons in NM states, with maximum NM state system occupancy reaching just 1.9%, thus suggesting that the TE effect (which reaches 32.3% at equilibrium)

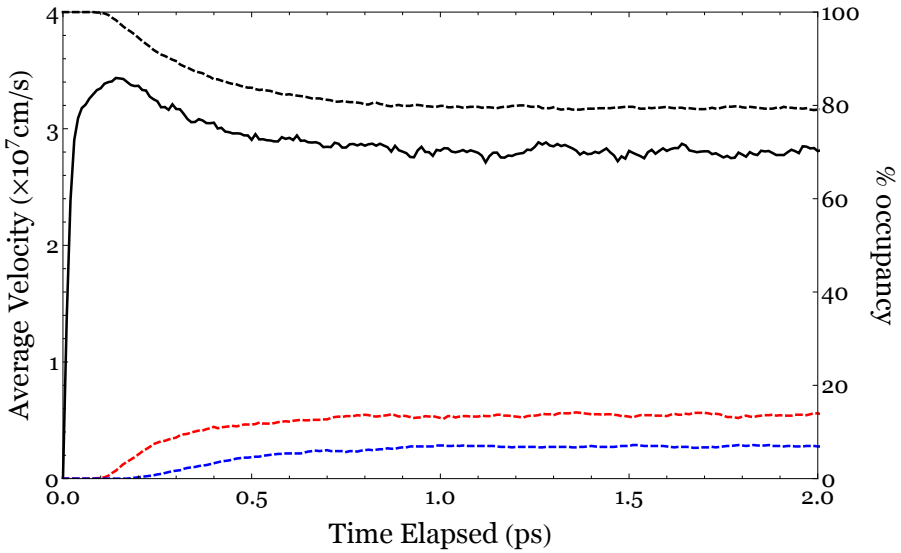

Figure 5.13) Transient characteristics when the valley separation is 1.9 eV and a field of 190 kV/cm is applied (using the EMC simulation and the cosine band-structure approximation for the lower band). Solid line, left axis, velocity. Dashed lines, right axis, percentage occupancy, with positive (black) and negative (red) states in the Γ valley, and states in the upper valleys (blue).

is driving the NDV characteristic of the system, the time that the peak occurs at coincides with the start of electron transfer to the upper valley. Before this point, however, there is a significant decrease in the average acceleration before the TE takes effect. This is an effect of the shape of the band-structure around the Γ valley, as electrons approach the required energy to enter NM states, the effective mass increases, and thus, the acceleration of the particles decreases.

When the valley separation is increased to 1.9 eV, the critical field is at 170 kV/cm so we look at the characteristics at 190 kV/cm, as shown in figure 5.13. The velocity characteristic is not overly different to that found in the previous model, a slightly larger peak velocity of 3.44×10^7 cm/s is observed after about 140 fs, before falling to a steady state velocity of 2.8×10^7 cm/s after around 1 ps, which is slightly less time than previous model required to reach steady state conditions, though it is difficult to say how much of this difference can be linked with the change in valley separation. Encouragingly, this result is similar to that obtained by Joshi *et al.*

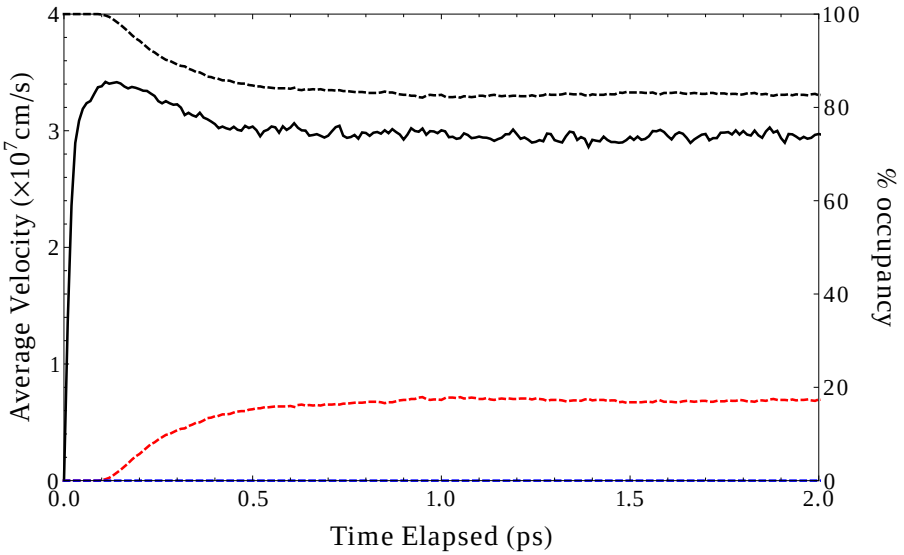

Figure 5.14) Transient characteristics when the one-valley model is used and a field of 190 kV/cm is applied (using the EMC simulation and the cosine band-structure approximation). Solid line, left axis, velocity. Dashed lines, right axis, percentage occupancy, with positive (black) and negative (red) states in the Γ valley.

[6], who suggest a slightly larger peak velocity of 3.8×10^7 cm/s after about 120 fs, using a slightly larger $\Gamma - \mathrm{L}$ valley separation of 2.27 eV and the **k.p** approximation.

It should be noted that the drop in velocity from the peak to the steady state value, an approximate change of 0.6×10^7 cm/s, is also less than that seen for the smaller valley separation of 1.2 eV, which saw a change of 1.16×10^7 cm/s. The peak velocity, and hence the occurrence of the NDV, is found to be present before the electrons begin to transfer into the upper valleys at 180 fs. We can thus assume that the shape of the band structure, in particular, the NM effect caused by it, has a noticeable effect on the system. Indeed, while the occupation of NM states is never dominant, it is more significant than the effect of electrons in the upper valley, with 14% of the system in NM states in the Γ valley whilst only 7% of electrons are in the upper valley under steady state conditions.

Turning to the one-valley model, (figure 5.14) we can investigate the effect of the NM states if the TE effect is eliminated. When using the two-valley model with a valley separation of $1.9eV$, it was noted that the velocity peak occurred before

the electron transfer took place. Therefore, we would expect that there is a similar peak velocity which occurs after a similar amount of time, which is indeed the case, with a peak velocity of 3.41×10^7 cm/s occurring after 140 fs, the difference in the peak velocity can be attributed to the random nature of the system. The differences occur when relaxing back to the steady state characteristics. The most noticeable difference that can be seen is the time it takes for the models to reach steady state conditions, while it takes the two valley model about 1 ps, the one-valley model takes about 0.4 ps, meaning that electrons that transfer to the upper valley require more time to relax to steady state conditions. As we have already seen from the steady state characteristics, the equilibrium velocity suggested by the one-valley model is slightly higher (at 2.98×10^7 cm/s). This is because NM states indicate a deceleration of electron velocity as energy increases and thus electrons enter these states with large velocities, whilst electrons that transfer into upper valleys lose a lot of their momentum quickly and start at low velocities, as they are suddenly much closer to a valley minima. Furthermore, the acceleration of electrons in upper valleys are generally impeded due to larger scattering rates, keeping upper valley velocities low, whilst an electron entering a NM state starts at the maximum attainable velocity, which decreases as it's energy and wave-vector increases. As such, an electron being in a NM state does not infer a low electron velocity.

5.3.2. High-field transient transport

We start looking at the high-field transport model by focussing on the two valley model with a valley separation of 1.2 eV. Figure 5.15 shows the aforementioned velocity-time characteristics along with the transient occupancy data of the Γ valley (where the positive and negative effective mass contributions have been sep-

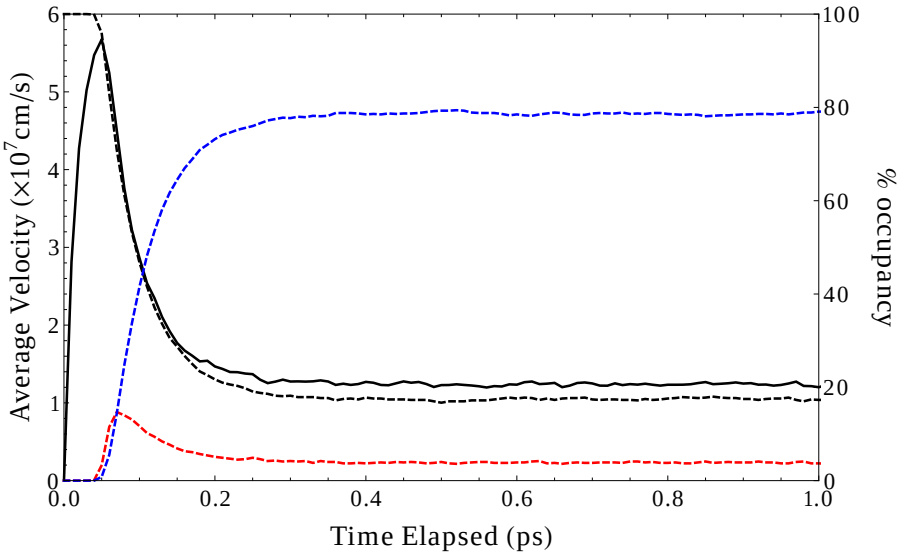

Figure 5.15) Transient characteristics when the valley separation is 1.2 eV and a field of 400 kV/cm is applied (using the EMC simulation and the cosine band-structure approximation for the lower band). Solid line, left axis, velocity. Dashed lines, right axis, percentage occupancy, with positive (black) and negative (red) states in the Γ valley, and states in the upper valleys (blue).

arated) and the upper valley contribution. It can be seen that the peak velocity of 5.62×10^7 cm/s occurs just 50 fs after the field has been "switched on", dipping back to the equilibrium velocity of 1.3×10^7 cm/s after about 300 fs. The occupancy characteristics match the transient profile of the velocity, we can see that the positive mass system occupancy of the Γ valley begins to drop at around 40 fs, just before the velocity peak, with electrons moving into NM states in the Γ band and the TE effect beginning to transfer the electrons to the upper valley occurring at almost the same time. As the occupancy of the upper valleys increases, it can be seen that the system velocity decreases, with the equilibrium upper valley occupancy of 79% occurring at the same point where the steady-state velocity is reached. NM states are never a dominant factor in this case, with a maximum of 13% occupancy before dropping down to 4%, before steady-state conditions are reached.

Whilst it appears that there is a slight dominance of NM states over the TE

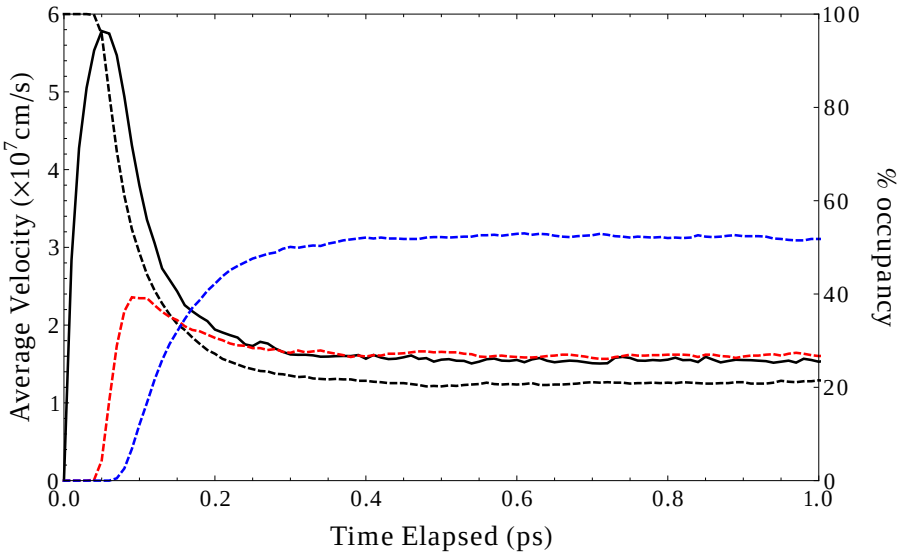

Figure 5.16) Transient characteristics when the valley separation is 1.9 eV and a field of 400 kV/cm is applied (using the EMC simulation and the cosine band-structure approximation for the lower band). Solid line, left axis, velocity. Dashed lines, right axis, percentage occupancy, with positive (black) and negative (red) states in the Γ valley, and states in the upper valleys (blue).

effect for a very brief period of time, as explained previously, NM states have a much lesser effect on the system when they first appear, when compared to the TE effect, as an electron that has entered a NM state simply by attaining enough energy in the Γ band still has close to it's maximum velocity while the TE effect instantaneously affects the momentum of the electron in question, thus affecting the system much less. Hence, we can assume that the effect of the NM states when they first appear is negligible and therefore play little to no part in the formation of the velocity characteristic.

When the valley separation is set to 1.9 eV, we see that the velocity peak of 5.78×10^7 cm/s occurs after 55 fs, which, again, is similar to data by Joshi *et al.* [6], who suggest a peak velocity of 6.2×10^7 cm/s after about 70 fs. On closer inspection of figure 5.16, it can be seen that there is a more pronounced effect from the NM states. This is something that is expected, some of the mid-energy electrons that would have transferred into the upper valley when the valley separation is 1.2 eV are

unable to do so in this model, as the threshold for IV transfer (at little over 1.8 eV by phonon absorption) is much higher. This means that there are more electrons in the lower valley, and due to the fact that the threshold to enter a NM state is at 1.35 eV in our models, there is suddenly a sizeable proportion of electrons undergoing NM effects. This difference between the two threshold energies also explains why the NM occupation begins to increase before inter-valley (IV) transfer takes place, as the electrons simply must attain enough energy to enter NM states before being able to be transferred. We see a NM occupation "overshoot", much like the one that was seen when the valley separation was 1.2 eV, however, a much larger maximum occupation is seen at just under 40%, before the IV transfer rate dominates over the rate at which electrons enter these NM states, pulling the NM occupancy back down towards 24% in the steady state regime. Again, the occupancy of NM states never dominates the characteristics of the system, with a large transfer of electrons into the upper valley, though clearly, the significant proportion of NM states do have an effect on the system properties, with the velocity peak occurring at 55 fs, just before IV transfer begins at approximately 60 fs into the simulation, suggesting that the deceleration of electrons by the field in the NM states causes the peak to be earlier than would otherwise be anticipated.

We now look at the system without the IV transfer mechanism, with figure 5.17 showing the characteristics for the one-valley model. Quite clearly, it can be seen that it does not take long for the NM states to dominate in the Γ valley, with there being 50% occupancy of NM states 85 fs into the simulation. We find that the peak velocity of 5.77×10^7 cm/s occurs at a simulation time of 55 fs, which is almost identical to the peak velocity obtained in the two valley model where the valley separation is set to 1.9 eV, for reasons as explained for the mid-field characteristics,

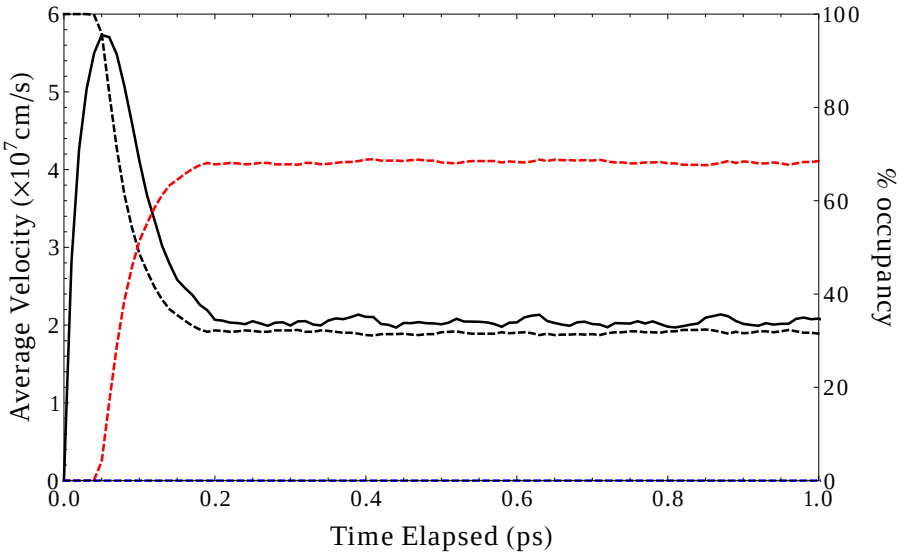

Figure 5.17) Transient characteristics when the one-valley model is used and a field of 400 kV/cm is applied (using the EMC simulation and the cosine band-structure approximation). Solid line, left axis, velocity. Dashed lines, right axis, percentage occupancy, with positive (black) and negative (red) states in the Γ valley.

this is to be expected in this two-valley case, the peak occurred before any electron transfer took place. We can therefore be confident that NM states has a noticeable effect on the model in the cases where a large valley separation has been used. Unlike in the two-valley models, while we see a velocity peak, we do not see a NM occupancy peak as we would expect, due to there being no higher-energy state or valley for the electrons to enter, with the maximum occupancy (and steady state occupancy) of NM states in the system reaching 67%. This system also reaches equilibrium much faster than the two-valley models, steady-state conditions being achieved in a little under 200 fs, a trait that was also present in the mid-field characteristics.

5.4. Summary

In this chapter, we have explored the steady-state and transient properties of Gallium Nitride by using the novel cosine band-structure approximation. We opened

the chapter by solely focussing on the effect on the steady state characteristics of GaN by changing the energy separation between to lowest two energy minima in the conduction band, as there is a wide range of values suggested in the literature ($1.1 - 2.1\,\text{eV}$) [6, 18, 56, 94]. It was shown that changing this valley separation has no effect on the low-field (first $100\,\text{kV/cm}$) transport characteristics of the material, nor did it have an effect on the shape of the characteristic. It did, however, have a profound effect on the characteristics in the mid-field, one of the most noticeable effects on the characteristics was on the value of the peak velocity, and the critical field at which it occurs, with lower valley separations suggesting lower peak velocities with lower critical fields. This variation in the peak velocities and their respective critical fields could be useful in determining the valley separation of the system, through comparison of experimentally obtained data with theoretical calculations.

The chapter continued by discussing the effect of negative effective mass states within the Γ valley and the relative contributions from these states when the valley separation is set to $1.2\,\text{eV}$ and $1.9\,\text{eV}$, and also the potential maximum effect of the NM states when electrons are unable to transfer into an upper valley. In the steady state regime, the effect of NM states was found to be dominated by the TE effect, however, it was found that the NM states have a noticeable effect on the transient properties of the system when the valley separation is large, with comparable transport characteristics to those suggested by the one valley model for the first few hundred femtoseconds of transport. If, like recent work by Semenenko *et al.* [94] suggests, that the valley separation between the two lowest conduction band energies is small, the work presented here suggest that NM states play a negligible role in all characteristics, and there is very little scope, if any, to potentially exploit

these characteristics in device development. However, if it is found that the valley separation is large, then in the transient regime there is potential for exploitation where the system characteristics are dictated by the shape of the Γ valley, and in particular, the NM states.

Chapter 6
Gallium Nitride 1D Device

Whilst it is of value to know the transport properties of bulk GaN, it is useful to know how it operates in a device. There is much interest in the development of devices based on GaN, such as in the creation of FETs and Gunn diodes [36, 42, 58, 79, 98]. There has been much relatively recent work looking into to simulate GaN based-devices using **k.p** based approaches [45, 56, 99] and full band approaches [100]. However, as has been discussed previously, the **k.p** model does not model the inflection point in the actual band-structure of GaN and thus ignores the effect of negative effective mass states. On the other hand full band approaches, whilst accurate, can take large amounts of time to run. We therefore propose the use of the cosine band-structure, which we successfully demonstrated to provide more accurate characteristics for GaN than the **k.p** model, in a device based setting.

In this chapter, we concentrate on the simulation of one-dimensional n-i-n diode simulations, based on the ensemble bulk simulations that were in the previous chapter. We use the same material parameters for GaN, in keeping with the recent data by Semenenko *et al.* [94], we assume a inter-valley separation of 1.2 eV, we do not consider other valley separations, nor do we consider the "one-valley" scenario. Again, polar-optical, equivalent- and inter-valley non-polar optical, piezoelectric and acoustic phonon scattering are all considered, as well as charged impurity scattering. We assume for all simulations that our device has an anode and cathode (with dopant densities of $10^{24}\,\mathrm{m}^{-3}$) of 150 nm each, whilst the intrinsic active region in the centre is of length 50 nm (giving a total device length of 350 nm). This device is simulated using a coupled Poisson - Ensemble Monte Carlo solver, as described in section 2.5 for a simulation time of4 ps.

6.1. Mesh Spacing and Time Step Selection

In order to determine a suitable mesh spacing and time step, we must use a set of stability criteria as described in section 2.5.2. Using equation 2.5.1, we can determine the plasma frequency of the system, in order to determine the maximum time step of the system [25],

$$\omega_p = \sqrt{\frac{e^2 n}{\epsilon_s m^*}} = \sqrt{\frac{(1.6 \times 10^{-19})^2 \times 10^{24}}{8.9 \times 8.85 \times 10^{-12} \times 0.2 \times 9.1 \times 10^{-31}}} \approx 4.23 \times 10^{13} \text{Hz}. \quad (6.1.1)$$

As the time step can be no larger than $1/\omega_p$, we find that the largest time step that can be used for these simulations is approximately 23.7 fs. Similarly, for the grid spacing, the mesh spacing must be no larger the Debye length of the system, so from equation 2.2.18 [25],

$$q_D = \sqrt{\frac{\epsilon_s k_B T}{e^2 n}} = \sqrt{\frac{8.9 \times 8.85 \times 10^{-12} \times 1.38 \times 10^{-23} \times 300}{(1.6 \times 10^{-19})^2 \times 10^{24}}} \approx 3.57 \times 10^{-9} \text{m}. \quad (6.1.2)$$

Whilst this is the maximum step length permitted, in the case of thus simulations, having such a large cell length when compared with the length of the active region will result in a very coarse potential profile (with a grid spacing of 3 nm, there would only be 16 grid points in the active region) and therefore may be unable to provide detailed enough characteristics of the model. Therefore, a smaller grid spacing is chosen, selecting 0.2 nm (2Å), which allows for a finer resolution with 250 cells within the active region. By choosing this step length, however, we must choose an appropriate time step so that particles cannot cross more than one cell boundary in a single step, through the use of equation 2.5.2 to do so. Setting the

maximum velocity to $E_B a/(2\hbar) \approx 1.062 \times 10^6\,\mathrm{m/s}$, we find [25],

$$\Delta x > v_{max} \times \Delta t \implies 0.2 \times 10^{-9} > 1.062 \times 10^6 \times \Delta t \implies \Delta t < 1.88 \times 10^{-16} s. \tag{6.1.3}$$

Thus, we choose a slightly smaller time step of 0.1 fs for these simulations, so that any calculations involving time are made simpler through the use of a round number.

6.2. Whole-system and active-region characteristics

As we have now described our system and determined what the stability criteria for our system is, we can proceed to analyse the results from said description. We start by looking at average characteristics of the system as a whole and the active region as the potential across the system changes at temperatures of $300K$.

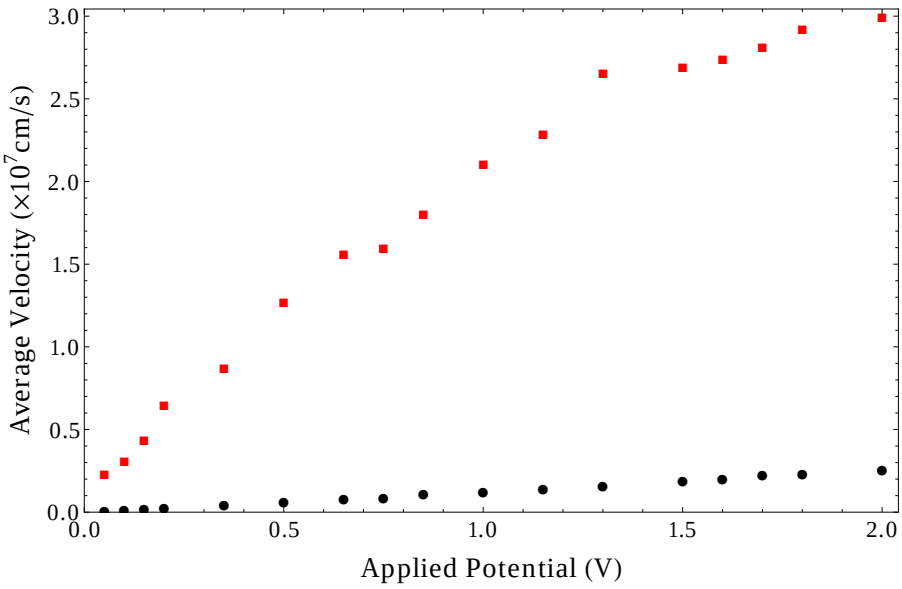

Figure 6.1) Average velocity of the particles in the whole device (black) and just the active region (red) as a function of the applied potential (using the device code with the cosine approximation).

Figure 6.1 displays the average velocity characteristics across the entire device and the active region. Across the whole device, particle velocities on average remain small even as larger potentials are applied across the device, with an average velocity of 0.257×10^7 cm/s being recorded at an applied potential of 2 V. We also see a linear trend in the relationship between the applied potential and the average velocity across the whole device. However, by just taking the average velocity across the active region, we find that the particles are travelling much faster, as we would expect, because it is assumed that there are no charged impurities in the active region. Indeed, we see that at an applied potential of 2 V, the average velocity of an active region particle reaches 2.994×10^7 cm/s. Unlike the whole device average, however, we do not see a linear relationship between the potential and the velocity, with there being less of a change in the velocity when higher potentials are reached. This can be explained for two reasons, 1) some electrons are able to transfer into upper valleys at higher applied potentials, and therefore fields, and 2) the shape of the band-structure approximation that we use and the potential transition of some particles to negative effective-mass states, thus decreasing the average velocity of this region.

The average energy characteristics of the device are shown in figure 6.2. In both the whole system and the active region cases, we see that the average energy increases as the potential increases, though we see that in the active region, the average energy of the particles is much higher than the average for the whole device for each applied potential, much like in the velocity characteristics. Both characteristics have a similar trend, at higher potentials, a small change in potential suggests a bigger increase in average energy than would be found for an identical change at lower potentials.

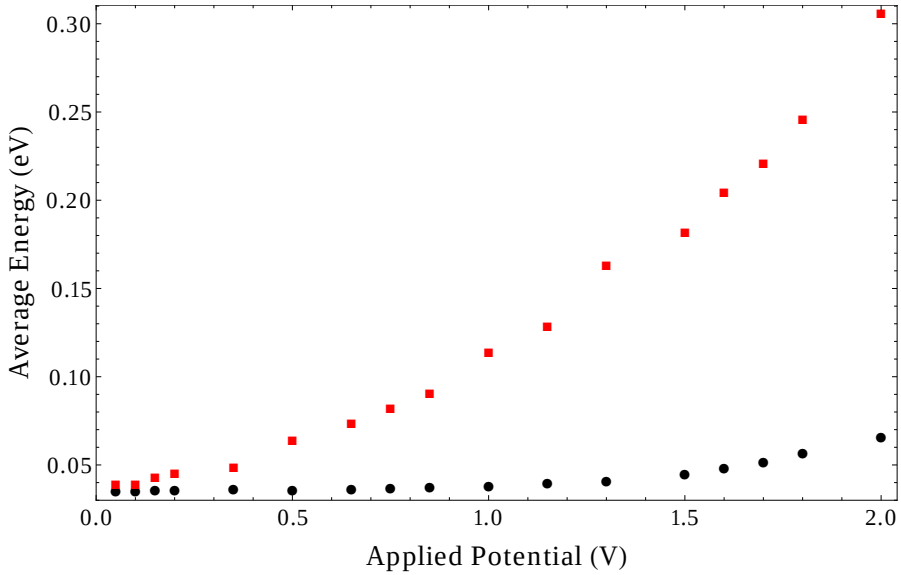

Figure 6.2) Average energy of the particles in the whole device (black) and just the active region (red) as a function of the applied potential (using the device code with the cosine approximation).

The large discrepancy that we can see between the whole system and the active region characteristics is explainable by noting that the active region contains approximately 1% of the particles in the simulation, for example, when 2 V is applied across the device, 1850 particles are in the active region, as opposed to 149265 in the entire simulation, which leads us to the belief that the whole system characteristics are dominated by the particles in the anode and cathode. Thus, to get a better idea of what is occurring in the device, we must turn to looking at characteristics at particular points in the device, rather than averaging over the device or parts of the device as a whole.

6.3. Position-averaged characteristics

We now consider the positional characteristics of the device, that is, the characteristics of the device in each 2Å cell, in order to be able to build up a picture of what is happening in different regions of the device. All of the following charac-

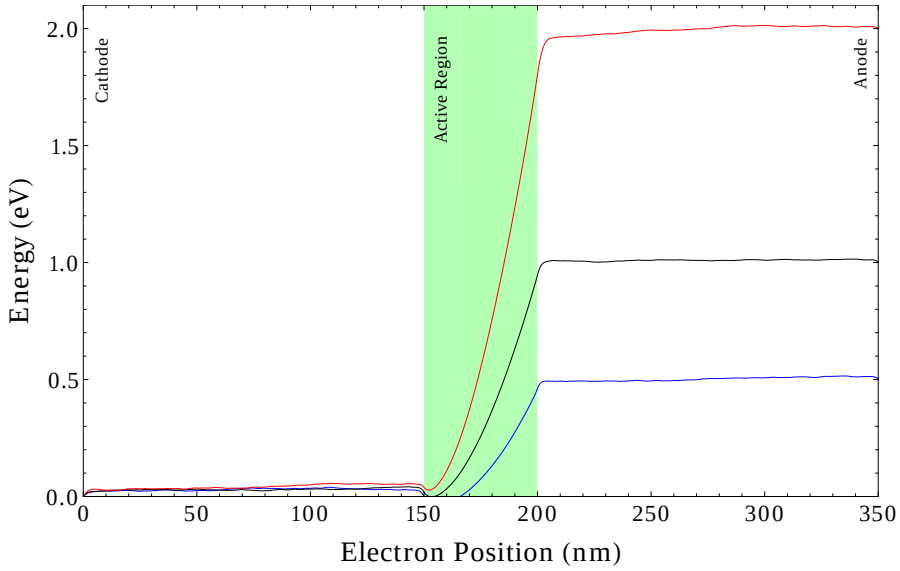

Figure 6.3) Potential profile across the device when the applied potential across the device is 0.5 V (blue line), 1 V (black) and 2 V (red) using the device code with the cosine approximation.

teristics (bar the potential profiles shown in figure 6.3) are obtained by averaging the properties of the particles in each cell. We present these position-averaged characteristics where a potential of 0.5 V, 1 V and 2 V is applied across the device, roughly corresponding to field strengths of 100 kV/cm, 200 kV/cm and 400 kV/cm across the active region.

Figure 6.3 displays the potential characteristics across the device, whilst Figure 6.4 depicts the velocity and energy position averaged profiles. The first thing we note is that due to the strong impurity scattering in the anode and cathode of the devices, the average electron velocities and energies in these areas correspond to thermal energies, with average energies of about 0.03 eV, approximately $1.5k_BT$ at 300 K, being recorded. This is unsurprising, as when we look at the potential (and thus, the field) characteristics, we find that the change in potential is negligible across the entire region. A small change in potential indicates a small field, and thus, electrons do not gain much energy and momentum between each scattering event, such that electron scattering, particularly impurity scattering and polar

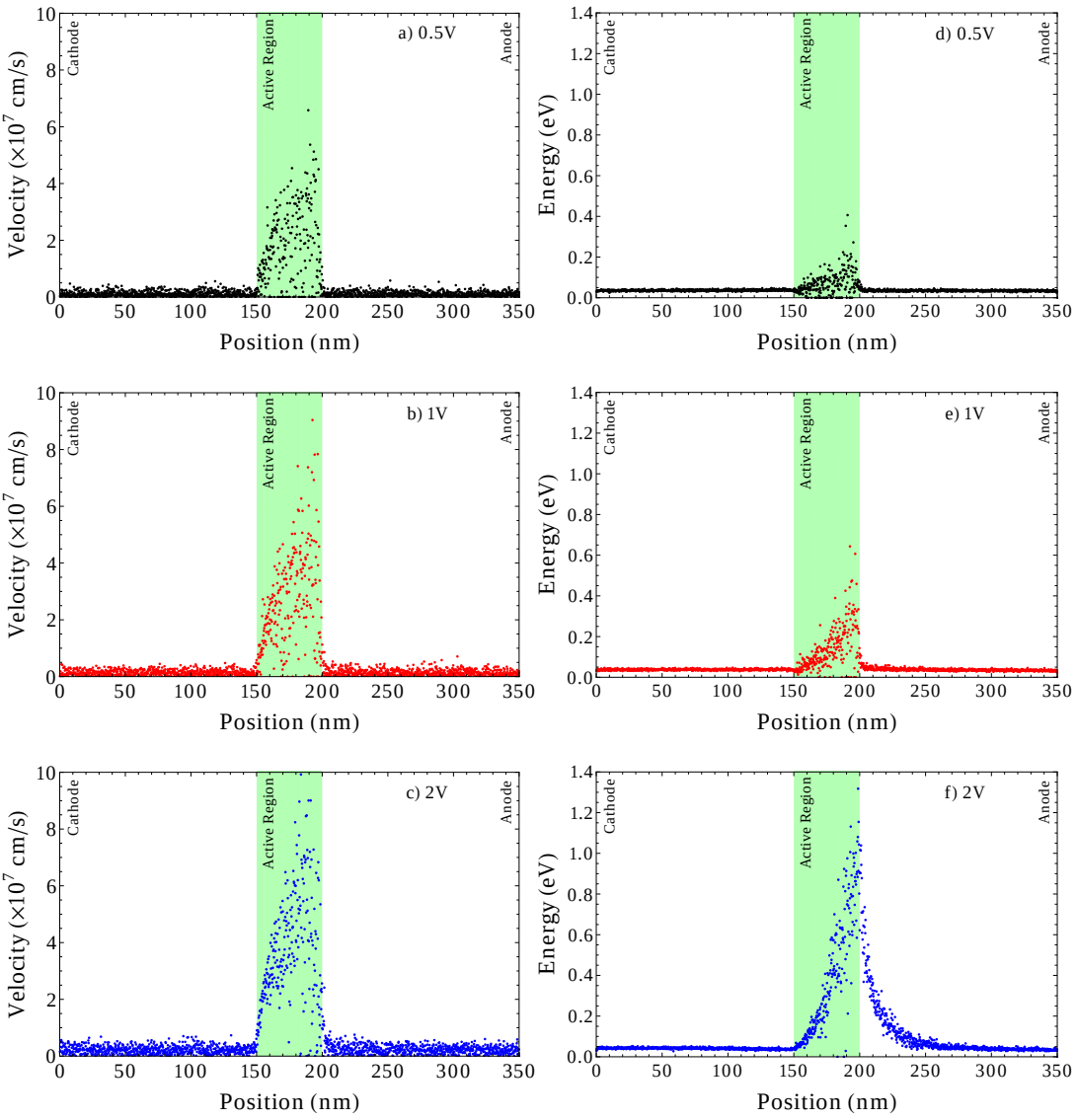

Figure 6.4) Velocity-position averaged (left) and energy-position averaged (right) profiles when potentials of 0.5 V (black, top), 1 V (red, middle) and 2 V (blue, bottom) are applied across the device. Each point represents the average velocity or energy of the particles in each 2Å cell (using the device code with the cosine approximation).

optical phonon scattering by emission (at slightly larger energies), is able to inhibit energy and momentum gain through momentum redistribution, with the latter scattering mechanism being particularly good at reducing the energy of the system. In the active (intrinsic) region of the system, however, an increase in the average particle velocity is observed as the particles get closer to the anode. As can be seen from the potential characteristics, we can see that there is a large field that affects the active region. Particles therefore gain much more energy and momentum between scattering events than those in the doped anode and cathode regions, and are less likely to be back scattered due to the properties of the dominant polar-optical phonon scattering favouring scattering in the direction of momentum.

Focussing on the high field case, i.e. when a potential of 2 V is applied to the system (sub-figures 6.4c) and f)), we find that there is a region of about 50 nm in the anode adjacent to the active region where the average energy is larger than thermal energies. This can be attributed to particles that have been promoted to the upper valley entering the anode in that high energy, low velocity state. As the particles travel further from the active region-anode, we find that the average energy decreases until the thermalised region is reached. As the particles enter the anode, they suddenly encounter a much lower field, and thus gain less energy from drift in the field between scattering events than they did in the active region. Particles that have had their momentum redistributed and/or energy reduced through scattering events are unlikely to be able to recover any lost momentum (in the direction of the field) and energy between scattering events. This results in an overall decrease in particle energy as the particles move away from the active region, until particles are unable to lose energy directly from scattering (at less than one polar optical phonon energy, 92 meV).

The average velocity profile, on the other hand, reaches average thermal velocities over the much shorter distance of approximately 5 nm. This is due to the redistribution of particle momentum, as well as the large quantity of particles that were already in thermal equilibrium in the anode, whilst there are many high velocity, high energy particles in the system, the momentum of the particles are scattered in all directions very quickly upon entry into the anode, thus having little net effect on the average velocity in the direction of the potential, unlike the energy of the particles which encompasses all three directions due to it being a scalar quantity.

We now discuss the form of the potential profiles found in figure 6.3. At the cathode and anode, we find that the potential profile is fairly flat, plateauing around 0 V and the maximum potential, whilst in the active region, there is a large change in the potential, and thus a large field applied across it. This is unsurprising, as the second derivative of the potential is directly proportional to the charge density in a cell, as per equation (2.5.5) (assuming the mesh spacing remains constant). However, in the active region, close to the junction with the cathode, a numerical instability can be seen where a potential "dip" occurs, which is more prominent and may dip below 0 V when smaller potentials are applied across the system. This is due to the build-up in charge that occurs in the active region close to the cathode, causing the potential calculation to undershoot.

We can see this charge build-up in the active region by looking at the number density plot, as displayed in figure 6.5, which displays the number of particles in each grid point. In the first 5 nm of the active region, it can be seen that there is a larger density of particles than over the rest of the region. We see this because at this point in the device, the average velocity of the particles is low compared with later in the device (see figure 6.4), so particles on average spend longer in each

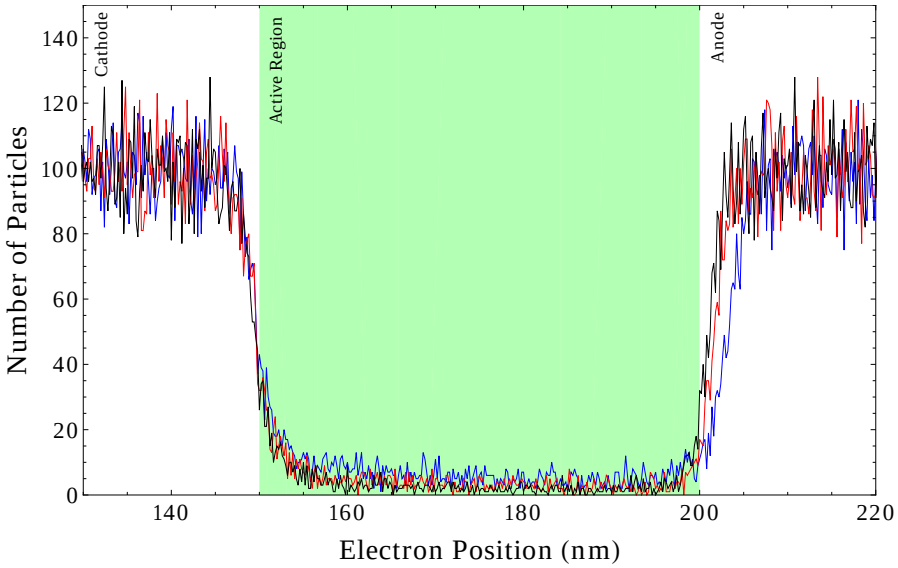

Figure 6.5) The number of electrons in each grid point across the active region and in the immediate area around it when a potential of 0.5 V (black), 1 V (red) and 2 V (blue) is applied across the device (using the device code with the cosine approximation).

cell. This is particularly prominent as the model suggests that there is actually a field in the opposite direction to the applied potential at the cathode-active region junction which acts to slow the particles down, though as previously explained, this is a numerical artefact. As the particles build up their velocity, they spend less time, on average, in each cell, and thus, a lesser number of particles can be seen in these cells further from the cathode.

In the anode, close to the junction with the active region, we see that there is a small region where the number density in the first $5 - 10$ nm is lower than the standard number density seen in the bulk of the anode. Most particles entering the anode from the active region do so with a much larger velocity the average anode electron, so, as explained in the previous paragraph, spend less time in these cells, and thus, there are a lesser number of particles in these high-speed cells. As the particle velocities reduce, we see that the number density of the particles further from the junction increases, before eventually reaching approximately 100 particles per cell. We note that it takes longer for particles to reach this point when a larger

potential is placed across the device, as particles reach larger velocities (as seen in figure 6.4) and thus take longer to shed their momentum, spending less time in the cells near the junction. This has an effect on the potential profiles as seen in figure 6.3, it can be seen that the high field areas finish a small distance into the anode rather than at the junction, extruding from the active region for the same distance as it takes for the number density to reach nominal values in the anode.

We can also see that this partial depletion of carriers also occurs in the cathode, close to the active region. Unlike in the anode, the number density profiles in the cathode is very similar across all potentials, which is unsurprising, given that the potential profiles are also very similar. This is due to thermal motion occurring in the cathode, so at most points in the cathode, there is an almost equal chance of a selecting a particle travelling in any direction in the device. However, as you approach the active region, particles that enter the active region are much more likely to continue travelling away from the cathode. Thus, particles that leave the cathode are less likely to be replaced, due to the particles only being replenished from one direction, as opposed to being replenished from both directions.

6.4. Energy & Phase-space characteristics

We now take a look at the steady-state characteristics of the system by looking at the individual super-particles in the system and plotting each super-particle's position against its velocity and energy. For these characteristics, we assume an applied potential of 2 V across the device.

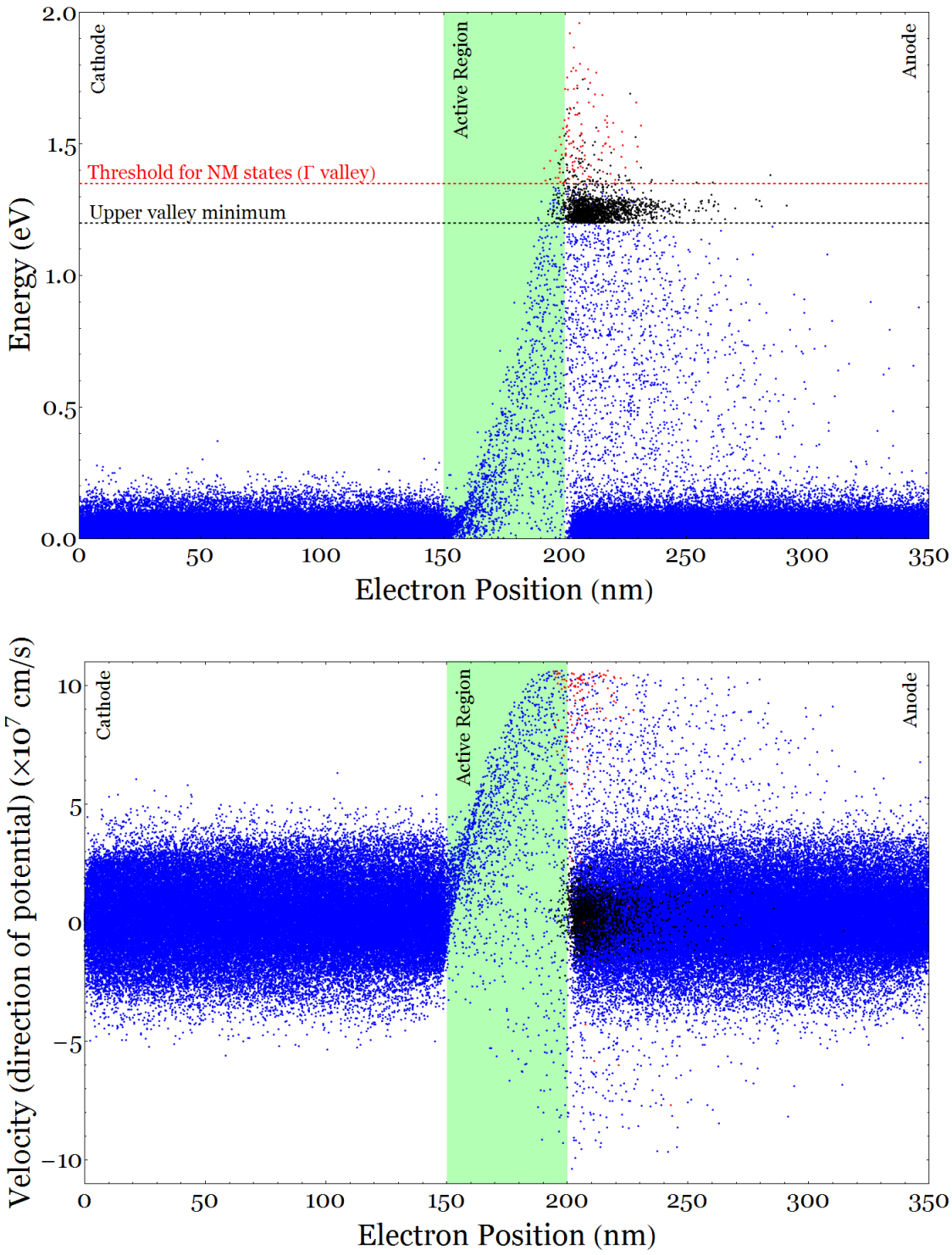

Figure 6.6) The energy-space (top) and phase-space (bottom) diagram of each super-particle, when 2 V is applied across the device at a temperature of 300 K (using the device code with the cosine approximation). Colours indicate positive (blue) and negative (red) effective mass states in the Γ valley and states in the upper valley (black).

6.4.1. Characteristics at 300K

Figure 6.6 plots the position in the direction of the applied potential of each super-particle in the device against their energies and velocities in the direction of the applied potential (i.e. the energy- and phase-space diagram). Focussing on the energy profile first, we can clearly see that the there is a small spread in the electron energies in the cathode. It was already known from figure 6.4f that the average energy per grid point is roughly $1.5k_BT$ (≈ 0.03eV), we can see that most electrons in the cathode have energies of less than 0.1 eV. The situation is, for the most part, similar in the anode in that most electrons have energies that are less than 0.1 eV. There are, however, a few electrons that have travelled through the active region that have larger energies. These traits are echoed in the phase-space plot, where we find that the velocity spread is relatively small, with most electrons travelling at low, thermal velocities in (or against) the direction of the applied potential.

We can investigate this further by looking at the distributions of the energy and the velocity in the cathode and anode, as can be seen in figure 6.7. Focusing on the energy distributions first, we find that the modal energy is actually at a lower energy than the average energy for the two regions, with a fairly broad "tail" of larger energies. Indeed, we see the formation of a "bump" in the two distributions, which is particularly prominent in the cathode at approximately 0.045 eV. We attribute this to electron back-scattering, whilst we measure velocity in the direction of the applied potential, energy, by it's very nature as a scalar, encompasses motion in all three directions. Turning our attention to the velocity distribution profiles, we see in both cases that the distributions resemble normal distributions that are centred at velocities at around 0.2×10^7 cm/s, with a slight skew towards positive velocities. This is viable, due to the small fields that occur across the two regions.

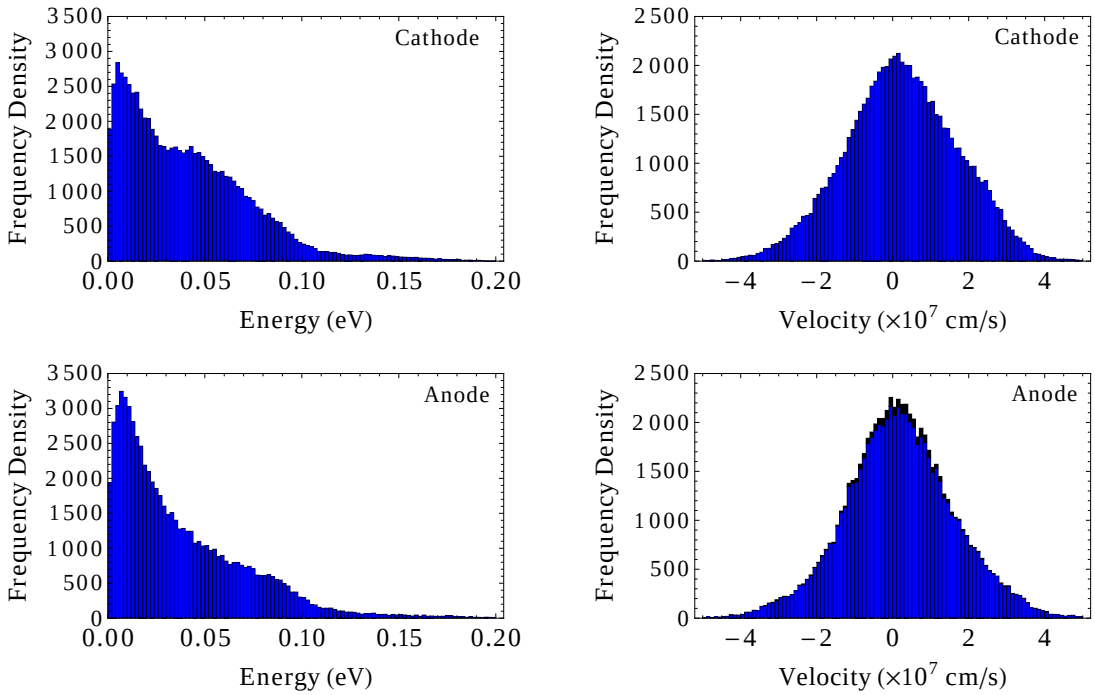

Figure 6.7) Distributions of electron energy (left) and velocity (right) in the direction of the applied potential in the contacts (using the device code with the cosine approximation). For the anode, full distributions are not shown as there are only negligible peaks beyond the displayed range. Blue -Γ valley particles in positive mass states, red - Γ valley, negative mass, black, upper valley.

We now look at the active region of the device. There is a stark contrast in the behaviour of the electrons between the cathode/anode and this region, unlike the cathode and anode, electrons can gain energy and momentum very quickly. Subfigures 6.4c) and f) have already shown that this is the case in the active region, but some interesting features can be seen in figure 6.6. First, looking at the energy profile in the active region, as particles move towards the anode, the largest energy attained by the particles increases. By looking at the relationship between this maximum with respect to the position, it can be seen that the shape this produces resembles that of the band-structure that we have used. This shape is actually more prominent in the velocity characteristics, where the maximum velocity curve can very clearly be seen, including the point where the maximum velocity of the particles begins to decrease due to the negative-effective mass states after 45 nm.

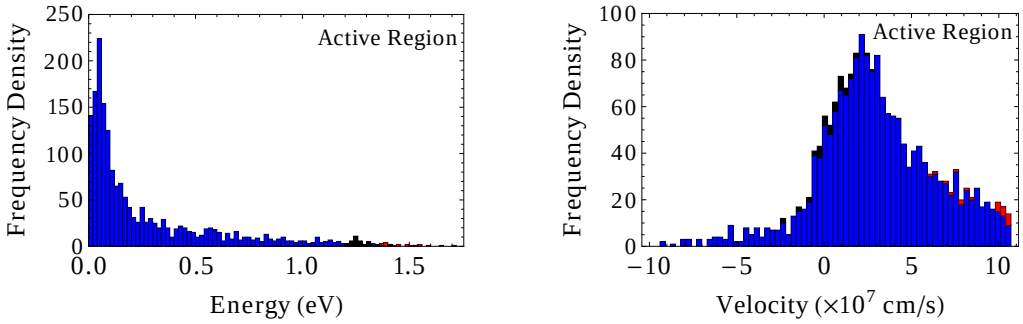

Figure 6.8) Distributions of electron energy (left) and velocity (right) in the direction of the applied potential in the Active Region (using the device code with the cosine approximation). Blue indicates Γ valley particles in positive mass states, red indicates Γ valley negative mass states and black indicates upper valley particles.

Turning to the energy and velocity distributions of the electrons in the active region (figure 6.8), we see that there is a shift to higher energies (0.1 eV peak energy as opposed to 0.015 eV) and velocities (2.25×10^7 cm/s instead of 0.2×10^7 cm/s) due to the increase in the electric field. In the energy distribution, we see a larger tail than seen in the anode and cathode, with a very slight energy peak occurring at the upper valley minima (located at 1.2 eV). We also do not see a bump in the distribution, as the little back-scattering that does occur in the active region is completely occluded by the relatively large increases in energy that electron drift in the field provides. The velocity distribution shows that the bulk of the particles in the active region move towards the anode at any given time, with a distribution highly biased towards velocities in the direction of the applied potential. Interestingly, we don't see many particles reach negative effective mass states or the upper valley region, this is due to the chosen length of the active region, electrons are only just reaching the threshold energies for transfer into either of these states before entering the anode.

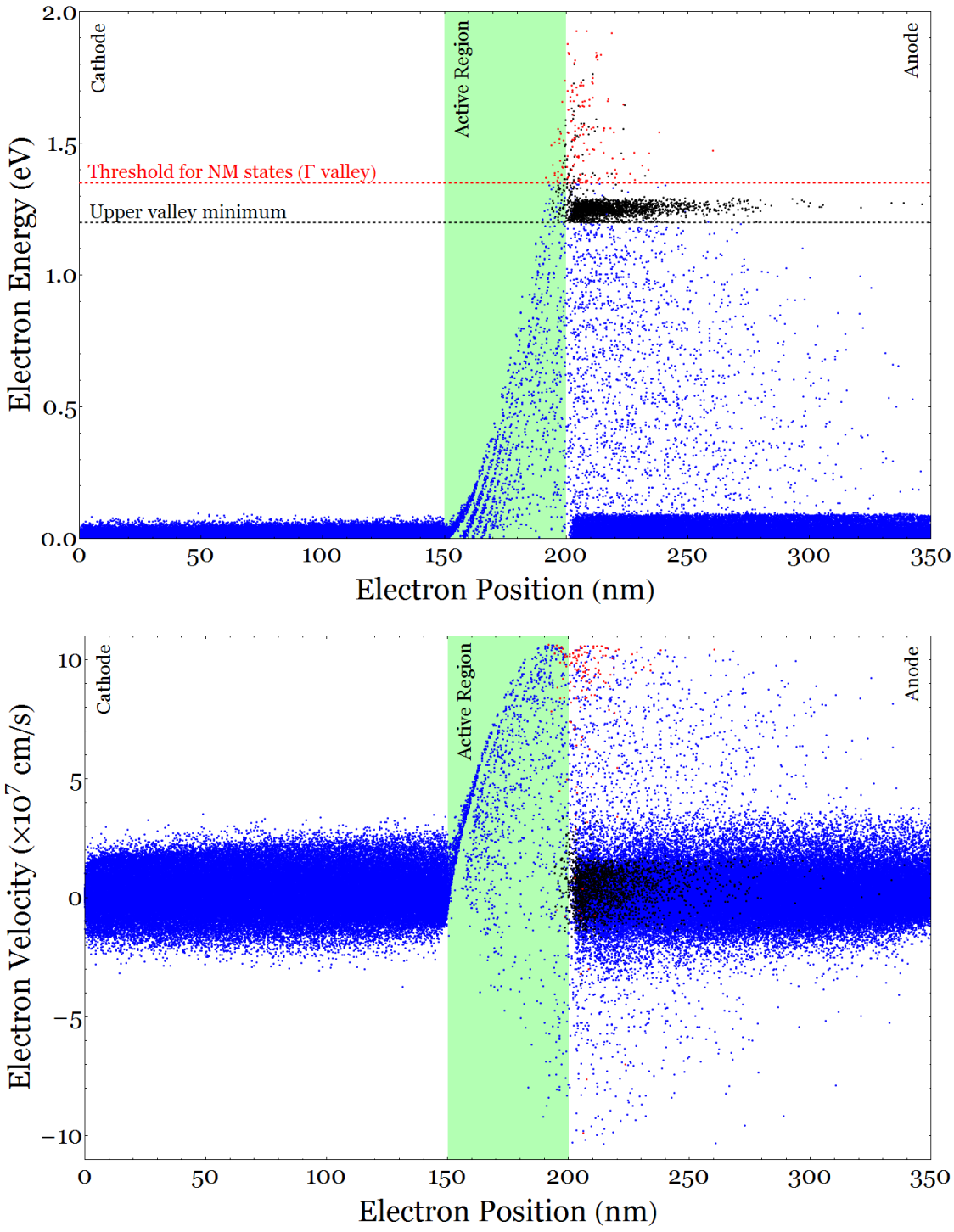

Figure 6.9) The energy-space (top) and phase-space (bottom) of each super-particle in the system against their position in the device, when 2 V is applied across the device at a temperature of 77K (using the device code with the cosine approximation). Colours indicate positive (blue) and negative (red) effective mass states in the Γ valley and states in the upper valley (black).

6.4.2. Characteristics at 77K

We now take a look at the same system at 77 K. In doing so, we only reduce the temperature parameter, we do not modify of any of the band parameters so that they truly reflect the band structure at this temperature. Obtaining these parameters would only provide a benefit if we were interested in pursuing running devices such as these at these temperatures. The reason for decreasing the temperature of the system is to inhibit some of the scattering mechanisms so that we can clearly see patterns in the energy and phase space plots, as illustrated in figure 6.9.

We can see an effect which is more prominent towards the cathode, where distinct lines of electron energies vs. their positions can be seen. The energy separation between these lines can be measured to be the energy of one polar optical phonon (POP), confirming that POP is the dominant scattering mechanism in the active region, due to this, we term this effect "phonon striping". Looking at the active region, distinctive lines can be seen at low energies near the junction of the cathode, these lines are the phonon striping lines due to the huge dominance of the POP scattering mechanism at 77 K. Indeed, these phonon striping characteristics can be seen throughout the active region and into the anode. While other scattering mechanisms do have enough of an effect to make these less clear by the time the particles reach the anode, the lines in the anode do not change in energy with position, unlike the striping in the active region, due to the lack of a local field. Thus, as POP is the dominant scattering mechanism for high energies, we see that these phonon striping lines are spaced one polar optical phonon energy apart. This effect is also visible when the lattice temperature is set to 300 K (refer back to figure 6.6), whilst the lines are definable, other scattering processes have enough of an effect to make these lines less clear, so whilst we see electrons tending to form

these lines, some electrons do get scattered into other energy states.

These characteristics also appear in the phase-space characteristics, again, in the active region, the phonon striping effect can be seen, though less so than in the energy-space plot as the velocity measured in our case is in the direction of the applied potential, and as the energy of the particles can be distributed in three dimensions without restriction, a high energy particle may have zero velocity in the direction we are interested in. Interestingly, we see the shape of the band-structure much more clearly when we look at this lower temperature system, suggesting the maximum velocity of the particles are being reached after 41 nm into the device, before the electrons start to lose momentum as a result of the band-structure.

6.5. Summary

Throughout the chapter, we have investigated the properties of a one-dimensional n-i-n device using the cosine band-structure approximation. We started by discussing whole system and active region average velocities and energies, finding that as about 99% of the particles in the device are in the anode and cathode at any one time, these characteristics are of little use in describing the processes that occur in the device. Thus, we continued the chapter by looking at position-averaged characteristics, and found distinct differences in the properties of the active region, when compared with the anode and cathode. It was found that particles in the anode and cathode mostly follow a thermal regime, as we found the potential across the anode and cathode varied very little, and thus the field across these regions was negligible. On the other hand, however, a large potential difference arose across the active region, and particles in this region were able to reach energies large enough

to be able to transfer into the upper valleys and negative mass states in the space of $45 - 50\,\text{nm}$. We were also able to spot the occurrence of charge build-up at the junction of the cathode and the lack of particles in the anode at the junction with the active region.

We finally looked at energy-space and phase-space plots of the device, and distributions of the particles in the various regions. We were able to confirm that the distribution particles in the anode and cathode indeed had similar profiles to those of a thermal distribution. In the active region, we noticed some interesting patterns emerging, including the onset of phonon-striping and the effect of the band-structure on the shape of the energy-space and phase-space plots. Whilst we did have issues with this simulation, such as the issue with the potential calculations, we have been able to demonstrate some of the other characteristics that occur within the device, and that this system works as a proof-of-concept. This method will therefore serve as a very good base for future works, such as the expansion of the system to a two- or three-dimensional device.

Chapter 7
Dilute Gallium Nitrogen Arsenide

In the previous chapters, we have concentrated our efforts on binary compounds, GaAs, InP and ZnO for algorithm validation in chapter 4, and then GaN, which has been the focus of the work in chapters 5 and 6. We now look at a ternary compound, Gallium Nitrogen Arsenide (GaN_xAs_{1-x}). In particular, we look at the material in the dilute nitride case, where the nitrogen concentration is less than 2%. In the dilute nitride cases, GaN_xAs_{1-x} is thought to have similar properties to GaAs, with the addition resonant energy levels due to the added nitrogen states. Many models have been developed in order to attempt to determine the characteristics of the material. One of the more well known approaches that have been used to model dilute GaN_xAs_{1-x} is through the introduction of a new nitrogen scattering mechanism into the standard GaAs model, which is a mechanism localised around the resonant energy levels caused by the addition of nitrogen impurities into the system [11, 24, 69, 70, 101, 102]. The approach assumes that the nitrogen states has no effect on the host band-structure, or any of the other material parameters, and thus, this mechanism models the dispersive nature of the strong nitrogen resonance. Alternatively, another popular model that is often used is the band anti-crossing (BAC) model [66, 103, 104], which assumes that the band-structure of GaN_xAs_{1-x} is altered due to optical bowing in the lowest (Γ) valley, splitting it into two or three separate bands, dependant on the concentration of nitrogen impurities and the position of the various states that are possible. The BAC model is therefore is primarily concerned with the distortive effect that the injection of nitrogen has on the band-structure of the host material.

In this chapter, we analyse the properties of GaN_xAs_{1-x} broadly using these two

approaches with our ensemble Monte-Carlo algorithms, and attempt to determine the relative effects of the dispersive and distortive properties of the material. We begin this chapter describing these models that we use in order to simulate the addition of these resonant energy levels. We then move on to look at the characteristics of bulk GaN_xAs_{1-x} as suggested by these models, first in the steady state regime before analysing the transient properties of the material, before drawing conclusions and potential expansions to this study at the end of this chapter.

7.1. Description of Models

Whilst the two models that we are considering in this chapter deal with the resonance effect caused by the nitrogen states in very different ways, there are many similarities between them. In both of the models, it is assumed that the system has identical parameters to those of a bulk GaAs system, (see table 7.1 for these values), and scattering due to phonons and charged impurities are treated in accordance with the applicable band-structure, in particular, polar optical phonon (POP), piezoelectric (PZ), optical deformation potential (ODP), acoustic deformation potential (ADP) and charged impurity scattering mechanisms are considered. We assume that the upper L-valleys in the band structure are completely unaffected by the nitrogen resonance and are thus identical to those found in bulk GaAs, and that scattering to this valley occurs through ODP scattering.

We use our Ensemble Monte-Carlo (EMC) methods in all simulations, employing the use of 15000 particles and simulating the transport over a period of 4ps.

Table 7.1) GaAs parameters as used in the nitrogen scattering model for GaN_xAs_{1-x} at room temperature (300K). Parameters have been taken from INSPEC [31], Blakemore [74], Madelung *et al.* [89]

Parameter (units)	GaN_xAs_{1-x}
Density (kg/m^3)	5360
Longitudinal sound velocity (ms^{-1})	5240
Transverse sound velocity, (ms^{-1})	2480
Non-polar optical deformation potential coupling constant, (eV/m)	10^{11}
Inter-valley scattering coupling constant, (eV/m)	10^{11}
Acoustic deformation potential, (eV)	7
Piezoelectric constant e_{14} (C m^{-2})	-0.16
Energy gap (eV)	1.424
Static dielectric constant (ϵ_0)	12.9
High-frequency dielectric constant (ϵ_0)	10.92
Energy gap (between Γ_1 and satellite valley minima) (eV)	0.29
Number of equivalent satellite upper valleys	4
Effective mass, Γ_1 minima (m_e)	0.067
Effective mass, satellite upper valley minima (m_e)	0.35
Polar optical phonon energy (meV)	35.36
Non-polar optical phonon energy (equivalent valleys) (meV)	27.8
Non-polar optical phonon energy (inter-valley) (meV)	34.3
Impurity concentration (cm^{-3})	10^{17}

7.1.1. Nitrogen scattering model

Our first model accounts for the inclusion of nitrogen states by assuming that they add a new scattering mechanism which is strongest around the energy levels of the states. It is assumed that this does not affect the band-structure of GaAs, thus this model can be thought of simply as GaAs with extra scattering mechanisms, as illustrated in Figure 7.1. We only consider nitrogen singlet and pair states in

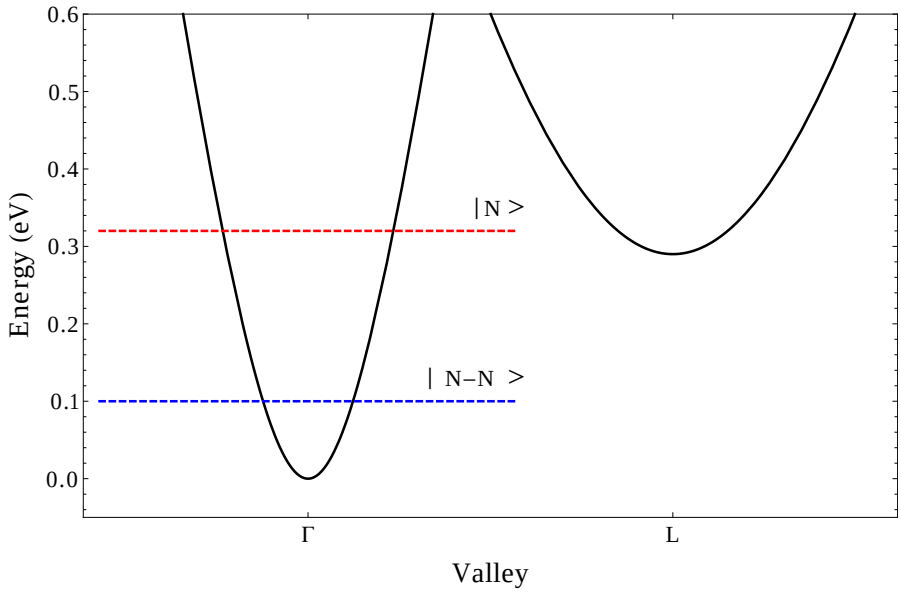

Figure 7.1) Schematic of the band-structure used in the nitrogen scattering model. The red and blue dashed lines indicate where the energy position of the nitrogen singlet ($|N\rangle$) and doublet ($|N-N\rangle$) states.

this model, the contribution of any higher order states (such as triplet states) are assumed to be negligible and hence ignored. Nitrogen impurity concentrations of 0.1%, 0.36%, 0.5%, 1.2% and 2.0% are considered using this model.

To be able to accommodate this model into our algorithm, we require an analytic approximation for the nitrogen scattering. To do this, we start with a previously derived expression for nitrogen scattering, [101, 102]

$$W_N(E_{\mathbf{k}}) = \sum_i \frac{\pi\alpha^3}{2\hbar} \frac{\beta_i^4 x_i}{(E_{\mathbf{k}} - E_{N_i})^2 + \Delta_{N_i}^2} N(E_{\mathbf{k}}), \tag{7.1.1}$$

where α is the lattice constant, $N(E)$ is the density of states at a given energy E, and for a given nitrogen state i, β_i is the coupling parameter, x_i is the concentration of nitrogen states, E_{N_i} is its resonant energy and Δ_N is its energy broadening. This rate is summed over all potential nitrogen states. The parameters β_i, x_i and Δ_{N_i} have been determined by fitting these parameters so that the characteristics of the scattering rates match those obtained through the use of the Linear Combination

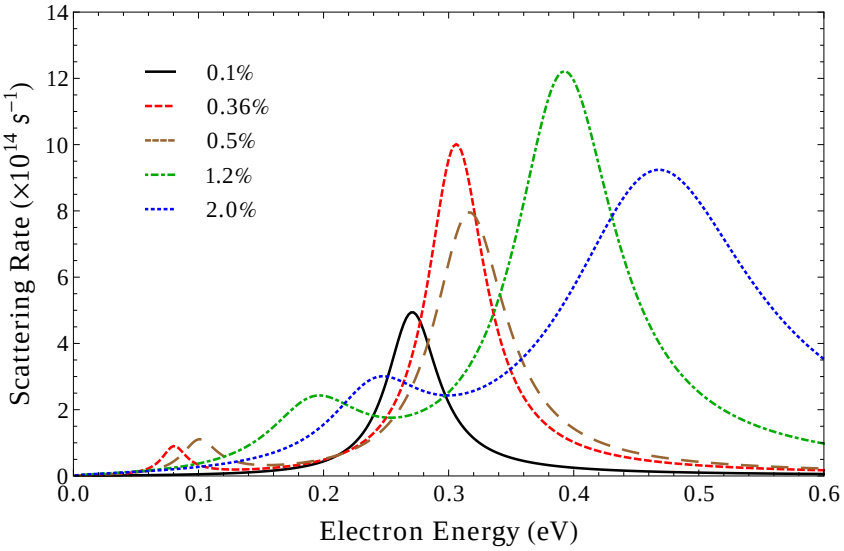

Figure 7.2) The nitrogen scattering rate as a function of energy as used in the first model at nitrogen concentrations of 0.1% (black, solid), 0.36% (red, short dashed), 0.5% (brown, long dashed), 1.2% (green, dot-dashed) and 2.0% (blue, dotted). The energy is relative to the energy minima of the conduction band at the Γ point, E_c. These scattering rates are based on those by Fahy *et al.* [101] (figure 2), though are not identical to them.

of Isolated Nitrogen States (LCINS) model from Fahy *et al.* [101], and thus, from this we are able to obtain analytic scattering rates for the various concentrations of nitrogen in GaN_xAs_{1-x} for use in our simulations. For simplicity, we assume that nitrogen scattering is elastic and isotropic. The fitted rates are illustrated in figure 7.2.

7.1.2. Analytic approximation of the E_- band

The second model we consider is based on the band anti-crossing (BAC) model, where the nitrogen scattering is accounted for by splitting the Γ-valley into two "mixed state" bands, a lower (E_-) and an upper (E_+) band. In our model, we only consider the contribution of the E_- band, and we assume that the L-valley is identical to that found in GaAs. This means that we do not consider the effect of the E_+ band, nor do we consider any broadening of the band structure induced by the nitrogen impurities as suggested by Green's function approaches [20]. Figure

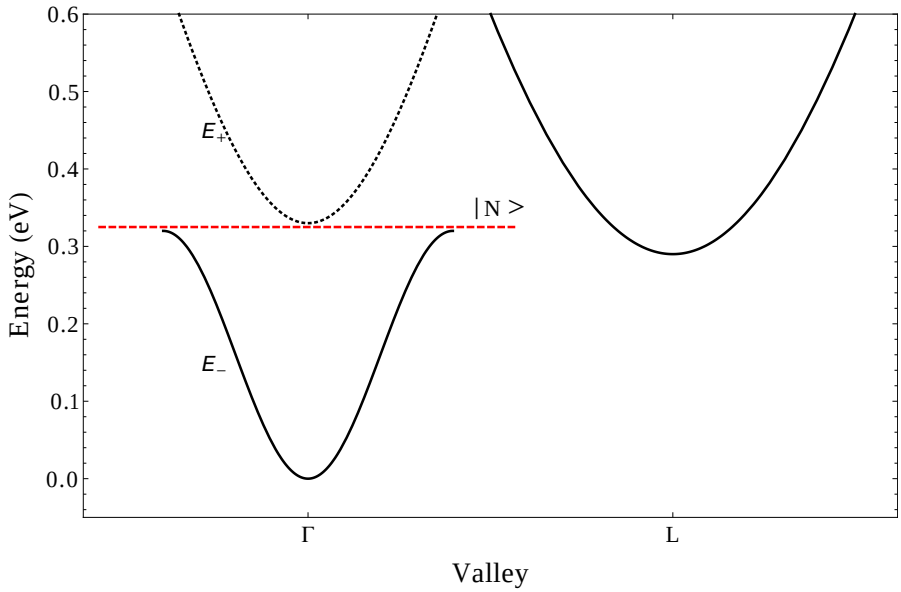

Figure 7.3) Schematic of the band-structure when modelling an analytic approximation of the E_- band when the nitrogen concentration is 1.2%. The red dashed line indicates the energy the nitrogen singlet state ($|N\rangle$) resides at. The E_+ band (dashed) is included in the diagram for completeness, however, it is not simulated in this model.

7.3 illustrates the band-structure used in this model.

The E_- band in the model is based on the cosine approximation as first discussed in chapter 3, with slight modification, and takes the form,

$$E_-(k) = \frac{E_B}{2}(1 - \cos[\gamma k \alpha]), \tag{7.1.2}$$

where E_B is the width of the E_- band, γ is a scaling constant, dependent on the nitrogen concentration, k is the wave-vector of the electron and α is the lattice constant. For sub-1% nitrogen concentrations, the E_- band cannot be satisfactorily modelled using this approximation. Indeed, in the sub-1% cases, we actually find that the **k.p** model for the band structure is an excellent approximation for the band structure that exists right to the top of the E_- band, where the inflection point is, only requiring special numerical treatment for a very small range of energies, as has been previously suggested [11]. For a nitrogen concentration of 1.2%, however, we find that our cosine-based approximation is much better fit to the E_- band

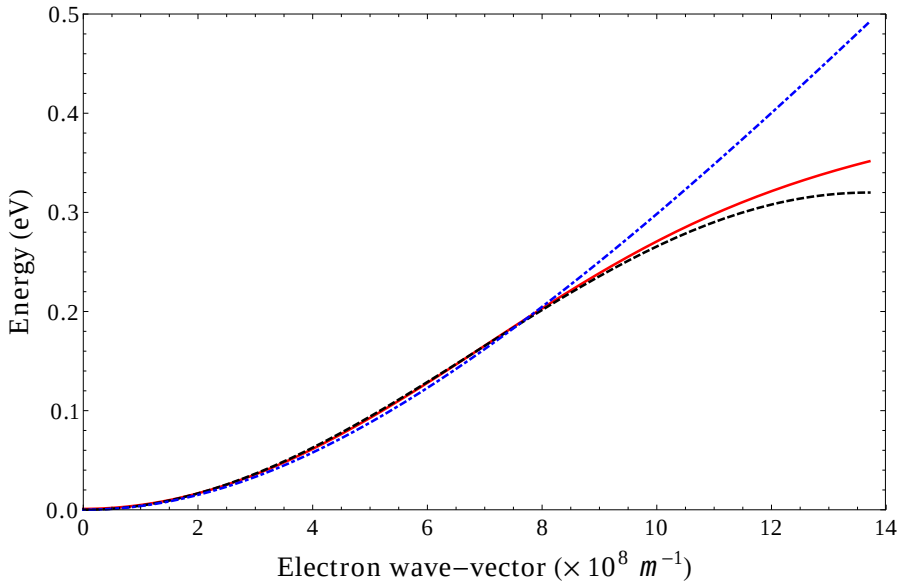

Figure 7.4) A comparison between the BAC model E_- band when the concentration of N impurities is 1.2% (red, solid line), the **k.p** approximation (blue, dot-dashed line) and the cosine approximation (black, dashed line)

around the Γ point when $E_B = 0.32\,\text{eV}$ and $\gamma = 4$ than the **k.p** approximation, as shown in figure 7.4, and is a fairly good fit when the concentration is 2%. We only consider a N concentration of 1.2% for use with this model. Scattering rates for the E_- band are similar to those that have been derived in chapter 3, with the substitution of $a = \gamma\alpha$. Nitrogen scattering is not considered as part of this model, as it is assumed that the altered dispersion of the band solely and adequately accounts for the effect of the introduction of the nitrogen states.

7.2. Steady State Characteristics

7.2.1. Nitrogen scattering Model

Figure 7.5 shows the velocity-field characteristics of GaN_xAs_{1-x} that were generated using the model that includes nitrogen scattering, in comparison to bulk GaAs. We find that at 0.1% N concentration, the peak velocity, $v_{max} = 1.15 \times 10^7\,\text{cm/s}$ at $8.5\,\text{kV/cm}$, which is a significantly lower velocity with a higher critical field than is

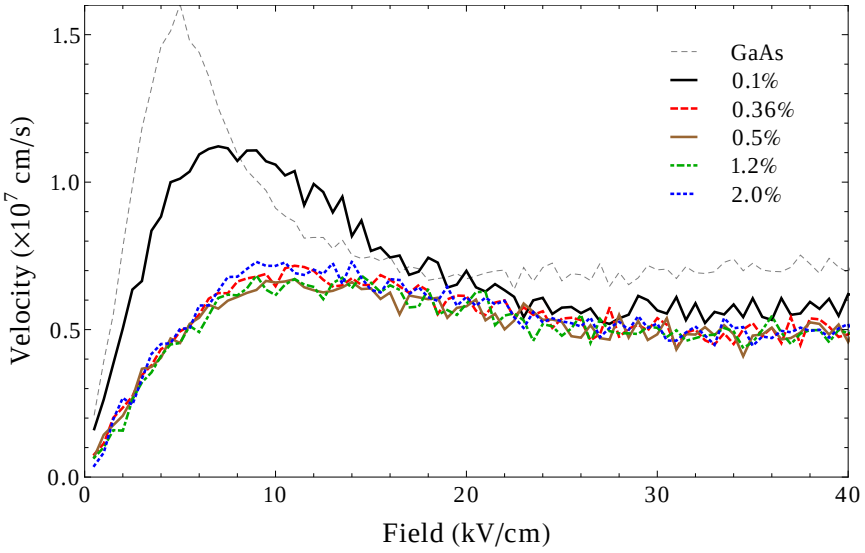

Figure 7.5) Velocity field characteristics of GaN_xAs_{1-x} for various concentrations of nitrogen (see legend) determined using the nitrogen scattering method, with the EMC code and the **k.p** approximation.

found in pure GaAs. There is still a sizeable negative differential velocity (NDV) that occurs, though it is less severe than that found in GaAs. At nitrogen concentrations of 0.36% and higher, we find that the characteristics are broadly similar to each other, suggesting electron peak velocities of between 0.6 - 0.7×10^7 cm/s, which occurs at a critical field of around 12 kV/cm. While there is still a noticeable NDV in the velocity field characteristics at these higher nitrogen concentrations, it is found that they are largely dampened, as the nitrogen scattering is massively dominant and eclipses the inter-valley (IV) scattering rate at fields at which the nitrogen scattering operates, at it's maximum point, the nitrogen scattering rate is approximately three orders of magnitude greater than the IV scattering rate.

It is thus unsurprising that the electron mobility-field characteristics, as illustrated in figure 7.6, show similar trends in the characteristics. We find that there is a noticeable decrease in the low-field electron mobility as nitrogen is introduced, but, as with the velocity-field characteristics, the mobility characteristics for nitrogen concentrations greater than 0.36% are very similar to each other. The inset

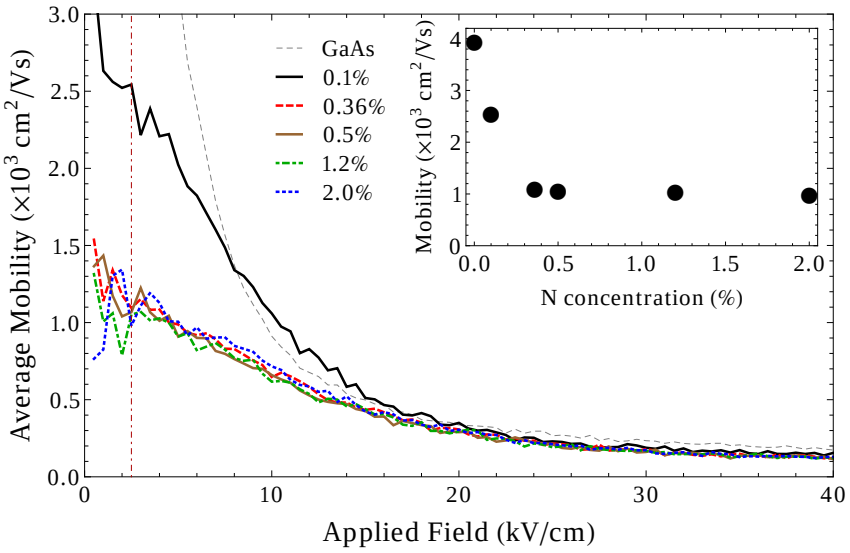

Figure 7.6) Electron mobility-field characteristics of dilute GaN_xAs_{1-x} when using the nitrogen scattering model, with the EMC code and the **k.p** approximation. Inset: low-field (2.5 kV/cm, denoted by the dark-red vertical line on the main figure) electron mobility as a function of nitrogen concentration.

in figure 7.6 displays the electron mobility at 2.5 kV/cm as a function of nitrogen concentration. At nitrogen concentrations $\geq 0.36\%$, we note that there is very little difference between the low field mobilities, with mobilities reaching about $1000\,\mathrm{cm^2V^{-1}s^{-1}}$, a result that is in close agreement with previous theoretical calculations, which suggest mobilities of around $1000\,\mathrm{cm^2V^{-1}s^{-1}}$ [105]. This trend that we have found is also consistent with that observed experimentally by Patané *et al.* [106] (though lower mobilities of $300 - 400\,\mathrm{cm^2V^{-1}s^{-1}}$ are seen), with there being a plateau in the low field mobility for nitrogen concentrations greater than 0.35%.

Whilst there is not much difference between the various velocity-field characteristics for higher concentrations of nitrogen in our model, there is more of a clear distinction between the energy-field characteristics and the Γ valley occupancy-field characteristics. Focussing on the energy-field characteristics at first, which are depicted in figure 7.7, we can see that in GaAs, there is a relatively quick increase in the average energy for low field strengths. As soon as nitrogen is introduced

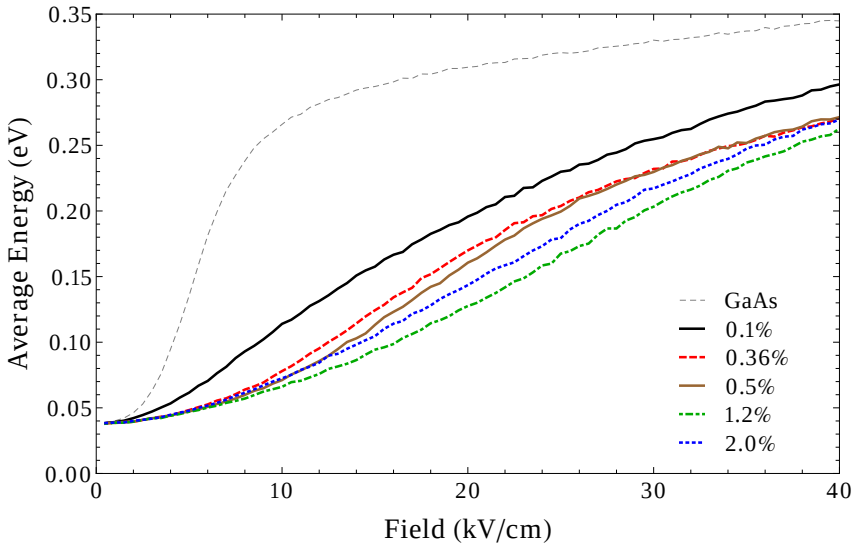

Figure 7.7) Energy-field characteristics of dilute GaN_xAs_{1-x} when using the nitrogen scattering model, with the EMC code and the **k.p** approximation. Energy is relative to the energy minima of the conduction band at the Γ point, E_c.

into the system, we see that the rate of this increase is more muted due to the increase in electron scattering in the material, inhibiting the increase in energy at higher fields. One of most interesting points that can be seen in this set of characteristics is that the rate at which the energy increases is actually lower for a nitrogen concentration of 1.2% than it is for a concentration of 2.0%. To explain this, we refer back to the nitrogen scattering rates in figure 7.2. Making a comparison between the scattering rates for nitrogen concentrations of 1.2% and 2.0%, it can be seen that the scattering rate for 1.2% is much stronger at energies less than $\sim 0.2\,\text{eV}$, and so electrons, on average, encounter many more scattering events at this lower concentration of nitrogen, which, in turn, inhibits the electrons ability to gain energy quickly. A similar effect can be seen on a much smaller scale between the characteristics for nitrogen concentrations of 0.36% and 0.5% at field strengths greater than about $30\,\text{kV/cm}$ - the scattering rate characteristic when the nitrogen concentration is 0.36% is larger than that for a concentration of 0.5% at electron energies above 0.2 eV. These effects have also been seen in recent works by Seifikar

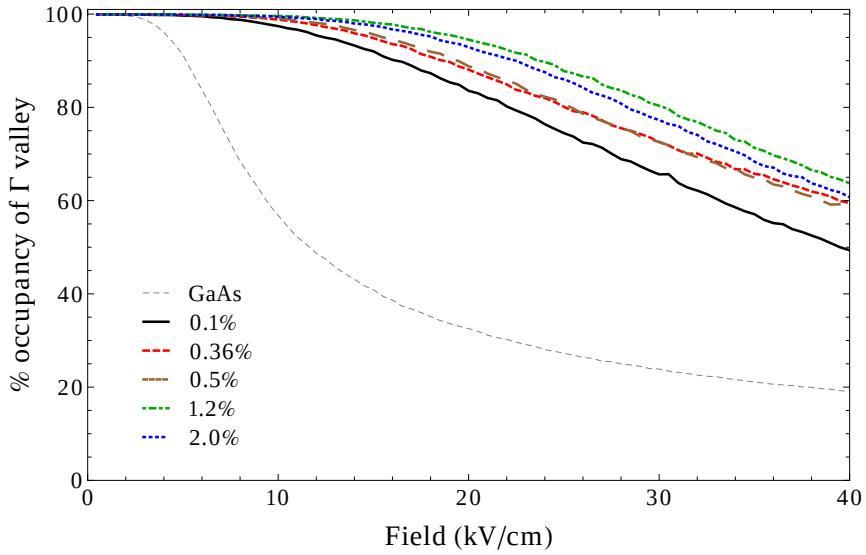

Figure 7.8) Percentage of electrons in system occupying the Γ_1 valley as a function of applied field for dilute GaN_xAs_{1-x} when using the nitrogen scattering model, with the EMC code and the **k.p** approximation.

et al. [70].

We finally discuss the Γ valley occupancy-field characteristics, illustrated in figure 7.8. As would be expected through analysis of the other characteristics, there is a much larger percentage of the system that is able to transfer to the upper L valley in bulk GaAs than there is in dilute GaN_xAs_{1-x} compounds. These characteristics match the features of the energy-field characteristics that have just been discussed, as the L-valley minima are set at 0.29 eV above that of the Γ valley. Thus, IV transfer cannot occur until electrons attain a threshold energy of 0.268 eV (i.e. the valley separation between the Γ and L valleys, minus the energy of one optical phonon), which is larger than the threshold for the effects discussed in the previous paragraph. Therefore, based on the energy-field characteristics, we would expect that the Γ valley occupancy would be higher for a nitrogen concentration of 1.2%, than it would be for 2.0% for all fields we have investigated, and this is indeed what is observed in the occupancy characteristics.

Another point of interest in these characteristics is that a "crossover" between the

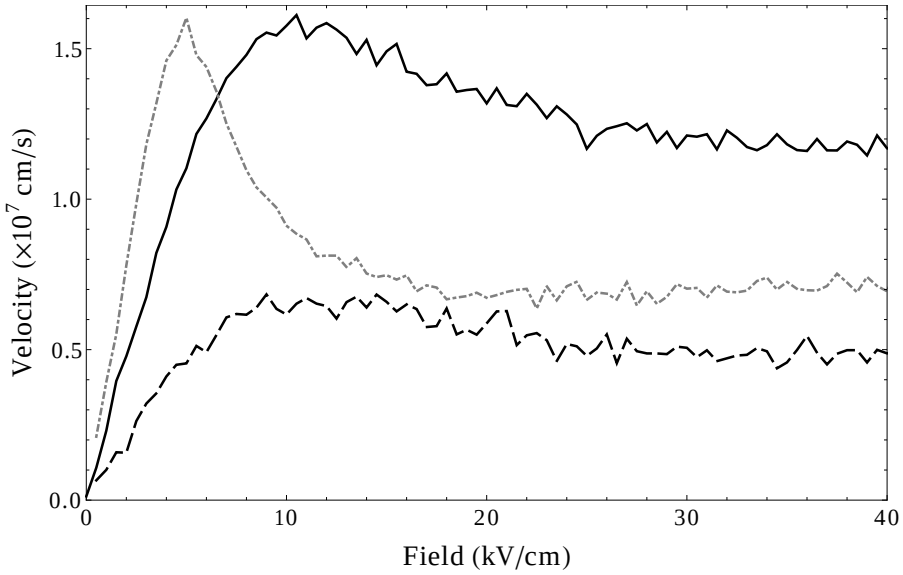

Figure 7.9) Velocity field characteristics for a nitrogen concentration of 1.2% using our analytic approximation to the E_-band (solid line), compared with the nitrogen scattering model (dashed line) and bulk GaAs (dot-dashed line). All models use the EMC code.

Γ valley occupancy characteristics for nitrogen concentrations of 0.36% and 0.5%. We can again link this to the scattering rates, the peak rate when the concentration is 0.36% is in a better position to dominate over the IV rate than the rate when the concentration is 0.5%, so when the average energy of the electron is at the threshold energy of 0.256 eV, electrons are more likely to be able to undergo IV transfer if the concentration is 0.36%. However, it's slightly more difficult for electrons to achieve this energy at this higher concentration due to a slightly larger scattering rate, due to the nitrogen doublet states, at lower energies, hence why an electron is slightly more likely to be in the Γ valley at the higher concentration when subjected to lower applied fields.

7.2.2. Analytic approximation of the E_- band

Figure 7.9 shows the velocity-field characteristics using the E_- band approximation model, compared with the bulk GaAs and the 1.2% nitrogen scattering model characteristics. While the critical field in our E_- band model is found to be similar

to that of the nitrogen scattering model at about $10 - 12\,\mathrm{kV/cm}$, the E_- band approximation suggests a peak velocity that is much greater, $1.62 \times 10^7\,\mathrm{cm/s}$ in comparison to $0.69 \times 10^7\,\mathrm{cm/s}$. It can also be seen that the peak velocity of the material is very similar to bulk GaAs under the same conditions, albeit at a higher field in the nitrogen doped case. As the scattering mechanisms used in both our E_- band approximation and the bulk GaAs case are the same, and the rates only differ at high-fields due to the different band-structure approximation in use, the similar peak velocities are conceivable. It is not surprising either to see that the peak velocity predicted by the nitrogen scattering method, which added another dominating scattering mechanism that inhibited the movement of the electrons, is much lower than that of the E_- approximation.

The shift in critical field that is seen from bulk GaAs to our approximation is due to the shape of the band-structure that is used in the respective approximations. The shape of the cosine approximation used in this model infers that the effective mass of an electron increasing in energy increases faster than it would in the **k.p** model, before it becomes negative. The effect of this is that the electron takes much longer to reach larger velocities, and hence, higher energies, such as the energy an electron needs to be able to undergo IV transfer. A larger applied field is therefore required to get the electrons up to the required energy level before scattering mechanisms can inhibit this process. The average energy-field characteristic, as shown in figure 7.10, shows that the rate of increase in the average energy with respect to the field is slower in the E_- model than bulk GaAs, but is actually faster than that predicted through the use of the nitrogen scattering model, suggesting that the carrier scattering induced by the nitrogen impurities has more of an effect on the system than the band distortion.

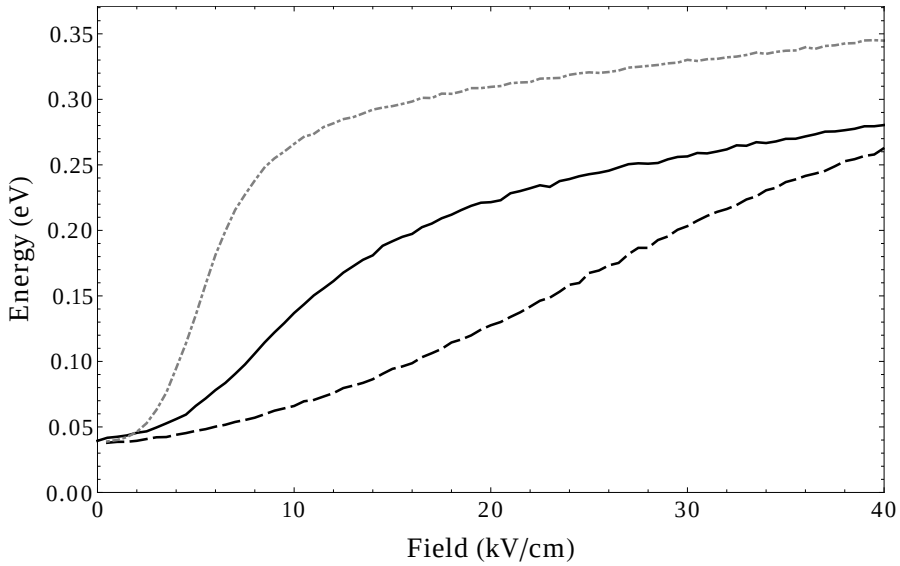

Figure 7.10) Energy-field characteristics for a nitrogen concentration of 1.2% using our analytic approximation to the E_-band (solid line), compared with the nitrogen scattering model (dashed line) and bulk GaAs (dot-dashed line), all using the EMC code. Energy is relative to the E_- band minimum.

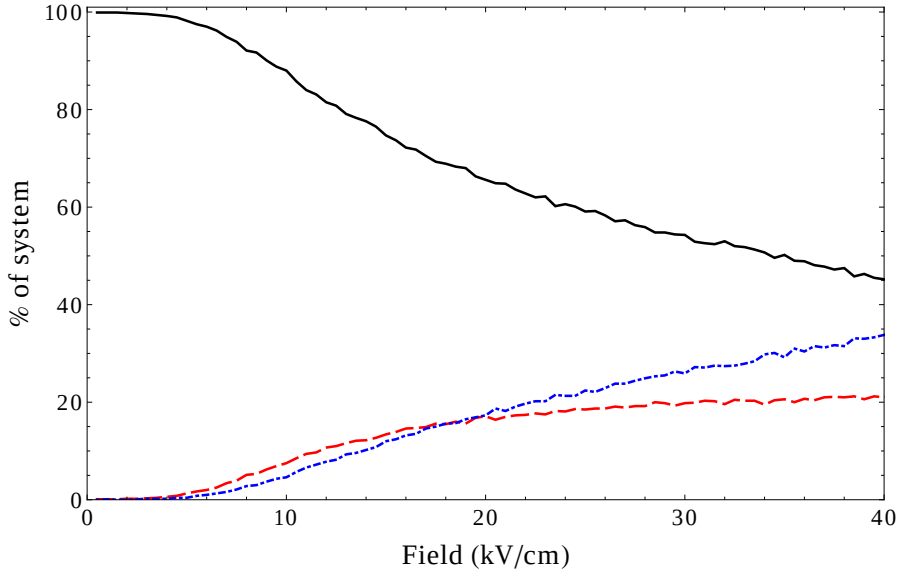

Figure 7.11) Percentage of system in the simulation under steady-state conditions total occupancy in the Γ valley/E_- band, (grey dashed line), with this split into positive (black solid) and negative (red dashed) mass components, and percentage occupation in the L valleys (blue dot-dashed), when using the analytic approximation to the E_- band with the EMC code.

We can clearly see from the Γ/E_- occupancy characteristics in figure 7.11, first looking at the total occupancy of the E_- band and the L valleys (grey and blue lines) that IV scattering is never a highly dominant factor in the electron transport in the Γ valley, and the slow transfer of electrons (with respect to the applied field) to the upper valley matches the shallow NDV characteristic seen in the velocity-field characteristic (figure 7.9). We can also look at the proportion of negative effective mass states in the E_- band, shown by figure 7.11 using the black and red lines. Like in previous chapters, we have taken a particle to be in a negative mass state based on the value of the wave-vector in the direction of the field only, as we are only interested in the velocity in the direction of the field. It can be seen that there is evidence of a slight dominance of electrons in negative mass states occurring in the E_- band over the number of electrons in the L valley at field strengths of up to 14 kV/cm. Even above this field strength, however, we find that there is still an increasing population of negative mass states under steady-state conditions as the applied field increases, reaching a population of 17% when a 30 kV/cm field is applied (with 27% of all electrons having transferred to the L valleys).

7.3. Transient characteristics

7.3.1. Nitrogen scattering model

We now turn our attention to the transient properties when a constant electric field is suddenly applied to the system. As with the steady-state case, the velocity time evolution characteristics we have found for 0.36% - 2.0% nitrogen concentrations are broadly similar to each other, so we mainly focus on the 0.1% and 0.36% concentration cases. The velocity time characteristics for these concentrations are

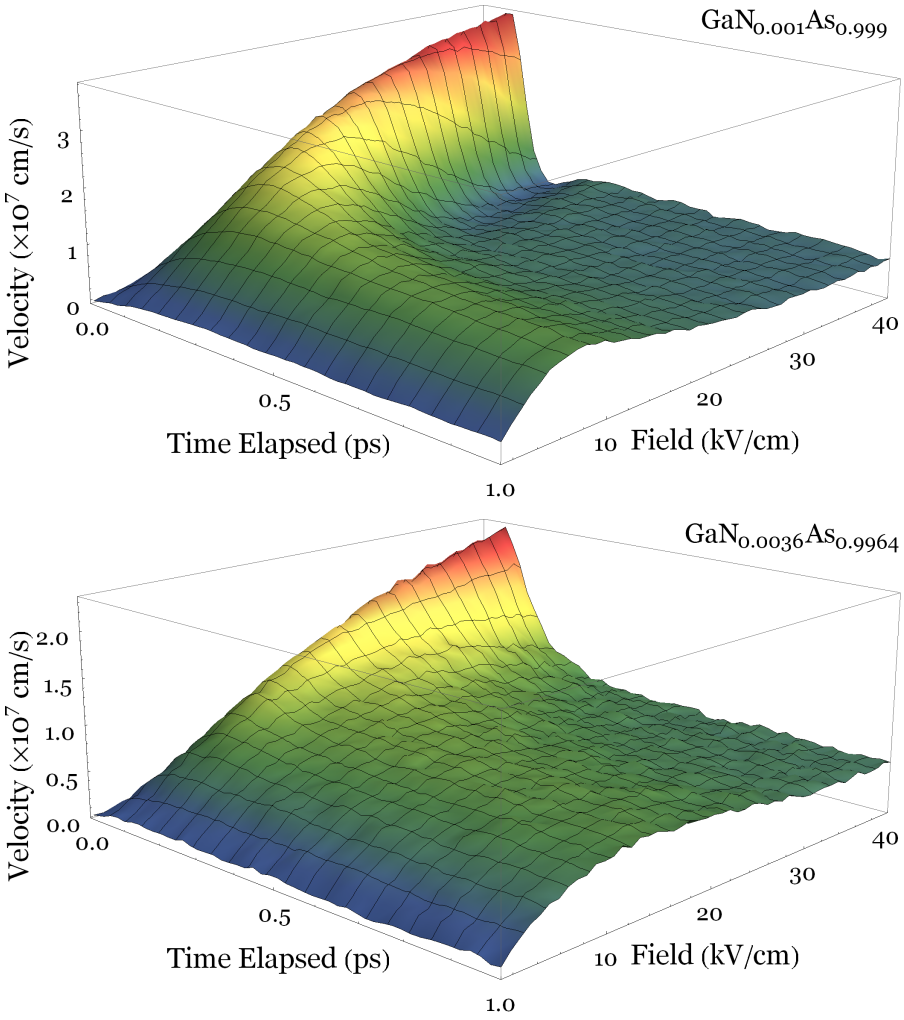

Figure 7.12) Average electron velocity as a function of time for applied fields from 0 to 40kV/cm, when using the nitrogen scattering model with the EMC code, where the nitrogen concentration is 0.1% (top) and 0.36% (bottom). The steady state velocity field characteristics of each model can be seen on the right hand side of the graph (i.e. the Velocity-Field plane at a time of 1 ps)

depicted in figure 7.12.

In both cases, it is found that the maximum velocity is limited by the nitrogen scattering, with maximum velocities at 30 kV/cm reaching only 3.4×10^7 cm/s after approximately 100 fs when there is a nitrogen concentration of 0.1%, and 1.95×10^7 cm/s after about 60 fs for nitrogen concentrations of 0.36%, in both cases lower, though occurring slightly later, than the corresponding peak velocity found in bulk GaAs at this impurity level, which is 5.8×10^7 cm/s at a time of 160 fs after the start of the simulation. This reduction in peak velocity is not

surprising, as the nitrogen scattering suppresses the ability of the system to reach higher velocities, a trend already seen in the steady-state characteristics. Higher concentrations of nitrogen also tend to increase the time it takes for electrons to reach the steady state (when compared to lower concentrations), as the magnitude of the nitrogen scattering rates inhibit the electron's ability to accelerate quickly due to a larger number of scattering events, though conversely, we find that bulk GaAs takes far longer to reach equilibrium.

To understand why this happens, in figure 7.13, velocity and energy number distributions are plotted for the first 190 fs of transport when a 40kV/cm field is applied across GaNAs with a nitrogen concentration of 0.1%. Normally, as we have already shown is the case for pure GaN, IV transfer is the main cause for net momentum reduction in the system, due to electrons losing momentum as they transfer into this upper valley, thus causing this overshoot effect. However, if we use the nitrogen scattering model, we find that this is not the case in GaN_xAs_{1-x}. It can be seen that between 30 fs and 70 fs the average velocity of the particles increases by a factor of little over 4, from 0.91×10^7 cm/s to 3.82×10^7 cm/s, as can be seen by the large shift in the peak of the distribution, whilst there is only a modest shift in the energy distribution, from 0.01 eV to just below 0.1 eV. At these energies, we see that the nitrogen scattering does not affect the characteristics of the system. At 110 fs, we begin to see the momentum re-distribution, which happens with very little transfer to the upper valley. Indeed, we see that most electrons in the system are well below the threshold energy for IV transfer, with the peak in the distribution occurring just below 0.2 eV, which is around the energy level where the nitrogen scattering mechanism becomes dominant. As we take nitrogen scattering to be an elastic isotropic mechanism, it is expected that over a large

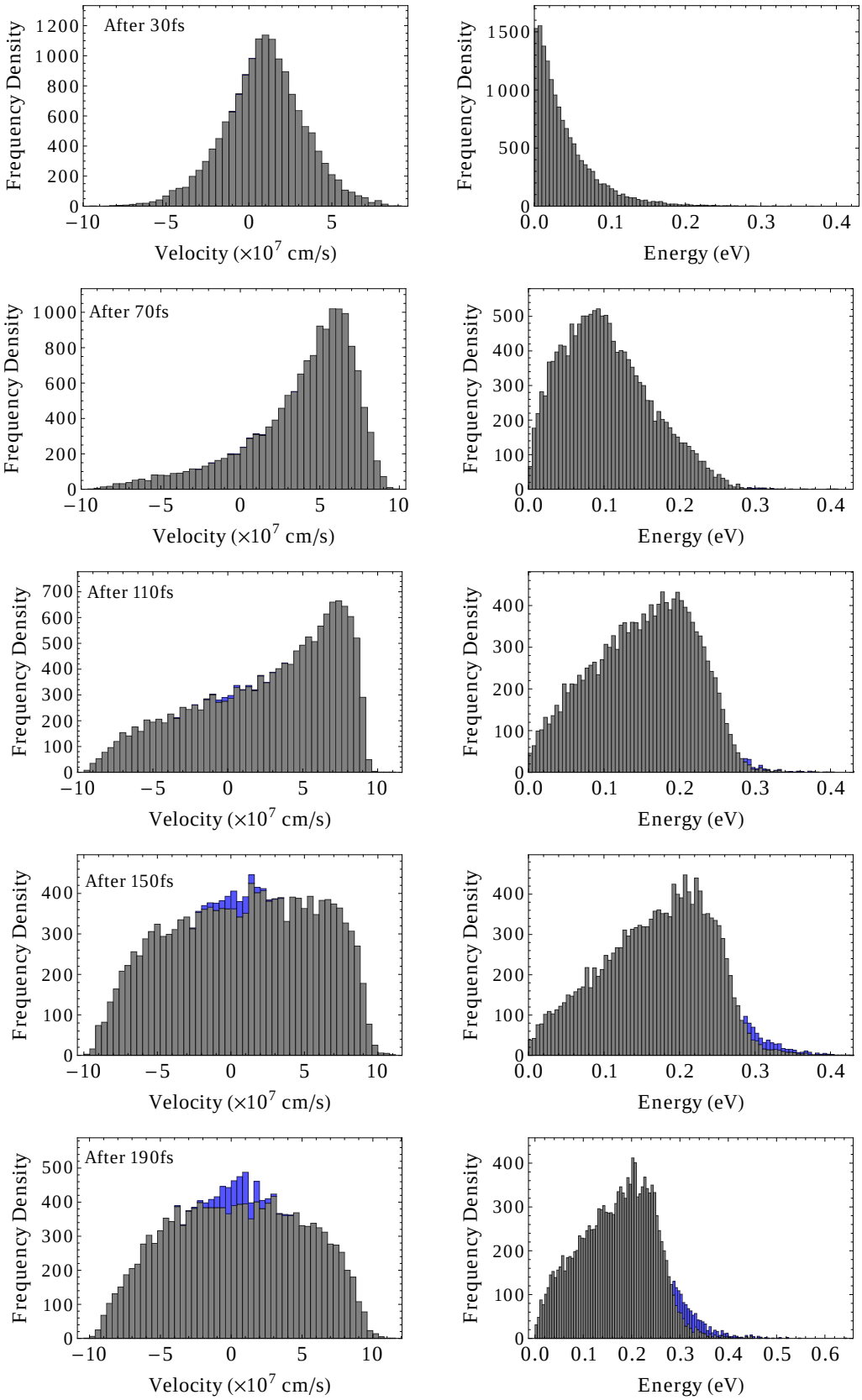

Figure 7.13) Electron velocity (left) and energy (right) distributions for GaNAs when the nitrogen concentration is 0.1% and the applied field is 40 kV/cm, as predicted by the nitrogen scattering model with the EMC code. The snapshots are taken at (from top to bottom) 30 fs, 70 fs, 110 fs, 150 fs and 190 fs. Energy is relative to the Γ valley minimum. Grey bars represent electrons in the Γ valley, blue bars, L valleys. Note that the scales are not the same on all y-axes.

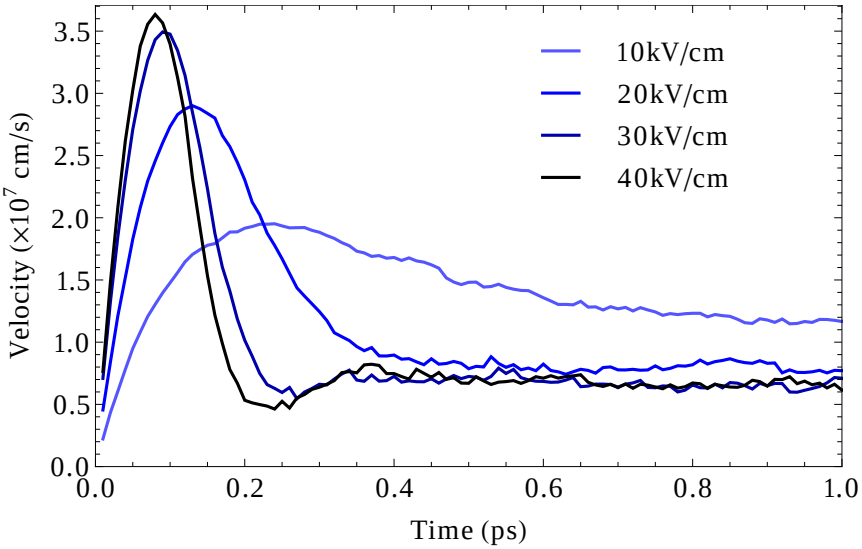

Figure 7.14) Time evolution of the average electron velocity for the 0.1% concentration nitrogen scattering model for various field strengths, when using the nitrogen scattering model with the EMC code.

number of scattering events and particles at that energy, a uniform re-distribution would be expected to occur, without effect to the magnitude of the momentum. This is indeed seen as the simulation time passes. After 190 fs have passed, we have a distribution that is almost symmetrical around the velocity 0.5×10^7 cm/s, with a small contribution from the IV scattering.

There is an interesting property that can be seen in the velocity overshoot characteristics at fields above 25 kV/cm when the nitrogen concentration is 0.1%. Figure 7.14 displays some of the characteristics at various fields, where a velocity undershoot can clearly be seen at $0.2 - 0.3$ ps for fields of 30 kV/cm and 40 kV/cm, but is absent at lower fields. When a large field is applied, most of the electrons in the system reach the energy at which nitrogen scattering becomes dominant quickly and at the same time. We have already seen this in figure 7.13, electrons reached large velocities in the direction of the field quickly and after 190 fs, the system's momentum is re-distributed, corresponding to the trough in the undershoot. The recovery from this undershoot can be seen in Figure 7.15, which depicts the electron

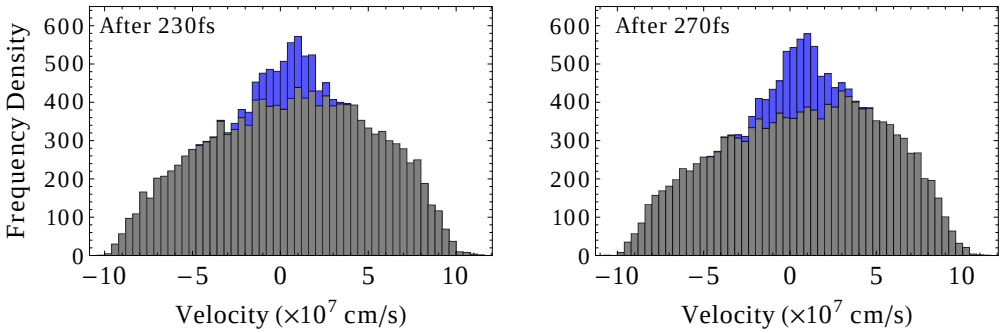

Figure 7.15) Electron velocity distributions for GaNAs when the nitrogen concentration is 0.1% and the applied field is 40 kV/cm, as predicted by the nitrogen scattering model with the EMC code. Grey bars represent electrons in the Γ valley, blue bars, L valleys.

velocity distribution at 230 fs and 270 fs. It can clearly be seen that the symmetrical distribution has once again become slightly skewed towards the positive velocities.

In low field cases, it takes longer for electrons to reach the threshold energy for the nitrogen scattering to be dominant, and thus other processes have more time to affect the electrons. Thus, a smaller volume of electrons reach the threshold energy, and due to the slower rate of energy gain due to the lower field, this happens over a longer time period. This means that the re-distribution of momentum occurs on a larger time scale, and once in equilibrium, electrons are potentially in high velocity states for longer before encountering the nitrogen scattering. If the field is low enough, only a minority of the system will have enough energy to undergo nitrogen scattering at any period, meaning it will not be dominant across the system and thus momentum re-distribution does not affect the entire system. This undershoot is not seen in higher concentration cases either, due to the low energy doublet nitrogen states, which are locally dominant, causing partial momentum re-distribution of the system, and much like in the low field cases above, this ensures that there is no undershoot.

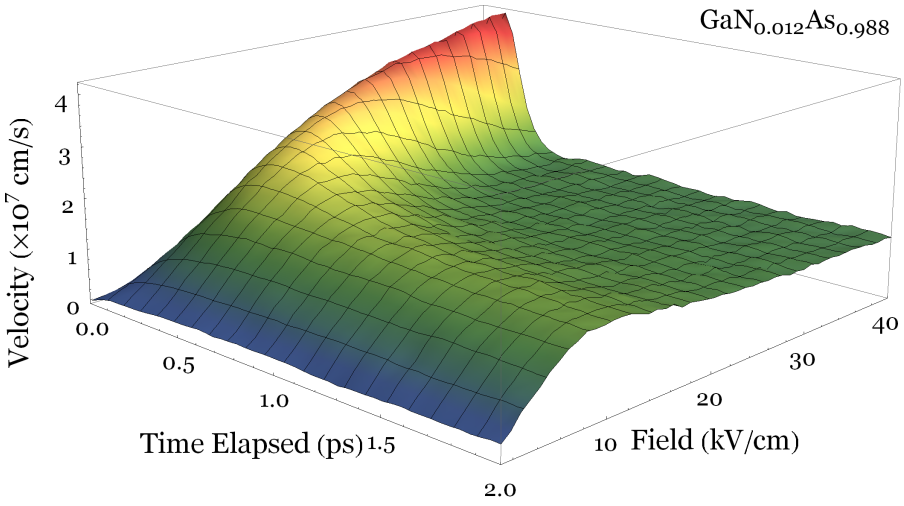

Figure 7.16) Average electron velocity as a function of time for applied fields from 0 to 40kV/cm, when modelling the E_- band using the EMC code, where the nitrogen concentration is 1.2%

7.3.2. Analytic approximation of the E_- band

Figure 7.16 depicts the transient velocity-field characteristics generated for $GaN_{0.012}As_{0.988}$. Much like in the nitrogen scattering model, we see comparable increases in the time it takes for equilibrium to be established with regards to the velocity. In contrast to the nitrogen scattering model, higher peak velocities are observed, reaching 3.8×10^7 cm/s at 30 kV/cm. This is not a surprising outcome, as it has been seen in the steady state results that the velocities from E_- band model are consistently larger than those found from the nitrogen scattering model. We find that the most interesting results that arise from this model occur at higher fields, it is immediately obvious from the transient velocities and occupancies plotted in figure 7.17 that there is a significant population of negative effective mass (NM) states before there is any IV transfer, with the population of NM states then dropping to below the population of L valley states in low field cases. This is especially prominent when a field strength of $30kV/cm$ is applied to the system, so we focus on this case to determine the effect of these NM states. We repeat the transient velocity and occupancy characteristics for 30kV/cm in figure 7.18, in order to make it easier to

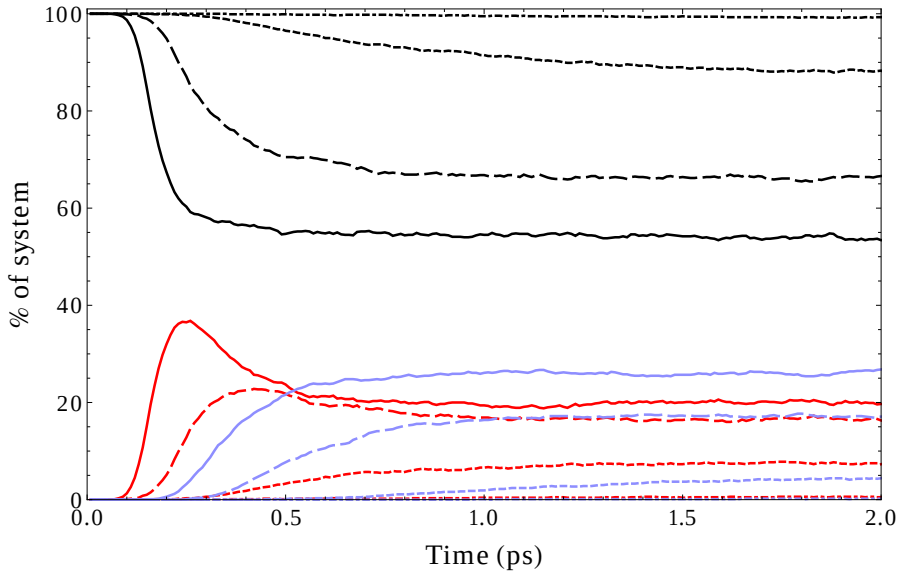

Figure 7.17) Time evolution of the occupancy of positive (black) and negative (red/dark grey) effective mass states in the Γ valley and occupying the L valleys (light blue/light grey) in $GaN_{0.012}As_{0.998}$ when using the E_- band approximation. In both graphs, characteristics at fields 4kV/cm (dot-dashed), 10kV/cm (short dashed), 20 kV/cm (long dashed) and 30 kV/cm (solid).

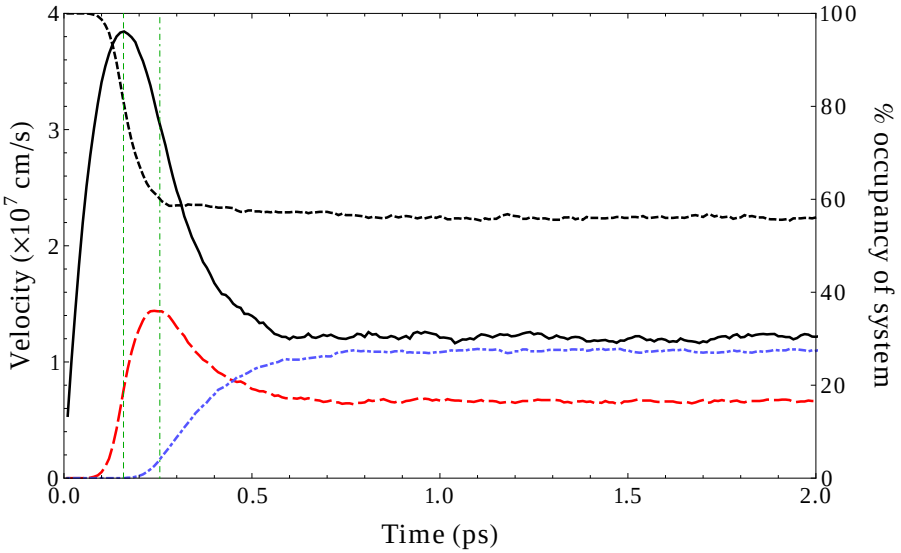

Figure 7.18) Transient properties of $GaN_{0.012}As_{0.998}$ when using the E_- band approximation using the EMC code and a field of 30kV/cm is applied. Velocity (left axis, solid black line) and occupancy (right axis) of Γ valley, positive (black dashed) and negative (red dashed) mass states, and the L valleys (blue dot-dashed line). The green vertical lines note two times of interest 1) the occurrence of the peak velocity before any IV transfer, and 2) the occurrence of the peak NM occupancy.

match the features of the characteristics.

We first note that NM states begin to occur at about 80 fs in to the simulation, well before IV transfer begins (at about 190 fs). This marks the start of a small period of time (about 400 fs) where there is a significant dominance of NM states over L valley states. At approximately 160 fs, (denoted by the dashed green line on figure 7.18) the peak overshoot velocity or 3.8×10^7 cm/s is attained. At this point in the simulation, we find that there is 0% occupancy in the upper L valleys, while approximately 19% of electrons are in NM states, deceasing the average velocity of the system, and thus causing the overshoot effect to occur earlier than it would have done in the absence of these states. Shortly after this peak velocity is reached, IV transfer begins to occur, however, the occupancy of NM states initially increases faster than the occupancy of the L valleys, before the occupancy of NM states peaks at 36.5% of the system after 250 fs (denoted by the dot-dashed green line). Beyond this time, IV transfer becomes the preferred mechanism for the velocity characteristic, with L valley occupancy increasing at the expense of the NM states, with there being more electrons occupying L valleys than NM states after 420 fs. Thus, our model suggests that NM states have a significant effect on the transient velocity profile, as the effect of the NM states causes the velocity to peak before any IV transfer begins to occur.

7.4. Summary

Through the use of two models of the GaN_xAs_{1-x} band structure in an ensemble Monte Carlo code, we have examined the steady-state and transient electron transport properties of GaN_xAs_{1-x}. Our two models allow us to quantify the effects of

band distortion and nitrogen scattering on the transport properties of GaN_xAs_{1-x}. We find for the steady-state regime that both models suggest a decrease in the low-field mobility when compared with GaAs. Both models also imply that the critical field is shifted to higher values due to the distortive effect the Nitrogen has on the host band-structure. The effect of adding the nitrogen scattering mechanism is that it reduces the peak velocity attained in the steady state, and as a result of this, we therefore find that our nitrogen scattering model is a much better fit to current experimental data [106] and analytic theoretical predictions [102, 105].

While our nitrogen scattering model assumes non-parabolic band, it does not include the distortion characteristic of the BAC model. By using an analytic approximation for the E_- band in the BAC a useful insight is gained into the potential effects of negative effective mass states, particularly under transient conditions. Through analysis of the transient regime using both models, we find that there is a noticeable decrease in the peak velocity attained. With the second model, in mid-field cases (5 - 14 kV/cm), there is always a larger population of electrons in NM states than there are in L-valley states, though a maximum of 10% of the electrons in the system occupies either state at any time. At fields greater than 15 kV/cm, there is a significant population of electrons occupying NM states (reaching peak occupancies of 23% at 20 kV/cm and 36% at 30 kV/cm) for the first 500fs of transport before the electron occupation in the L-valleys becomes greater than that of the NM states.

We conclude that the occupation of NM states has a significant effect on the transient properties of GaN_xAs_{1-x}, decreasing the peak velocity attained in the velocity overshoot. The use of an analytic approximation of the E_- band suggests that the distortion of the band causes a shift in the critical field. Furthermore,

through the use of our nitrogen scattering model, we find a reduction in the peak velocity attained in both the steady-state and transient regimes when compared with bulk GaAs; these steady-state results are in agreement with experimental data and analytic theoretical works.

Chapter 8
Conclusions and Future Work

Throughout this thesis, we have explored the properties of the III-V materials Gallium Nitride and dilute Gallium Nitrogen Arsenide, using a new, novel band structure approximation, based on a cosine function, that allows us to access and simulate the effects of electrons in negative effective mass states that occur around the Γ points of the materials. New expressions for the scattering mechanisms were derived in chapter 3 that take advantage of this approximation, and using these expressions, in chapter 4 we successfully demonstrated that this approximation provided us with accurate results when coupled with ensemble Monte-Carlo algorithms. This was done by comparing our results with results from simulations performed with the **k.p** band-structure approximation and other works, whilst retaining the fast nature of the code when compared with numerical full-band structure based models. We were thus able to use this new band-structure in ensemble bulk and 1D device Monte-Carlo simulations in order to determine the effects of negative effective mass states and other features from the highly non-parabolic character of the band-structure in both GaN (in chapters 5 & 6), and dilute GaN_xAs_{1-x} (in chapter 7).

We found that in bulk GaN, the effect of the negative effective mass states were dependent on the energy difference between the local minima at the Γ and M-L points in the conduction band, with there only being a noticeable population of negative effective mass states forming when this valley separation is large. Regardless of the valley separation that was used, however, the use of this band-structure approximation produces characteristics that are close to those suggested by experimental data [7] and by other simulations that use numerical, full-band struc-

ture models [17, 97]. We also successfully demonstrated some characteristics of a nanoscale one-dimensional device using a coupled Ensemble Monte Carlo/Poission solver algorithm, illustrating some of the effects that can occur within such a device.

In the investigation into dilute GaNAs (in chapter 7), we first developed analytic forms of the nitrogen scattering rates as used in the nitrogen scattering model for GaNAs, as determined by Fahy *et al.* [101] using the linear combination of isolated nitrogen state methods, and successfully obtained rates to use in our ensemble Monte Carlo codes, obtaining steady-state velocity-field results similar to those obtained by Seifikar *et al.* [70] and low-field mobilities in good agreement with other theoretical works [105]. We also investigated the transient properties of GaNAs using this model, noting that transient transport is driven by nitrogen scattering rather than intervalley transfer, as is the case in GaN. We also investigated the steady state and transient characteristics using a BAC like model when the nitrogen concentration in the compound is 1.2%, simulating the lower BAC band using the cosine band-structure approximation, discovering that negative effective mass states in the E_- band play a vital role in the characteristics of the system.

The work presented in this thesis also presents itself a good base for future works. On the basis that we were able to derive three-dimensional scattering rates (as shown in chapter 3), future projects involve the derivation of two-dimensional scattering rates using the cosine band-structure approximation for use in determining the transport properties of electrons confined in two-dimensional electron gasses (2DEGs). Leading on from this, drawing from the work on development of bulk and one-dimensional systems using the cosine-band structure models coupled with work on 2DEG scattering rate derivation, the next step in the evolution of our methods is to move onto two-dimensional simulations of structures. While

simple devices with an anode, cathode and active region, similar to the 1D device we presented in chapter 6 can be modeled in two dimensions without the presence of 2DEGs, the creation of models containing these 2DEG systems will allow for the development of more complex device models, such as high electron mobility transistors, that utilize the high electron mobilities that 2DEGs offer.

Appendix A
Determination of Scattering Angle for Piezoelectric Scattering

A.1. Derivation for a Parabolic Band

As described in section 2.2.4.2, in order to determine the probability of an electron scattering with an angle θ', $W_t(E_k)_{\theta:0-\theta'}/W_t(E_k)_{\theta:0-\pi}$ must be solved for $\cos(\theta')$. We will do so here for piezoelectric scattering when a parabolic band-structure is used.

We start with the overall piezoelectric scattering rate through all angles, $W_t(E_k)_{\theta:0-\pi}$, which has previously been shown to be [22],

$$\begin{aligned} W_t(E_k)_{\theta:0-\pi} &= \frac{e^2 K_{av}^2 k_B T}{8\pi^2 \epsilon \hbar} \int_0^{2k} \int_{-1}^{1} \int_0^{2\pi} \frac{q^2}{\left(q^2+q_0^2\right)^2} \delta_{\mathbf{k}\pm\mathbf{q}-\mathbf{k}',0} \\ &\times \delta\left(E_{\mathbf{k}'} - E_{\mathbf{k}} \mp \hbar\omega_{\mathbf{q}}\right) d\phi \, d\cos\left(\theta\right) \, dq. \end{aligned} \tag{A.1.1}$$

This integrates to,

$$W_t(E_k)_{\theta:0-\pi} = \frac{e^2 K_{av}^2 k_B T}{4\pi \epsilon \hbar} \left(\ln\left[1+\frac{4k^2}{q_0^2}\right] - \frac{4k^2}{q_0^2+4k^2} \right). \tag{A.1.2}$$

In order to determine the scattering rate for scattering between 0 (i.e. no change to the wave-vector direction) a polar angle θ', i.e. $W_t(E_k)_{\theta:0-\theta'}$, we must alter the above integral accordingly so that we are only integrate over the range of angles we are interested in. We thus change the limits of the integral over $\cos\theta'$, obtaining,

$$W_t(E_k)_{\theta:0-\theta'} = \frac{e^2 K_{av}^2 k_B T}{8\pi^2 \epsilon \hbar} \int_0^{2k} \int_{\cos\theta'}^{1} \int_0^{2\pi} \frac{q^2}{\left(q^2+q_0^2\right)^2} \delta_{\mathbf{k}\pm\mathbf{q}-\mathbf{k}',0} \tag{A.1.3}$$

$$\times \delta\left(E_{\mathbf{k}'} - E_{\mathbf{k}} \mp \hbar\omega_{\mathbf{q}}\right) d\phi \, d\cos\left(\theta\right) \, dq. \tag{A.1.4}$$

Integrating this, we obtain,

$$W_t(E_k)_{\theta:0-\theta'} = \frac{e^2 K_{av}^2 k_B T}{4\pi\epsilon\hbar}\left(\ln\left[1+\frac{2k^2-2k^2\cos(\theta')}{q_0^2}\right]-\frac{2k^2-2k^2\cos(\theta')}{q_0^2+2k^2-2k^2\cos(\theta')}\right). \tag{A.1.5}$$

We can now obtain a cumulative probability function as a function of $\cos(\theta')$ by dividing A.1.3 by A.1.2, thus obtaining,

$$\frac{W_t(E_k)_{\theta:0-\theta'}}{W_t(E_k)_{\theta:0-\pi}} = \frac{\ln\left[1+\frac{2k^2-2k^2\cos(\theta')}{q_0^2}\right]-\frac{2k^2-2k^2\cos(\theta')}{q_0^2+2k^2-2k^2\cos(\theta')}}{\ln\left[1+\frac{4k^2}{q_0^2}\right]-\frac{4k^2}{q_0^2+4k^2}}. \tag{A.1.6}$$

We know that $W_t(E_k)_{\theta:0-\theta'}/W_t(E_k)_{\theta:0-\pi}$ must be a value between 0 and 1, henceforth, we shall denote this quantity by the variable r. We now need to re-arrange this equation in terms of $cos\,(\theta')$. We let $\chi = \ln\left[1+\frac{4k^2}{q_0^2}\right]-\frac{4k^2}{q_0^2+4k^2}$, as we can treat k (magnitude of electron wave-vector) and q_0 (screening) as constant throughout this derivation. We then make the following substitutions,

$$r_1 = \ln\left[1+\frac{2k^2\,(1-\cos(\theta'))}{q_0^2}\right] \tag{A.1.7}$$

$$r_2 = -\frac{2k^2-2k^2\cos(\theta')}{(q_0^2+2k^2-2k^2\cos(\theta'))} \tag{A.1.8}$$

which in turn reduces (A.1.5) to,

$$\chi r = r_1 + r_2. \tag{A.1.9}$$

We now have a pair of simultaneous equations to solve. Rearranging both in

terms of $\cos(\theta')$, we get,

$$\cos(\theta') = \frac{2k^2 + (1 - \exp[r_1])\, q_0^2}{2k^2} \tag{A.1.10}$$

$$\cos(\theta') = \frac{2k^2(r_2 + 1) + q_0^2 r_2}{2k^2(r_2 + 1)}. \tag{A.1.11}$$

For both equations to hold true, the value of $\cos(\theta')$ must be the same in both equations. We can thus get r_2 in terms of r_1 by equating the two right-hand sides,

$$2k^2 + (1 - \exp[r_1])\, q_0^2 = \frac{2k^2(r_2 + 1) + q_0^2 r_2}{(r_2 + 1)}. \tag{A.1.12}$$

This reduces to,

$$1 - \exp[r_1] = \frac{r_2}{r_2 + 1}. \tag{A.1.13}$$

Taking the reciprocal of (A.1.13), we obtain;

$$\frac{1}{1 - \exp[r_1]} = 1 + \frac{1}{r_2} \tag{A.1.14}$$

$$\frac{\exp[r_1]}{1 - \exp[r_1]} = \frac{1}{r_2}. \tag{A.1.15}$$

Taking the reciprocal once more,

$$r_2 = \exp[-r_1](1 - \exp[r_1]) = \exp[-r_1] - 1. \tag{A.1.16}$$

We can now substitute (A.1.16) into (A.1.11) and solve for $\cos(\theta')$,

$$\cos(\theta') = 1 + \frac{q_0^2\,(\exp[-r_1] - 1)}{2k^2 \exp[-r_1]} = 1 + \frac{q_0^2\,(1 - \exp[-r_1])}{2k^2}. \tag{A.1.17}$$

Now, using the relation established in (A.1.9), we obtain a relation between r and r_1,

$$\chi r = r_1 + \exp[-r_1] - 1. \tag{A.1.18}$$

Rearranging in terms of r_1, we get,

$$r_1 = 1 + \chi r + W_0\left(-\exp\left[-1-\chi r\right]\right). \tag{A.1.19}$$

where W_0 denotes the principal branch of the Lambert W function. Substituting this into (A.1.17) yields the equation used to determine the scattering angle of an electron subjected to piezoelectric scattering (which is the equation given in (2.2.19)),

$$\cos(\theta') = \frac{1}{2k^2}\left(2k^2 + q_0^2\left(1 - \exp\left[1 + \chi r + W_0\left(-\exp\left[-1-\chi r\right]\right)\right]\right)\right). \tag{A.1.20}$$

The Lambert W function can only be solved numerically. Fortunately, fast numerical subroutines exist that allows for approximate solutions to be found, see Barry *et al.* [107] for a good example.

References

[1] J. Hacker, M. Seo, A. Young, Z. Griffith, M. Urteaga, T. Reed, and M. Rodwell, in *2010 IEEE MTT-S International Microwave Symposium* (IEEE, 2010) pp. 1126–1129.

[2] C. Nguyen and M. Micovic, IEEE Transactions on Electron Devices **48**, 472 (2001).

[3] A. Dyson and B. K. Ridley, Journal of Applied Physics **104**, 113709 (2008).

[4] L. A. Samoska, IEEE Transactions on Terahertz Science and Technology **1**, 9 (2011).

[5] A. V. Muravjov, D. B. Veksler, V. V. Popov, O. V. Polischuk, N. Pala, X. Hu, R. Gaska, H. Saxena, R. E. Peale, and M. S. Shur, Applied Physics Letters **96**, 042105 (2010).

[6] R. P. Joshi, S. Viswanadha, P. Shah, and R. D. del Rosario, Journal of Applied Physics **93**, 4836 (2003).

[7] J. M. Barker, R. Akis, T. J. Thornton, D. K. Ferry, and S. M. Goodnick, Physica Status Solidi (a) **190**, 263 (2002).

[8] C. Xie and A. Pavio, in *MILCOM 2007 - IEEE Military Communications Conference* (IEEE, 2007) pp. 1–4.

[9] K. Krishnamurthy, J. Martin, B. Landberg, R. Vetury, and M. J. Poulton, in *2008 IEEE MTT-S International Microwave Symposium Digest* (IEEE, 2008) pp. 303–306.

[10] A. Patanè, A. Ignatov, D. Fowler, O. Makarovsky, L. Eaves, L. Geelhaar, and H. Riechert, Physical Review B **72**, 2 (2005).

[11] N. Vogiatzis and J. M. Rorison, Journal of Applied Physics **109**, 083720 (2011).

[12] G. Allison, S. Spasov, a. Patanè, L. Eaves, a. Ignatov, D. Maude, M. Hopkinson, and R. Airey, Physical Review B **75**, 2 (2007).

[13] W. G. Bi and C. W. Tu, Journal of Applied Physics **80**, 1934 (1996).

[14] M. Lundstrom, *Fundamentals of carrier transport*, second edi ed. (Cambridge University Page, Cambridge, 2000).

[15] C. Kittel, *Introduction to Solid State Physics*, 8th ed. (John Wiley & Sons, Inc., Hoboken, 2005).

[16] R. D. Kronig and W. G. Penney, in *Proceedings of the Royal Society of London*, Vol. 130 (1931) pp. 499–513.

[17] S. Yamakawa, R. Akis, N. Faralli, M. Saraniti, and S. M. Goodnick, Journal of Physics: Condensed Matter **21**, 174206 (2009).

[18] C. Bulutay, B. Ridley, and N. Zakhleniuk, Physical Review B **62**, 15754 (2000).

[19] B. Guo, H. Guo, S. Zhang, and D. Song, Physica B: Condensed Matter **405**, 4925 (2010).

[20] J. Wu, W. Walukiewicz, and E. Haller, Physical Review B **65**, 233210 (2002).

[21] D. K. Ferry, *Semiconductor Transport*, 1st ed. (Taylor & Francis, London, 2000).

[22] B. K. Ridley, *Quantum Processes in Semiconductors*, 2nd ed. (Oxford University Press, 1988).

[23] E. O. Kane, in *Semiconductors and Semimetals: Volume 1*, edited by R. K. Willardson and A. C. Beer (Academic Press, London, 1966) Chap. 3.

[24] M. P. Vaughan, *Alloy and phonon scattering-limited electron mobility in dilute nitrides*, Ph.D. thesis, University of Essex (2007).

[25] K. Tomizawa, *Numerical Simlulation of Submicron Semiconductor Devices* (Artech House, 1993).

[26] W. A. Hadi, S. K. OâĂŹLeary, M. S. Shur, and L. F. Eastman, Solid State Communications **151**, 874 (2011).

[27] J. A. Reissland, *The Physics of Phonons* (John Wiley & Sons Ltd., London, 1973).

[28] J. Schwinger, *Quantum Mechanics: Symbolism of Atomic Measurements*, edited by B.-G. Englert (Springer Berlin Heidelberg, Berlin/Heidelberg, 2001).

[29] B. K. Ridley, *Electrons and Phonons in Semiconductor Multilayers*, 2nd ed. (Cambridge University Press, Cambridge, 2009).

[30] M. A. Littlejohn, J. R. Hauser, and T. H. Glisson, Physics **48**, 4587 (1977).

[31] INSPEC, *Properties of Gallium Arsenide* (The Institution of Electrical Engineers, London, 1986).

[32] S. M. Sze, *Semiconductor Devices: Physics and Technology*, 2nd ed. (John Wiley & Sons, Inc., Hoboken, 2002).

[33] J. Gunn, Solid State Communications **1**, 88 (1963).

[34] B. K. Ridley and T. B. Watkins, Proceedings of the Physical Society **78**, 293 (1961).

[35] C. Hilsum, Proceedings of the IRE **50**, 185 (1962).

[36] B. K. Ridley, W. J. Schaff, and L. F. Eastman, Journal of Applied Physics **97**, 094503 (2005).

[37] A. Dyson and B. K. Ridley, Journal of Applied Physics **108**, 104504 (2010).

[38] S. Nakamura and G. Fasol, *The Blue Laser Diode, GaN Based Light Emitters and Lasers* (Springer-Verlag, Berlin, 1997).

[39] S. Y. Ren and J. D. Dow, Applied Physics Letters **69**, 251 (1996).

[40] F. Roccaforte, M.-H. Weng, C. Bongiorno, F. Giannazzo, F. Iucolano, and V. Raineri, Applied Physics A **100**, 197 (2010).

[41] S. Nakamura, M. Senoh, S.-i. Nagahama, N. Iwasa, T. Yamada, T. Matsushita, H. Kiyoku, Y. Sugimoto, T. Kozaki, H. Umemoto, M. Sano, and K. Chocho, Applied Physics Letters **72**, 2014 (1998).

[42] J. Lee, J. Kim, and H. Jeon, Current Applied Physics **9**, 663 (2008).

[43] S. Mingiacchi, P. Lugli, A. Bonfiglio, G. Conte, M. Eickhoff, O. Ambacher, A. Rizzi, A. Passaseo, P. Visconti, and R. Cingolani, physica status solidi (a) **190**, 281 (2002).

[44] B. E. Foutz, S. K. O'Leary, M. S. Shur, and L. F. Eastman, Journal of Applied Physics **85**, 7727 (1999).

[45] B. Aslan, L. F. Eastman, and Q. Diduck, International Journal of High Speed Electronics and Systems **19**, 1 (2009).

[46] R. Gaska, Q. Chen, J. Yang, A. Osinsky, M. Asif Kahn, and M. Shur, IEEE Electron Device Letters **18**, 492 (1997).

[47] B. Kim, D. Derickson, and C. Sun, in *2007 Asia-Pacific Microwave Conference* (IEEE, 2007) pp. 1–4.

[48] K. Joshin and T. Kikkawa, in *2008 IEEE Radio and Wireless Symposium* (IEEE, 2008) pp. 65–68.

[49] A. Ashok, D. Vasileska, O. L. Hartin, and S. M. Goodnick, IEEE Transactions on Electron Devices **57**, 562 (2010).

[50] R. Vetury, D. Green, S. Gibb, T. Mercier, K. Leverich, P. Garber, M. Poulton, and J. Shealy, in *IEEE MTT-S International Microwave Symposium Digest, 2005.*, Vol. 00 (IEEE, 2005) pp. 487–490.

[51] T. Kikkawa, T. Iwai, and T. Ohki, Fujitsu Sci Tech **44**, 333 (2008).

[52] J. D. Sun, Y. F. Sun, Y. Zhou, Z. P. Zhang, W. K. Lin, C. H. Zen, D. M. Wu, B. S. Zhang, H. Qin, L. L. Li, W. Xu, J. Ihm, and H. Cheong, in *AIP Confrence Proceedings*, Vol. 893 (2011) pp. 893–894.

[53] A. El Fatimy, S. Boubanga Tombet, F. Teppe, W. Knap, D. Veksler, S. Rumyantsev, M. Shur, N. Pala, R. Gaska, Q. Fareed, X. Hu, D. Seliuta, G. Valusis, C. Gaquiere, D. Theron, and A. Cappy, Electronics Letters **42**, 1342 (2006).

[54] J. T. Lü and J. C. Cao, Semiconductor Science and Technology **19**, 451 (2004).

[55] H. Krömer, Physical Review **109**, 1856 (1958).

[56] R. F. Macpherson, G. M. Dunn, and N. J. Pilgrim, Semiconductor Science and Technology **23**, 055005 (2008).

[57] L.-A. Yang, Y. Hao, Q. Yao, and J. Zhang, IEEE Transactions on Electron Devices **58**, 1076 (2011).

[58] O. Yilmazoglu, K. Mutamba, D. Pavlidis, and T. Karaduman, Electronics Letters **43**, 480 (2007).

[59] J. M. Barker, D. K. Ferry, D. D. Koleske, and R. J. Shul, Journal of Applied Physics **97**, 063705 (2005).

[60] M. Weyers, M. Sato, and H. Ando, Japanese Journal of Applied Physics **31**, L853 (1992).

[61] U. Tisch, E. Finkman, and J. Salzman, Applied Physics Letters **81**, 463 (2002).

[62] J. E. Lowther, S. K. Estreicher, and H. Temkin, Applied Physics Letters **79**, 200 (2001).

[63] J. Perkins, A. Mascarenhas, Y. Zhang, J. Geisz, D. Friedman, J. Olson, and S. Kurtz, Physical Review Letters **82**, 3312 (1999).

[64] Y. Zhang, A. Mascarenhas, H. Xin, and C. Tu, Physical Review B **61**, 7479 (2000).

[65] G. Pozina, I. Ivanov, B. Monemar, J. V. Thordson, and T. G. Andersson, Journal of Applied Physics **84**, 3830 (1998).

[66] W. Shan, W. Walukiewicz, J. Ager, E. Haller, J. Geisz, D. Friedman, J. Olson, and S. Kurtz, Physical Review Letters **82**, 1221 (1999).

[67] R. J. Potter and N. Balkan, Journal of Physics: Condensed Matter **16**, S3387 (2004).

[68] N. López, L. Reichertz, K. Yu, K. Campman, and W. Walukiewicz, Physical Review Letters **106**, 1 (2011).

[69] N. Vogiatzis and J. M. Rorison, Physica Status Solidi (B) **248**, 1183 (2011).

[70] M. Seifikar, E. P. O'Reilly, and S. Fahy, Physical Review B **84**, 1 (2011).

[71] A. Ignatov, A. PataneÌĂ, O. Makarovsky, and L. Eaves, Applied Physics Letters **88**, 032107 (2006).

[72] D. Vasileska and S. M. Goodnick, *Computational Electronics*, Synthesis Lectures on Computational Electronmagnets (Morgan & Claypool Publishers, 2006).

[73] D. C. Look and J. R. Sizelove, Physical Review Letters **82**, 1237 (1999).

[74] J. S. Blakemore, Journal of Applied Physics **53**, R123 (1982).

[75] M. Fischetti and S. Laux, Physical Review B **38**, 9721 (1988).

[76] H. Thomas, D. V. Morgan, B. Thomas, J. E. Aubrey, and G. B. Morgan, eds., *Gallium Arsenide for Devices and Integrated Circuits* (Peter Penegrinus Ltd., London, 1986).

[77] A. Khalid, N. J. Pilgrim, G. M. Dunn, M. C. Holland, C. R. Stanley, I. G. Thayne, and D. R. S. Cumming, IEEE Electron Device Letters **28**, 849 (2007).

[78] B. Baliga, R. Ehle, J. Shealy, W. Garwacki, and W. Garwacki, IEEE Electron Device Letters **2**, 302 (1981).

[79] L. Eastman and U. Mishra, IEEE Spectrum **39**, 28 (2002).

[80] T. J. Maloney and J. Frey, Journal of Applied Physics **48**, 781 (1977).

[81] J. D. Albrecht, P. P. Ruden, S. Limpijumnong, W. R. L. Lambrecht, and K. F. Brennan, Journal of Applied Physics **86**, 6864 (1999).

[82] F. Bertazzi, M. Goano, and E. Bellotti, Journal of Electronic Materials **36**, 857 (2007).

[83] E. Furno, F. Bertazzi, M. Goano, G. Ghione, and E. Bellotti, Solid-State Electronics **52**, 1796 (2008).

[84] S. K. O'Leary, B. E. Foutz, M. S. Shur, and L. F. Eastman, Solid State Communications **150**, 2182 (2010).

[85] C. F. Klingshirn, B. K. Meyer, A. Waag, A. Hoffmann, and J. M. M. Geurts, *Zinc Oxide: From Fundamental Properties Towards Novel Applications* (Springer, 2010) p. 359.

[86] B.-Y. Oh, M.-C. Jeong, T.-H. Moon, W. Lee, J.-M. Myoung, J.-Y. Hwang, and D.-S. Seo, Journal of Applied Physics **99**, 124505 (2006).

[87] R. KÃűnenkamp, R. C. Word, and C. Schlegel, Applied Physics Letters **85**, 6004 (2004).

[88] O. Madelung, U. Rössler, and M. Schulz, eds., *II-VI and I-VII Compounds; Semimagnetic Compounds*, Landolt-Börnstein - Group III Condensed Matter, Vol. 41B (Springer-Verlag, Berlin/Heidelberg, 1999).

[89] O. Madelung, U. Rössler, and M. Schulz, eds., *Group IV Elements, IV-IV and III-V Compounds. Part a - Lattice Properties*, Landolt-Börnstein - Group III Condensed Matter, Vol. a (Springer-Verlag, Berlin/Heidelberg, 2001).

[90] M. Goano, F. Bertazzi, M. Penna, and E. Bellotti, Journal of Applied Physics **102**, 083709 (2007).

[91] E. Bellotti and F. Bertazzi, *Nitride Semiconductor Devices*, edited by J. Piprek (Wiley-VCH, Weinheim, 2007) Chap. 4, pp. 69–94.

[92] V. Bougrov, M. E. Levinshtein, S. L. Rumyantsev, and A. Zubrilov, "Properties of Advanced Semiconductor Materials," (John Wiley & Sons, Inc., New York, 2001) pp. 1–30.

[93] T. P. Chow and Ghezzo, in *III-Nitride, SiC, and Diamond Materials for Electronic Devices*, Vol. 423, edited by D. K. Gaskill, C. D. Brandt, and R. J. Nemanich (Material Research Society Symposium Proceedings, Pittsburgh, PA., 1996) pp. 69–73.

[94] M. Semenenko, O. Yilmazoglu, H. L. Hartnagel, and D. Pavlidis, Journal of Applied Physics **109**, 023703 (2011).

[95] C. Bulutay, B. K. Ridley, and N. A. Zakhleniuk, Physical Review B **68**, 115201 (2003).

[96] M. Ilegems and H. Montgomery, Journal of Physics and Chemistry of Solids **34**, 885 (1973).

[97] I. M. Abdel-Motaleb and R. Y. Korotkov, Journal of Applied Physics **97**, 093715 (2005).

[98] P. Perlin, T. Swietlik, L. Marona, R. Czernecki, T. Suski, M. Leszczynski, I. Grzegory, S. Krukowski, G. Nowak, and G. Kamler, Journal of Crystal Growth **310**, 3979 (2008).

[99] P. Shiktorov, E. Starikov, V. Gruzinskis, M. Zarcone, D. Persano Adorno, G. Ferrante, L. Reggiani, L. Varani, and J. Vaissière, physica status solidi (a) **190**, 271 (2002).

[100] F. Sacconi, a. Di Carlo, and P. Lugli, Physica Status Solidi (a) **190**, 295 (2002).

[101] S. Fahy, A. Lindsay, H. Ouerdane, and E. O'Reilly, Physical Review B **74**, 1 (2006).

[102] M. Vaughan and B. Ridley, Physical Review B **75**, 1 (2007).

[103] W. Shan, K. M. Yu, W. Walukiewicz, J. Wu, J. W. Ager, and E. E. Haller, Journal of Physics: Condensed Matter **16**, S3355 (2004).

[104] E. P. O'Reilly, A. Lindsay, and S. Fahy, Journal of Physics: Condensed Matter **16**, S3257 (2004).

[105] S. Fahy and E. P. O'Reilly, Applied Physics Letters **83**, 3731 (2003).

[106] A. Patané, G. Allison, L. Eaves, N. V. Kozlova, Q. D. Zhuang, A. Krier, M. Hopkinson, and G. Hill, Applied Physics Letters **93**, 252106 (2008).

[107] D. A. Barry, S. J. Barry, and P. J. Culligan-Hensley, ACM Transactions on Mathematical Software **21**, 172 (1995).